



HAL
open science

The North Sistan orogen (Eastern Iran): Tectono-metamorphic evolution and significance within the Tethyan realm

Michael Jentzer, Philippe Agard, Guillaume Bonnet, Patrick Monié, Marc Fournier, Hubert Whitechurch, Jafar Omrani, Mohammad Hossein Zarrinkoub, Mohammad Mahdi Khatib, Reza Kohansal, et al.

► **To cite this version:**

Michael Jentzer, Philippe Agard, Guillaume Bonnet, Patrick Monié, Marc Fournier, et al.. The North Sistan orogen (Eastern Iran): Tectono-metamorphic evolution and significance within the Tethyan realm. *Gondwana Research*, 2022, 109, pp.460-492. 10.1016/j.gr.2022.04.004 . hal-03757182

HAL Id: hal-03757182

<https://hal.science/hal-03757182>

Submitted on 24 Aug 2022

HAL is a multi-disciplinary open access archive for the deposit and dissemination of scientific research documents, whether they are published or not. The documents may come from teaching and research institutions in France or abroad, or from public or private research centers.

L'archive ouverte pluridisciplinaire **HAL**, est destinée au dépôt et à la diffusion de documents scientifiques de niveau recherche, publiés ou non, émanant des établissements d'enseignement et de recherche français ou étrangers, des laboratoires publics ou privés.

Gondwana Research

The Sistan orogen (Eastern Iran): Tectonic evolution and significance within the Tethyan realm --Manuscript Draft--

Manuscript Number:	
Article Type:	GR Focus, Review Article
Keywords:	Sistan, metamorphic sole, obduction, pull apart, Iran, ophiolite
Corresponding Author:	Michael Jentzer, PhD. Sorbonne Université Campus Pierre et Marie Curie: Sorbonne Université Campus Pierre et Marie Curie Paris, FRANCE
First Author:	Michael Jentzer, PhD.
Order of Authors:	Michael Jentzer, PhD. Philippe Agard Guillaume Bonnet Patrick Monié Marc Fournier Hubert Whitechurch Jafar Omrani Mohammad Hossein Zarrinkoub Mohammad Mahdi Khatib Reza Kohansal Damien Do Couto Camille Godbillot Dia Ninkabou
Abstract:	<p>The N-S trending Sistan belt (E Iran) stretches N-S along ~700 km, at a high angle compared to the other Alpine-Himalayan ranges found along the Neotethyan suture zone. The aim of this study is to reappraise both the tectonic evolution of the Sistan orogen and its significance within the Neotethyan realm. The Sistan ophiolite, which started forming since 125 Ma, exhibits all the characteristics of present-day (ultra-)slow spreading environments. Closure of the Sistan ocean occurred through a major NE-dipping subduction zone active at least since 90 Ma, as indicated by (i) the location and age of bimodal juvenile arc magmatism, (ii) the regular SW vergence of the orogen and (iii) the location and age of subducted fragments. The discovery of 74-72 Ma metamorphic soles (~750°C-0.65 GPa) at the base of the ophiolite argues for the initiation of an intra-oceanic thrust/subduction zone, which ultimately led to the SW obduction of the ophiolite onto the Lut Block (mostly over by 50 Ma). Subsequent collision was marked by a drastic change of the Eocene sedimentation yet by only moderate shortening until the Oligocene (~30-40 km). Since the Late Miocene, post-collisional deformation appears strongly controlled by far-field stresses emanating from the Zagros collision. Given its orientation, petrological characteristics and age, the Sistan ocean probably opened as an independent pull apart basin along an inherited transform fault. The Sistan ocean also appears to have recorded the major geodynamic events which accompanied the closure of the Neo-Tethys, i.e. the major change in kinematics at ~90 Ma and the northward migration of India at ~75-70 Ma.</p>
Suggested Reviewers:	Jean Pierre Burg jean-pierre.burg@erdw.ethz.ch Federico Rossetti federico.rossetti@uniroma3.it

	Ali Mohammadi ali.mohammadi@erdw.ethz.ch
	G.R. FOTOOHI RAD gfotohi@yahoo.com
	Andréa Zanchi andrea.zanchi@unimib.it
Opposed Reviewers:	

The Sistan orogen (Eastern Iran):

Tectonic evolution and significance within the Tethyan realm

Michael Jentzer¹, Philippe Agard¹, Guillaume Bonnet¹, Patrick Monié², Marc Fournier¹,
Hubert Whitechurch³, Jafar Omrani⁴, Mohammad Hossein Zarrinkoub⁵, Mohammad Mahdi
Khatib⁵, Reza Kohansal⁴, Damien Do Couto¹, Camille Godbillot¹, Dia Ninkabou¹

¹*Sorbonne Université, CNRS, Institut des Sciences de la Terre de Paris (iSTeP), 4 place
Jussieu 75005 Paris, France*

²*Université de Montpellier, Géosciences Montpellier, place Eugène Bataillon 34095
Montpellier France*

³*Université de Strasbourg, Ecole et Observatoire des Sciences de la Terre, Institut de
Physique du Globe, Institut de Géologie, 1 rue Blessig, 67084 Strasbourg, France*

⁴*Geological Survey of Iran, Mehraj Bd., Tehran, Iran*

⁵*Department of Geology, University of Birjand, University Bd., Birjand, Southern
Khorasan, Iran*

26 **Abstract**

1
2
3 27 The N-S trending Sistan belt (E Iran) stretches N-S along ~700 km, at a high angle
4
5
6 28 compared to the other Alpine-Himalayan ranges found along the Neotethyan suture zone. The
7
8 29 aim of this study is to reappraise both the tectonic evolution of the Sistan orogen and its
9
10 30 significance within the Neotethyan realm. The Sistan ophiolite, which started forming since
11
12 31 125 Ma, exhibits all the characteristics of present-day (ultra-)slow spreading environments.
13
14
15 32 Closure of the Sistan ocean occurred through a major NE-dipping subduction zone active at
16
17
18 33 least since 90 Ma, as indicated by (i) the location and age of bimodal juvenile arc magmatism,
19
20 34 (ii) the regular SW vergence of the orogen and (iii) the location and age of subducted fragments.
21
22
23 35 The discovery of 74-72 Ma metamorphic soles (~750°C-0.65 GPa) at the base of the ophiolite
24
25 36 argues for the initiation of an intra-oceanic thrust/subduction zone, which ultimately led to the
26
27
28 37 SW obduction of the ophiolite onto the Lut Block (mostly over by 50 Ma). Subsequent collision
29
30 38 was marked by a drastic change of the Eocene sedimentation yet by only moderate shortening
31
32 39 until the Oligocene (~30-40 km). Since the Late Miocene, post-collisional deformation appears
33
34
35 40 strongly controlled by far-field stresses emanating from the Zagros collision. Given its
36
37
38 41 orientation, petrological characteristics and age, the Sistan ocean probably opened as an
39
40 42 independent pull apart basin along an inherited transform fault. The Sistan ocean also appears
41
42 43 to have recorded the major geodynamic events which accompanied the closure of the Neo-
43
44
45 44 Tethys, i.e. the major change in kinematics at ~90 Ma and the northward migration of India at
46
47 45 ~75-70 Ma.

49
50 46
51
52
53 47 **Keywords**

54
55
56
57 48 Sistan, metamorphic sole, obduction, pull apart, Iran, ophiolite
58
59
60 49
61
62
63
64
65

50 1. Introduction

1
2
3 51 The dominantly E-W trending Alpine–Himalayan mountain belts formed as a result of
4
5
6 52 the long-lived convergence between Eurasia and continental fragments derived from
7
8 53 Gondwana. Two main sutures (Figs. 1a, b) outlined by ophiolite belts, high-pressure low-
9
10 54 temperature metamorphic relics, magmatic arcs or flexural basins, stand out in this
11
12
13 55 superorogenic complex: (1) a northern suture marking the former location of the Paleotethys
14
15
16 56 ocean, which opened in the Early Devonian and disappeared through N-dipping subduction
17
18 57 below Eurasia from the Upper Carboniferous onwards, leading to continental collision in the
19
20 58 Late Triassic (e.g. Dercourt et al., 1986; Boulin, 1991; Besse et al., 1998; Stampfli and Borel,
21
22
23 59 2002; Richards and Şengör, 2017; Barrier et al., 2018); (2) a southern suture marking the former
24
25 60 location of the Neotethys ocean, which formed on the northern edge of Gondwana in the Upper
26
27
28 61 Carboniferous or Early Permian, when the Paleotethys ocean was still several thousand km
29
30 62 wide (Stampfli and Borel, 2002; Torsvik, 2016). Closure of the Neotethys, through N-dipping
31
32
33 63 subduction below Eurasia, started during the lowermost Jurassic and was followed by collision
34
35 64 during the Tertiary (e.g., during the Eo-Oligocene along the Zagros transect; e.g. Berberian and
36
37
38 65 Berberian, 1981; Dercourt et al., 1986; Sengor et al., 1988; Stampfli and Borel, 2002; Agard et
39
40 66 al., 2011; Barrier et al., 2018; Burg, 2018).

41
42 67 In detail, however, many issues remain unresolved, such as (i) the precise location of
43
44
45 68 each suture, most markers being discontinuous; (ii) the diachronicity of tectonic events along
46
47
48 69 strike of the same ocean (Stampfli and Borel, 2002); (iii) the exact number of sutures (e.g.,
49
50 70 Metcalfe, 2013); (iv) the exact number of intervening blocks and their lateral relationships (van
51
52 71 Hinsbergen et al., 2012). In particular, the respective location and geometries of the so-called
53
54
55 72 Cimmerian continental blocks, which lied between the two Tethyan oceans after the opening of
56
57 73 the Neotethys and before the final closure of the Paleotethys, are fraught with large
58
59 74 uncertainties.

75 These inferred blocks are separated by ophiolite belts, mostly Mesozoic in age, found
1 2 3 4 5 6 7 8 9 10
76 outside of the two main E-W Tethyan sutures (Figs. 1a, b). These ophiolite belts have
77 commonly been interpreted as marginal basins opened within the upper plate of the Neotethys
78 subduction system but their geodynamic evolution, initial location, spatial extension and mutual
79 relationships are still outstanding questions.

11 12 13 14 15 16 17 18 19 20
80 Within this framework, Iran lies in a central position and is one of the best places to
81 constrain Tethyan convergence (Figs. 1), for which contrasting tectonic reconstructions were
82 published (e.g. Berberian and King, 1981; Dercourt et al., 1986; Saccani et al., 2010; Agard et
83 al., 2011; McQuarie and van Hinsbergen, 2013; Ajirlu et al., 2016; Richards and Sholeh, 2016;
84 Barrier et al., 2018; Bonnet et al., 2020), and to assess the significance of its many ophiolite
85 belts (e.g., Nain-Baft, Sabzevar; Torbat-Heydarieh; Sistan; Jaz Murian; Moghadam and Stern,
86 2015 and references therein).

29 30 31 32 33 34 35 36 37 38
87 The Sistan orogen contains an extensive ~700 km long ophiolite belt and is located
88 halfway between the Zagros and Himalayan orogens. It separates the Afghan and Lut
89 continental blocks and appears most intriguing with its north-south orientation (Figs. 1; 2). It is
90 also the only orogen located at the rear of an active subduction system, namely the Makran
91 subduction zone (where the last fragments of Neotethys are presently disappearing; Figs. 1b).
92 The seismically active Sistan orogen was first surveyed in the late 1970s through pioneering
93 geological studies (Tirrul et al., 1983) but never comprehensively studied since.

46 47 48 49 50 51 52 53 54 55
94 The aims of the present contribution are to refine our present understanding of the Sistan
95 orogeny and its bearing on the history and geodynamic processes accompanying Tethyan
96 convergence. To this aim we provide (i) detailed cross-sections distributed across the northern
97 sector of the Sistan belt, merged into a first synthetic structural map and crustal scale cross-
98 section and (ii) tectono-metamorphic and geochronological constraints on the poorly studied
99 ophiolite domain and the eastern edge of the Lut block. These observations are combined with

100 existing magmatic and metamorphic data for the Sistan suture zone (including some recently
101 published by this group; Jentzer et al., 2017, 2020; Bonnet et al., 2018) into 2D lithospheric
102 scale geodynamic reconstructions of the Sistan realm. This study shows, in particular, that the
103 Sistan orogen (1) preserves a large obducted ophiolite with so far unreported metamorphic soles
104 that was only mildly affected by later collision and (2) represents a landmark at the crossroads
105 between the Zagros and Himalayas, recording all the major tectonic events occurring to the East
106 and West of the Neotethys ocean.

107 **2. Geological setting of the Sistan orogen**

108 2.1. Overall architecture

109 2.1.1. Main geological domains (as defined by Tirrul et al., 1983)

110 The Sistan belt was mapped at the 1:50.000 scale as part of an extensive regional
111 mapping and mineral exploration program with the Geological and Mineral Survey of Iran.
112 Based on lithostratigraphic (15 logs) and tectonic (three local cross-sections) investigations,
113 Tirrul et al. (1983) recognized five main domains (Figs. 2b):

- 114 – (1) The Lut Block to the W and (2) the Afghan Block to the E, characterized by
115 Neoproterozoic to Paleozoic basement. The youngest sediments deposited on top of
116 this basement prior to the Sistan orogeny are mildly deformed Jurassic series and
117 Early Cretaceous (Barremian-Aptian) Orbitolina limestones.
- 118 – (3) The Neh Complex, which comprises Aptian to Albian ophiolites and ophiolitic
119 mélanges together with sedimentary rocks of Senonian age, both assumed to be
120 weakly metamorphosed.
- 121 – (4) The Ratuk Complex, characterized by the presence of highly deformed, ophiolitic
122 mélange and metasediments locally metamorphosed under HP-LT conditions.

123 – (5) The Sefidabeh basin overlying both the Ratuk and Neh complexes, which consists
124 of Senonian to Eocene turbiditic sequences and was interpreted as deposited in a
125 fore-arc basin.

126 2.1.2. Geophysical constraints on the deep structure

127 Gravimetric data suggest that the Moho depth reaches up to ~52 km below the Sistan
128 orogen. This is slightly deeper than the 40 to 45 km depth reported everywhere else in the
129 adjacent Lut, Tabas, Yazd and Central Iran continental blocks composing the Central East Iran
130 Microcontinent (Figs. 2a; Mousavi and Ebbing, 2018; Eshagh et al., 2019). In contrast, the
131 lithosphere appears to be relatively thin below Sistan, as shown by two independent approaches:
132 (1) heat flow measurements higher than 100 mWm^{-2} (i.e. above the average 67 mWm^{-2} value
133 for continental domains; Davies, 2013; Lucazeau, 2019); (2) inversion of magnetic data, which
134 allows to estimate the 580°C isotherm Curie depth at ~48 km in this area. (Mousavi and Ebbing,
135 2018).

136 2.2. Main tectonic events from the Mesozoic onwards

137 The main tectonic stages which affected the Sistan domain since the
138 Mesozoic, which comprise all the steps of a single Wilson cycle (see Fig. 3), are briefly
139 described here. They will be further discussed below in the light of our results.

140 2.2.1. Rifting and spreading stages

141 The onset of rifting of the Sistan ocean is ill-constrained but spreading is
142 attested from the mid-Cretaceous onwards (Figs. 3): K-Ar dating on amphiboles from oceanic
143 gabbros in the ophiolites yield an Aptian age of $124 \pm 11 \text{ Ma}$ (Delaloye and Desmons, 1980),
144 while U-Pb dating of zircons from oceanic leucogabbros yield Albian ages between 107 ± 1
145 and $113 \pm 1 \text{ Ma}$ (Zarrinkoub et al., 2012a). This is coeval with deposition of the Orbitolina
146 limestone in the Lut and Afghan blocks. Biostratigraphic dating of radiolarites deposited on
147 ophiolitic material yield Upper Aptian to Lower Albian ages (Babazadeh and De Wever, 2004;

148 Ozsvárt et al., 2020), in agreement with isotopic dating. These authors inferred that the rifting
149 of the Sistan ocean started during the Lower (to Middle) Cretaceous.

150 Petrological and geochemical studies on the ophiolite (Delaloye and
151 Desmons, 1980; Moazzen et al., 2006; Saccani et al., 2010; Zarrinkoub et al., 2012a) show that
152 its mantle section mostly consists of harzburgite (less than 5% of clinopyroxene), affected by
153 variable degrees of serpentinisation. The crustal section dominantly comprises N-MORB
154 gabbros and basalts and rarer E-MORB basalts, respectively attributed to ridge-type
155 magmatism (~5-20% partial melting of DMM) and to an environment where the DMM is mixed
156 with an enriched source (e.g., interaction with a hot-spot; Saccani et al., 2010). Less common
157 mafic rocks bear calc-alkaline series with diagnostic enrichment in LREE, negative anomalies
158 in Nb, Ta suggesting a supra-subduction origin. Contrasting degrees of partial melting of the
159 mantle have been proposed: based on the Cr# [$Cr / (Cr + Al)$] of spinel in peridotite, Moazzen et
160 al. (2006) inferred it to be high, possibly advocating for fast spreading, whereas based on
161 geochemical modelling Saccani et al. (2010) and Zarrinkoub et al. (2012a) proposed an
162 intermediate to low degree of partial melting.

163 Berberian and Berberian (1981) proposed that the Sistan basin opened as a
164 back-arc basin above the retreating Zagros subduction zone of the Neo-Tethys ocean, which
165 was still active at that time (Agard et al., 2011). The paleogeographic orientation of the Sistan
166 ocean is still largely speculative, however, ranging from N100 to N160°E (e.g. Saccani et al.,
167 2010; Barrier et al., 2018).

168 Paleomagnetic data on the Central East Iran Microcontinent (CEIM;
169 Davoudzadeh et al., 1981; Soffel and Förster, 1984; Soffel et al., 1996; Besse et al., 1998;
170 Mattei et al., 2012, 2015; Figs. 3) show that (1) before the opening of the Sistan ocean, the
171 Yazd, Tabas and Lut blocks experienced a homogeneous counter-clockwise rotation of about
172 ~65° between the Upper Triassic and the Middle Jurassic, suggesting that these blocks formed

173 a single microcontinent at that time; (2) a ~30° counter-clockwise rotation of the CEIM between
174 the Upper Jurassic and the Upper Cretaceous which could be due to the Sistan rifting-spreading
175 formation and propagation.

2.2.2. Subduction stages

177 Subduction of oceanic lithosphere is attested by the presence of high-pressure low-
178 temperature metamorphic rocks (HP-LT) in the Ratuk complex (Tirrul et al., 1983), which
179 constrain the location of the Sistan suture zone (Figs. 2b, c). Peak P-T conditions for eclogites
180 range between 1.9-2.4 GPa and 435 -650°C (Fotoohi Rad et al., 2005; Angiboust et al., 2013).
181 Most recent estimates point to a relatively cold subduction thermal regime (~7°C/km; Bonnet
182 et al., 2018). Retrograde P-T conditions were estimated from 0.5 to 0.8 GPa and between 470
183 and 530°C (Angiboust et al., 2013; Kurzawa et al., 2017; Bonnet et al., 2018).

184 Bröcker et al. (2013) used three methods to date the HP-LT metamorphic rocks along
185 the Ratuk complex: (1) Rb-Sr on phengite, glaucophane, omphacite, biotite, epidote, garnet,
186 albite and garnet from eight samples yield ages between 87.1 ± 0.3 and 84.9 ± 0.6 Ma for the
187 mineral assemblages near the eclogitic peak, while retrograde assemblages yield a younger age
188 at 78.9 ± 0.5 Ma; (2) ^{40}Ar - ^{39}Ar plateau ages on five samples, which range between 87.6 ± 0.6
189 and 81.3 ± 1.3 Ma; and (3) U-Pb on zircons from four samples, which yield ages between 89.3
190 ± 1.6 and 86.1 ± 1.1 Ma. Bonnet et al. (2018) provided fourteen Ar-Ar ages on phengite and
191 amphibole ranging from 88.4 ± 0.35 to 83.81 ± 0.94 Ma without significant difference between
192 near peak and retrograde assemblages. Most authors agree on an age of peak burial of the
193 eclogites at 86 ± 3 Ma. Somewhat older Ar-Ar ages on phengite and amphibole (between 139
194 ± 19 Ma and 116 ± 19 Ma; Fotoohi Rad, 2009) were interpreted to result from excess Ar
195 (Bröcker et al., 2013).

196 Thick deposits of Senonian flysch also imply the presence of a highly subsiding basin,
197 probably related to the existence of a nearby subduction zone (Tirrul et al., 1983). Last, low-K

198 calc-alkaline magmatic rocks intruding or interbedded with the Senonian flysch, and capped by
199 the Paleocene reef of the Sefidabeh basin, were shown to correspond to subduction-related
200 juvenile arc magmatism (Jentzer et al., 2020). In the same location, Jentzer et al. (2020)
201 described high-silica adakites, produced with a component of slab melting. These authors
202 argued for NE-dipping subduction of the Sistan ocean beneath the Afghan margin since the
203 Turonian (i.e., after ~93 Ma). Subduction polarity has been the matter of debate, however, with
204 authors arguing for either east- (Tirrul et al., 1983) or west-dipping subduction zone (Pang et
205 al., 2013; Boskabadi et al., 2020; Ozsvárt et al., 2020).

2.2.3. Collisional stages

Coarse grained proximal molasse-type Eocene sediments overlying earlier
flysch deposits are thought to postdate ocean closure and to constrain the onset of collision
between the two continental blocks. Based on unconformities Tirrul et al. (1983) identified two
stages of deformation during the Eocene. Eocene deformation is sealed by unconformable, less
deformed Oligocene deposits.

Voluminous, mildly deformed syn- to post-collisional Paleogene magmatism
cuts across the Lut block and part of the Sistan orogen (Camp and Griffis, 1982; Figs. 2b; 3).
Ar-Ar age constraints for these magmatic rocks span from the Mid-Eocene (ca. 46 Ma) to the
Lower Oligocene (ca. 25 Ma). This magmatism has been interpreted as the result of the
delamination of the lithospheric root following collision (e.g.: Pang et al., 2013; Mohammadi
et al., 2016; Omidianfar et al., 2020).

2.2.4. Post collisional stages

Paleomagnetic data suggests that since the Miocene another ~35° counter-
clockwise rotation affected the CEIM (Soffel et al., 1996; Mattei et al., 2015). The main
horizontal stress rotated around 60° counter-clockwise, probably due to the increasing influence
of the “hard” collision in the Zagros (Jentzer et al., 2017 and references therein). The Sistan

223 orogen is still tectonically active, as shown by several morphologic indicators (e.g., shifts of
224 river waterways) and by instrumental seismicity and paleoseismicity studies of strike-slip
225 faults. The dominant set of active faults comprise N-S right-lateral faults and their conjugate
226 left-lateral NW-SE-trending reverse faults (Berberian et al., 2000; Walker and Khatib, 2006),
227 which are compatible with a N025 orientation of the main horizontal stress (Jentzer et al., 2017).
228 These strike-slip faults also act as major pathways for upper Cenozoic intraplate post-collisional
229 alkali-basalts (ca. 27 to 2 Ma, K-Ar or Ar-Ar dating on whole rocks; Camp and Griffis, 1982;
230 Walker et al., 2009; Pang et al., 2012). This alkaline magmatism has been interpreted as
231 deriving from an asthenospheric upflow following lithospheric delamination (Pang et al., 2012).

232 2.3. Major unknowns and detailed objectives of this study

233 Our current knowledge of the Sistan orogen suffers from at least two major
234 unknowns:

235 (1) Several first-order questions regarding the tectonic evolution of the Sistan
236 orogen are still a matter of debate, including: (i) the determination of the ocean type, ranging
237 from fast to (ultra) slow spreading ocean; (ii) the timing of closure of the ocean basin, during
238 the Upper Cretaceous or the Paleogene, as well as subduction polarity (i.e. NE- or SW-dipping,
239 or both); (iii) the process allowing the emplacement and preservation of the (presumably)
240 unmetamorphosed Neh ophiolite; (iv) the onset (during the Paleocene or Eocene) and
241 termination of collision, the amount of overall shortening and extent of deep basement thrusting
242 (i.e., thin- or thick-skin tectonics). To that end, the architecture and structural relationships of
243 the main domains (Neh complex, Ratuk complex and Sefidabeh basin) need to be refined.

244 (2) The paleogeography of the Sistan within the Tethyan framework requires
245 further investigations to assess its orientation and potential relationships with nearby marginal
246 basins such as Sabzevar, N-Makran and/or Ras Khoh.

247 The present study aims at addressing the first set of questions by focusing on
1
2 248 dedicated areas (Figs. 2c; 4) and using two major approaches: (1) structural investigation of
3
4 249 each domain to constrain their organization and the overall present-day architecture of the
5
6
7 250 Sistan orogen and (2) a metamorphic and geochronologic approach to further characterize the
8
9
10 251 Neh complex and constrain its emplacement as well as metamorphism of the eastern margin of
11
12 252 the Lut block.

15 253 **3. Structural map of Sistan**

18
19 254 Regional mapping of the northern part of the Sistan orogen was conducted in 1977 and
20
21
22 255 1978 by the Geological Survey of Iran (together with the Bureau de Recherches Géologiques
23
24 256 et Minières). Results are published in the 1:250 000 scale maps of Qayen, Shahrakht, Birjand,
25
26
27 257 Gazik, Dehsalm and Zabol (and three detailed reports for Qayen, Shahrakht and Gazik). The
28
29 258 corresponding 1:100 000 scale maps were published during the 1990's.

30
31 259 We have combined the six 1:250 000 scale maps of the North Sistan belt to produce a
32
33
34 260 comprehensive and homogeneous map (Figs. 4a). To improve readability, some simplifications
35
36 261 and specific groupings were necessary:

37
38
39 262 – All ultramafic rocks (dunite, harzburgite and lherzolite) and their altered or
40
41 263 metasomatized products (serpentinite and listvinite), magmatic rocks representing
42
43
44 264 the crustal section of the Sistan ocean (gabbro, basalt and spilite, dolerite and
45
46 265 plagiogranite) and ocean floor, deep-sea sediments (radiolarites, phyllites and
47
48
49 266 pelagic carbonates), together with what is mapped as “colored mélange” were
50
51 267 merged into what is referred to here as ophiolite.

52
53
54 268 – Magmatic rocks are shown by age (e.g., Precambrian, Jurassic and Early Cretaceous)
55
56 269 except for Tertiary magmatism, which had to be grouped since ages proposed for
57
58
59 270 the same formation on neighbouring maps do not allow to be more precise. In

271 addition to the volcanic and plutonic rocks, volcano-sedimentary rocks like tuff,
272 volcanic breccia, and ignimbrite have been associated to this group.

273 – Sedimentary rocks are shown by age. The rare Oligocene and Miocene outcrops were
274 merged because they are mainly continental deposits (red beds and conglomerates)
275 difficult to date accurately.

276 – Metamorphism is indicated by hatching. Due to the lack of data, metamorphic facies
277 cannot be indicated, except for the more extensively studied HP-LT metamorphism
278 of the Ratuk complex.

279 This map highlights three main gaps in the knowledge of the structure of Northern
280 Sistan, as defined by Tirrul et al. (1983): (1) the boundary between the Sistan suture zone and
281 the Afghan Block, originally defined by the western extension of the Barremian-Aptian
282 Orbitolina limestone, must be refined due to the discontinuity of the Orbitolina limestone
283 outcrops; (2) despite the sub-division of the Sistan suture zone into three main units, the
284 relationship between the Neh and Ratuk complexes or the extension and structural position of
285 the Sefidabeh basin are unknowns; (3) the boundary between the Sistan suture zone and the Lut
286 Block, originally defined by the NE limit of the Jurassic pelitic schist, must be refined since
287 Jurassic sediments are overlain by younger Cretaceous deposits in several places.

288 **4. Methodology: from field to P-T-t estimations**

289 This section presents an overview of the methodology used in this study. Details on the
290 analytical protocols, the tools used to estimate P-T conditions or the geochronological methods
291 can be found below in the Appendix (together with relevant references).

292 Fieldwork consisted in collecting structural data to build cross-sections and samples for
293 metamorphic and geochronologic analysis, mainly on three targets (Figs. 2c ; 4): (1) the eastern
294 side of the Sistan orogen, in order to refine the organization of the Ratuk complex and the

295 Sefidabeh basin and to constrain the relationships between the main domains; (2) the central
296 domain, to constrain the internal organization of the Neh complex and (3) the border between
297 the Neh complex and the Lut Block, to constrain their mutual relationships and metamorphism.

298 Textures, mineral occurrences and mineral zoning were determined by optical
299 microscopy and scanning electron microscopy (SEM, ZEISS Supra 55 VP). Mineral
300 compositions were determined by electron probe micro-analysis (Cameca SX-5 and SX-100;
301 CAMPARIS, Sorbonne Université). Maximum temperatures experienced by organic-rich
302 samples were determined by Raman spectroscopy of Carbonaceous Material (RSCM;
303 Renishaw inVia, Ecole Normale Supérieure), following the method of Beyssac et al. (2002).

304 Whole-rock major element composition was obtained after crushing and dissolution by
305 Inductively Coupled Plasma Optical Emission Spectrometry (ICP-OES iCap 6 500; ALIPP6,
306 Sorbonne Université).

307 Ar/Ar isotopic measurements were done on grain separates by laser ablation coupled to
308 a multi-collector noble gas mass spectrometer (Thermo-Fisher Argus VI; Géosciences
309 Montpellier). Titanite U-Pb analyses were performed in-situ in thin sections by laser ablation
310 split-stream inductively coupled plasma mass spectrometry (LASS ICP-MS; Univ. California
311 Santa Barbara).

312 Different methods were used to estimate P-T conditions depending on each lithology.
313 For mafic samples, the Ti content in Ca-Amphibole (Ernst and Liu, 1998) and the Na-Si vs Ca-
314 Al exchange between amphibole and plagioclase (Holland and Blundy, 1994) were used to
315 estimate temperature. The Al/Si exchange between plagioclase and Ca-Amphibole were used
316 to estimate equilibrium pressure (Ernst and Liu, 1998). The Zr content in titanite was used, in
317 zircon-bearing samples, to place constraints on maximum temperature conditions.

318 For metasedimentary rocks, maximum temperatures were estimated by the RSCM
319 method. Empirical thermometry based on the Ti content in biotite and Garnet-Biotite Fe-Mg

320 exchange was also used. Pressure was estimated using Garnet-Biotite-Aluminosilicate-Quartz
1
2 321 barometry.
3

4 322 Thermodynamic modelling of selected samples was performed in the NCFMASHTO
5
6
7 323 and MnNCKFMASHTO chemical systems, respectively, with the Perple-X software
8
9
10 324 (Connolly, 2005) using whole-rock compositions. Mineral assemblages and chemistry were
11
12 325 then compared to those predicted by thermodynamical modelling.
13
14

15 326 **5. Sedimentary basins: types and burial metamorphism**

17 18 19 327 5.1. Stratigraphy 20

21
22 328 This section summarizes the observations made by Tirrul et al. (1983) and Maurizot et
23
24 329 al. (1990a; 1990b), complemented by ours. Though not representative of all parts of the basins,
25
26
27 330 this description is meant to illustrate the style of sedimentation and the stratigraphic
28
29 331 relationships within the Sefidabeh, Ratuk and Neh complexes (Figs. 3).
30

31 332 5.1.1. Stratigraphy of the Sefidabeh basin 32

33
34 333 The thickness of the Cenomanian to Eocene sedimentary deposits in the Sefidabeh basin
35
36 334 (Figs. 3) was estimated at around 8 km (Tirrul et al., 1983). In the Northern Sistan Orogen, the
37
38
39 335 Sefidabeh basin develops on the Afghan margin (see below).
40

41 336 The oldest rocks are mainly Senonian in age but some biostratigraphic markers hint to
42
43
44 337 an Aptian age for the base of this formation (Tirrul et al., 1983). This sequence (Lahnu
45
46 338 formation, Figs. 5a) is mainly composed by calci-turbidite with layers of marl and limestone,
47
48
49 339 in places called (calc-)flysh. Calc-alkaline rocks and adakites are intrusive or interbedded in
50
51 340 this sequence (Jentzer et al., 2020). In some places, Maastrichtian sediments can be recognized.
52
53
54 341 Their base is a polygenic breccia reworking ophiolite pebbles (Darband-Bad formation; Figs.
55
56 342 5b) evolving upwards into a turbiditic, marl and shale sequence (Nesfandeh formation; Figs.
57
58 343 5c) locally interbedded with a ten-meter-thick Hyppuritic and Orbitoid bearing limestone (Figs.
59
60
61
62
63
64
65

344 5d-f). Maastrichtian ages were confirmed, east of Sulabest, by biostratigraphy on microfossil
1
2 345 assemblage (*Omphalocyclus* sp., *Lepidorbitoides* sp., *Orbitoides* sp., *Siderolites* sp; S.
3
4 346 Soleimani, GSI, pers. comm.).
5
6

7 347 The base of the Paleocene is a reefal limestone slightly unconformable on top of the
8
9 348 Upper Cretaceous deposits, showing large thickness variations, from ~0 to >600 m (Palang
10
11 349 formation; Figs. 5g-h). It is overlain by an Upper Paleocene turbiditic sequence (Chah Chucchu
12
13 350 formation; Figs. 5i) locally preserving paleo-channels and Nummulites, especially in the core
14
15 351 of synclines.
16
17
18

19 352 Eocene sediments are “red beds” polygenic continental puddingstone observed only on
20
21 353 the easternmost part of the basin (Figs. 5j). They lie unconformably on top of the Paleocene
22
23 354 series. Calc-alkaline affinity lavas and dykes are present in the Eocene. Oligocene deposits
24
25 355 correspond also to “red bed” facies with an increase of the volcano-clastic component from the
26
27 356 Eocene magmatic activity. Although both sedimentary sequences are conglomeratic, a major
28
29 357 unconformity marks the limit between Eocene and Oligocene deposits. Miocene lavas and
30
31 358 dykes are found in a few places (Camp and Griffith, 1983). The latest sediments are Plio-
32
33 359 quaternary polygenic continental conglomerates reworking all previous lithologies (Figs. 5k).
34
35
36
37
38

39 360 5.1.2. Stratigraphy of the Ratuk complex 40

41 361 The metamorphic units of the Ratuk complex (see Geological setting) are
42
43 362 unconformably overlain by a Maastrichtian conglomerate evolving upwards into a turbiditic
44
45 363 sequence (equivalent to the Darband-Bad formation; Figs. 5b). In some places, Eocene red-beds
46
47 364 (equivalent those in Figs. 5j) overly unconformably the Maastrichtian sequence. Plio-
48
49 365 quaternary polygenic conglomerates (equivalent of Figs. 5k) are also locally observed.
50
51
52

53 366 5.1.3. Stratigraphy of the Neh complex 54

55 367 The total thickness of the sedimentary succession of the Neh basin, from Upper
56
57 368 Turonian to Eocene, reaches ~4 km (Tirrul et al., 1983). Half of it is made by phyllite
58
59
60
61
62
63
64
65

369 interbedded with sandstone dated from the Upper Cretaceous to the Early Cenozoic (most likely
1
2 370 Paleocene).

3
4 371 The first sedimentary rocks on top or interbedded between lavas of the ophiolite are
5
6
7 372 alternations of radiolarian chert, marl and/or limestone (Figs. 5l). No biostratigraphic dating is
8
9 373 available for these rocks but a Lower Cretaceous age could be expected based on the
10
11
12 374 geochronologic ages of the ophiolite (between 124 and 107 Ma, Aptian-Albian).

13
14 375 Upper Cretaceous and Paleocene deposits are fine grained turbidites dominated by
15
16
17 376 phyllite, minor sandstone and locally layers of limestone (Figs..5m-n). These depositis are
18
19 377 referred to as flysch in some 1:250000 scale maps. Upper Cretaceous deposits are mostly
20
21
22 378 exposed in the eastern part of the Neh complex, whereas Paleocene sediments dominate in its
23
24 379 central part (Figs. 2c).

25
26 380 Eocene sedimentation exhibits a marked increase of the clastic component. In the
27
28
29 381 southern Neh complex, where Eocene deposits are best exposed (Figs. 2c), sediments are silici-
30
31 382 clastic turbidite (aka flysch; Figs. 5o) interbedded with Nummulite bearing sandy limestone
32
33
34 383 (Figs. 5p). In the North, the Eocene and Oligo-Miocene deposits are mainly composed by a
35
36 384 shallower, massive conglomerate reworking all previous lithologies (Figs. 5q), including
37
38
39 385 andesitic Eocene volcanics. Conglomerates are interbedded with a Nummulite-bearing sandy
40
41 386 limestone. A major unconformity marks the limit between Eocene and Oligocene deposits
42
43
44 387 (Tirrul et al., 1983). The latest sediments are Pliocene polygenic channelized continental
45
46 388 conglomerate reworking all the previous lithologies (Figs. 5r).

47 48 389 5.2. Maximum temperatures experienced by Sistan sediments

49
50
51 390 In order to evaluate the amount of differential burial of the various sediments (and
52
53 391 estimate either burial depths or heat fluxes), RSCM measurements were performed on samples
54
55
56 392 collected from the Neh complex and from the northern limit of the Lut Block. Out of the 44
57
58 393 samples, about half of them had a too low or oxidized organic content. Results for the other
59
60
61
62
63
64
65

394 half, out of which 13 from the Upper Cretaceous and 5 from the Paleocene Neh complex, are
395 shown in Figure 6 (and on Supplementary material 2). None of the Eocene samples yielded
396 results. Three samples come from the Jurassic siltstone of the Lut block. Figure 4 is
397 complemented by three variably metamorphosed Late Cretaceous flysch samples from the HP-
398 LT Ratuk complex (sample 14-38 is not unmetamorphosed; Bonnet et al., 2018). Maximum
399 temperatures (Tmax) can be divided in three groups (Figs. 6):

400 (1) Tmax obtained throughout the Neh complex, from the Paleocene sample 16-68 in
401 the south to the Cretaceous sample 14-37 in the north, are close to the average $275^{\circ}\text{C} \pm 50^{\circ}\text{C}$
402 value. Tmax from Upper Cretaceous or Paleocene samples are undistinguishable. Only one
403 sample (16-41) gives a higher value, which could be explained by its proximity with several
404 intrusive dykes (which are known to affect Tmax estimates; e.g., Chen et al., 2017).

405 (2) Except for sample 17-20 with 326°C , samples from the S of the Neh complex (14-
406 07; 14-23a, 15b-10 and 16-80) have a significantly higher Tmax at 515°C on average, close to
407 those obtained in the Jurassic deposits of the Lut Block at 508°C in average. These results will
408 be interpreted in the light of their structural position (see discussion below).

409 (3) In the north east, sample 14-38 has a Tmax compatible with the average 270°C in
410 the Neh complex while samples 14-39a/b and 14-40 give Tmax 70°C higher.

411 6. Ophiolitic rocks from the Neh complex

412 The structures and lithologies of the ophiolitic part of the Neh complex were studied to
413 the south of Birjand and northwest of Nehbandan. Figures 4 and 7-8 show some of the main
414 ophiolite exposures, with special emphasis on the ophiolitic ridge south of Birjand.

415 6.1. Overall structure and internal organization of the ophiolitic ridge near Birjand

416 The 1:100 000 map of the Birjand ophiolitic ridge (essentially produced using airplane
417 photographs; Eftekhar Nezhad et al., 1987) features at least three types of colored mélangé and

418 profuse vertical contacts between peridotites, serpentinites, basalts and gabbros. Based on
1
2 419 extensive observations (Figs. 4a; and complementary satellite images), we have reappraised the
3
4 420 structural organization of the eastern sector of the Birjand ophiolitic ridge, identifying three
5
6
7 421 main units thrust on top of each other (Fig. 7):
8

9 422 (1) The northernmost Unit 1 is characterized, from bottom to top, by peridotites, an
10
11 423 almost continuous level of pillow-lavas or brecciated basalts, rare radiolarites and Cretaceous
12
13 424 turbidites. Thrusting of Unit 1 over Unit 2 is marked by a crushed zone with various
14
15 425 dismembered material (Fig. 7b). Some exposures show evidence for the existence of fossil
16
17 426 oceanic detachment faults. In the outcrop shown in figures 8a-f (interpreted in Fig. 7f), a hm-
18
19 427 to km-scale fault zone, outlined by striated peridotite and foliated amphibolite facies gabbro,
20
21
22 428 separates serpentinized peridotite, overlain by a breccia containing clasts of dismembered
23
24 429 pillows within a carbonate matrix and pillow-basalts above, from serpentinized peridotite
25
26
27 430 sparsely overlain by ophicalcite.
28
29
30

31 431 (2) Unit 2 (Fig. 7c) is characterized by massively serpentinized and in places brecciated
32
33 432 peridotite (Figs 8g-h) with dunitic channels. This mantle section is cross-cut by scarce
34
35 433 rodingites and plagiogranites and locally intruded by gabbroic pods, which is uncommon in
36
37
38 434 Unit 1. Contrary to Unit 1, pillow lavas are rare and do not constitute a continuous horizon. At
39
40
41 435 the base of Unit 2, the contact onto Unit 3 is outlined by a tectonic *mélange* (Figs. 7c).
42

43 436 (3) Unit 3 mostly crops out as a tectonic window below Unit 2 (Fig. 7d). Unit 3 is
44
45 437 characterized by serpentinized peridotite intruded by large masses of gabbros and dolerites and
46
47 438 overlain by ophicalcite and brecciated material (Figs. 8i-k). Pillow-lavas are rare and
48
49
50 439 discontinuous, as for Unit 2. Radiolarian cherts and Cretaceous turbidites are present in a few
51
52
53 440 places. The Eocene Nummulitic sandy limestone was deposited unconformably either on the
54
55
56 441 Cretaceous turbidite or directly on the peridotite. This Eocene deposit is affected by large-scale
57
58
59
60
61
62
63
64
65

1
2 442 asymmetric drag folds and overthrust in places by peridotites of Unit 2 or Unit 3 (Fig. 7d). This
3 443 basal unit exhibits metasedimentary rocks (see below).

4 444 Each of these units shows kilometre scale continuity, at odds with the characteristics of
5
6
7 445 a chaotic mélangé (Fig. 7e). The stack of units was affected by later tectonics, as shown by the
8
9
10 446 thrusting of peridotite over Neogene conglomeratic deposits south of the Birjand ridge, or by
11
12 447 sinistral strike-slip faults cutting through the ridge. The core of the Birjand ridge was intruded
13
14 448 by Oligo-Miocene then Plio-Quaternary magmatism.

15 16 17 449 6.2. Petrology and mineralogy

18
19 450 A brief overview of the petrology and mineralogy of the three main lithologies observed
20
21
22 451 in the ophiolite is given here (Table 1). Peridotites, mildly to completely serpentinized (Figs.
23
24 452 9a-b), dominantly correspond to harzburgite with olivine, orthopyroxene, rare clinopyroxene,
25
26 453 titanite, Fe-Ti oxide and occasional amphibole (Delavari et al., 2009; Saccani et al., 2010;
27
28 454 Zarrinkoub et al., 2012a). Gabbroic intrusions mostly comprise clinopyroxene and plagioclase,
29
30
31 455 commonly altered to prehnite. A foliation marked by amphiboles is visible in some samples
32
33
34 456 (Figs. 9c-d).

35
36 457 Basalts are exposed as discontinuous layers, hundred meters thick at most. They are
37
38
39 458 made of phenocrysts of clinopyroxene, plagioclase and Fe-Ti oxide in an aphanitic matrix
40
41 459 (Figs.9e-f). Some have secondary phases such as epidote and/or pumpellite and occasional
42
43 460 calcite veins. Basaltic fragments are also found directly above serpentinized peridotite, as cm-
44
45
46 461 to m-scale clasts in sedimentary breccia/olistostrome or ophicarbonates.

47
48 462 Microprobe analyses were performed in serpentinized peridotite and gabbro (see
49
50
51 463 supplementary material 1). In gabbros, clinopyroxene compositions are close to augite, while
52
53 464 amphibole compositions range from actinolite to tschermakite but are mainly Mg-hornblende;
54
55
56 465 plagioclase is >88 mol% albite. Serpentinized peridotites contain enstatite, amphibole (mostly
57
58 466 tremolite or edenite, but with some Mg-hornblende) and olivine close to the forsterite

467 endmember. Semiquantitative amphibole geothermobarometry (Ernst et Liu, 1998) gave results
1
2 468 between 625°C and 775°C and between 0.3 GPa and 0.7 GPa for the amphibolitized gabbroic
3
4 469 sample 16-01c (equivalent to 15b-18 in Fig. 8e).
5
6
7

8 470 **7. Sections across the northern branch of the Sistan orogen**

9

10
11
12 471 Structural observations are summarized on nine sections across the Sistan belt,
13
14 472 presented from north to south (Figs. 11; location on Fig. 2c). Representative exposures are
15
16 473 shown in Figure 11.
17
18

19 474 7.1. Gomenj transect

20

21
22 475 This northern cross-section comprises four main domains (Fig. 11a). In its western part,
23
24 476 a thick series of Quaternary and Neogene conglomerates is deformed and overthrust by Upper
25
26 477 Cretaceous flysch and unmetamorphosed ophiolitic rocks. The area is pervasively intruded by
27
28 478 Eocene to Miocene magmatism.
29
30

31 479 Further east, a hm-thick crushed zone with amphibolitized blocks in a serpentinite
32
33 480 matrix (and abundant listvenite) likely corresponds to the HP-LT zone observed in Gazik
34
35 481 (section below) or Sulabest (Angiboust et al., 2013). Sefidabeh basin sediments are thrust over
36
37 482 the crushed zone.
38
39
40

41 483 These sediments consist of Upper Cretaceous (Senonian) flysch interbedded and/or
42
43 484 intruded by arc magmatic rocks unconformably overlain by the Paleocene reef limestone and
44
45 485 turbidite (equivalent to the one in Figs. 10a, c), and finally by the Eocene “red bed”. At this
46
47 486 latitude the Sefidabeh basin is extremely narrow, allowing to study the basement of the Afghan
48
49 487 Block in the eastern part of the section. This basement comprises of Paleozoic granodiorite and
50
51 488 amphibolites and a sedimentary cover made of Early Cretaceous series (i.e., oosparitic
52
53 489 sandstone overlain by Orbitolina limestone). Basement rocks are thrust over the Sefidabeh
54
55
56
57
58 490 basin in its western part, while large-scale folds are observed in the sedimentary cover in the
59
60
61
62
63
64
65

491 eastern part. The thrust contact between the basement and the cover corresponds to a reactivated
1
2 492 normal fault. On this transect, the western limit of the Afghan block (Tirrul et al., 1983) does
3
4
5 493 not always coincide with the westernmost outcrop of Orbitolina limestone.
6

7 494 7.2. Gazik transect

8
9 495 This section reveals four main parts (Figs. 11b; for more local sections on this transect:
10
11
12 496 Bonnet et al. 2018; Jentzer et al., 2020), from west to east:

13
14 497 (1) An ultramafic unit made of serpentinite with rare radiolarites or basalts and locally
15
16
17 498 m- to hm-large gabbroic intrusions. It is overlain by folded Cretaceous turbidite (intruded by
18
19 499 Oligo-Miocene dykes). This unit is in apparent continuity with the (mostly) unmetamorphosed
20
21
22 500 Neh complex.

23
24 501 (2) Slices of serpentinitized peridotite, with a few gabbroic pods, locally overlain by
25
26
27 502 pillow lavas and/or radiolarite. In the eastern part, thick Maastrichtian turbidites are folded into
28
29 503 a broad syncline and intruded by massive Oligo-Miocene quartz-diorites. The basal peridotite
30
31
32 504 hosts Senonian adakitic dykes and sills.

33
34 505 (3) The HP-LT zone, more extensive than on the Gomenj section, which comprises three
35
36 506 main units separated by tectonic contacts (Fig. 10d): (a) a serpentinite-matrix mélange made
37
38
39 507 of a fine-grained (to locally massive) matrix surrounding metamorphic blocks of pillow-lavas
40
41 508 or metatuffs. This mélange can be sub-divided based on the peak metamorphic assemblage of
42
43
44 509 the blocks: the basal portion reached eclogitic facies while the top portion only reached
45
46 510 blueschist facies (Bonnet et al., 2018); (b) a mélange with a tuffaceous matrix, containing
47
48
49 511 blocks of marl, radiolarite, serpentinite, sandstone or basalts, metamorphosed in the greenschist
50
51 512 facies at most; (c) Maastrichtian turbiditic sediments, with a monogenic basal conglomerate
52
53 513 reworking pieces of serpentinite.

54
55
56 514 (4) The Sefidabeh basin, with the same characteristics as in Gomenj.
57
58
59
60
61
62
63
64
65

1
2
3
4
5
6
7
8
9
10
11
12
13
14
15
16
17
18
19
20
21
22
23
24
25
26
27
28
29
30
31
32
33
34
35
36
37
38
39
40
41
42
43
44
45
46
47
48
49
50
51
52
53
54
55
56
57
58
59
60
61
62
63
64
65

515 The suture zone separates the HP-LT zone from the Afghan block, here marked by the
516 Orbitolina limestone. It is represented by a steep contact, which must have accommodated the
517 exhumation of the HP-LT units. The boundary between the HP-LT zone and the Sefidabeh
518 basin was reworked into a major reverse and right lateral strike-slip fault (Fig. 11b). Steep faults
519 and local back-thrusting hints to the presence at depth of a flower structure along the contact.
520 Upper Cretaceous volcanoclastics found along this transect could correspond to material
521 reworked from the former Senonian magmatic arc (Jentzer et al., 2020).

522 7.3. Rازه transect

523 The Rازه cross-section outlines the southward widening of the Sefidabeh basin (Fig.
524 11c). In its western part, Quaternary conglomerates unconformably overlie coarse
525 Maastrichtian sediments deposited on top of the HP-LT units and are actively deformed below
526 the overthrusting Sefidabeh basin (close to Fig. 10a). To the east, the Sefidabeh basin consists
527 of Upper Cretaceous (Senonian) flysch interbedded with a ten-meter thick reef preserving large
528 rudists. It is interbedded and/or intruded by a significant amount of arc magmatic rocks. The
529 younger Paleocene reef appears slightly unconformable and shows large thickness variations,
530 from ~0 to >600 m (same as Figs. 10a, c). Above it, the Paleocene turbidite with Nummulite-
531 rich paleo-channels is preserved in the core of a broad syncline. Eocene red beds, observed in
532 the easternmost part only, lie unconformably on locally very thin Paleocene series. The absence
533 of Paleocene turbidite hints to erosion prior to deposition of Eocene sediments. Eocene to
534 Miocene magmatic rocks intrusions are present.

535 7.4. Sulabest transect

536 A major dextral strike-slip fault (the East Neh fault) marks the eastern limit of the Neh
537 complex. Three main units of the Ratuk complex proposed by Angiboust et al. (2013) were
538 recognized by (close to Fig. 10d), from bottom to top: (1) the Eclogitic Unit, at the base,
539 cropping-out into a tectonic window, corresponds to a mélange with a serpentized matrix

540 surrounding rare blocks of metaradiolarite and more abundant eclogitic metabasic blocks
1
2 541 retrogressed into amphibolite facies; (2) the Upper Unit, which is a mélangé with a tuffaceous
3
4 542 matrix hosting blocks metamorphosed in the blueschist facies; (3) the Western Unit, made of
5
6
7 543 serpentinized peridotite, pockets of gabbro, pillow basalts and radiolarites, which lacks HP-LT
8
9
10 544 metamorphic relics. The Western Unit is in apparent continuity with the unmetamorphosed
11
12 545 ophiolitic units found to the west of the HP-LT zone in the previous cross-sections. Since this
13
14 546 unit also exhibits Senonian arc magmatism (Jentzer et al., 2020), we consider that it represents
15
16
17 547 the westernmost domain of the Afghan Block, either a stretched ocean continent transitional
18
19 548 domain or an accreted forearc domain.

21
22 549 To the east, the HP-LT units are covered by folded Maastrichtian polygenic
23
24 550 conglomerates grading upwards into a turbiditic sequence. Plio-Quaternary polygenic
25
26 551 conglomerates overlie all previous lithologies and are deformed below the thrust contact with
27
28
29 552 the Sefidabeh basin (locally underlined by abundant listvenite). The western part of the
30
31 553 Sefidabeh basin is characterized by Upper Cretaceous (Senonian) turbidite and associated arc
32
33
34 554 magmatism rocks covered by the Paleocene reef. Its overall structure is comparable to that
35
36 555 presented on the Razeh cross-section (Fig. 11c). All units are intruded by Eocene to Miocene
37
38
39 556 magmatism, located in the vicinity of major tectonic contacts and recently deformed. Neogene
40
41 557 (Pliocene to Quaternary) alkali-basalts with basaltic columns are present close to the East Neh
42
43 558 fault (Fig. 10e).

46 559 7.5. Doroh transect

47
48 560 The Doroh cross-section corresponds to our southernmost transect along the contact
49
50
51 561 between the HP-LT zone and the Afghan Block (Fig. 11e). Its western part exhibits the same
52
53 562 lithologies and structural organization as in the previously described HP-LT zone (e.g., Fig.
54
55
56 563 10d), with an Eclogitic Unit covered by Maastrichtian deposits and Plio-Quaternary folded
57
58 564 polygenic conglomerates. The Sefidabeh basin is thrust over the HP-LT units. It comprises
59
60
61
62
63
64
65

1
2
3
4
5
6
7
8
9
10
11
12
13
14
15
16
17
18
19
20
21
22
23
24
25
26
27
28
29
30
31
32
33
34
35
36
37
38
39
40
41
42
43
44
45
46
47
48
49
50
51
52
53
54
55
56
57
58
59
60
61
62
63
64
65

565 Senonian turbidites with abundant calc-alkaline magmatic intrusions, lavas and volcano-
566 sedimentary rocks. The lowermost series is a polygenic Upper Cretaceous coarse conglomerate
567 (Fig. 10b). The Paleocene reef outlines west-vergent asymmetric folds (as in Figs. 10a, c).

7.6. Forg transect

569 Forg cross-section (Fig. 11f) is located to the southwest and almost continuous with the
570 Gazik cross-section but the part in between is not exposed. In the northeast, the Forg cross-
571 section exhibits Cretaceous phyllites unconformably overlain by an intensely deformed distal,
572 thinly bedded Paleocene sequence showing southwest-vergent asymmetric folds and a
573 pervasive sub-vertical schistosity. This transect is cut by the major Purang dextral strike-slip
574 fault and smaller conjugate sinistral and reverse faults outlining the existence of a flower
575 structure. Thrusts locally expose an ophiolitic unit, made of serpentized peridotite and
576 discontinuous horizons of pillow-lavas, below the Cretaceous sediments (Figs. 10g, h). In the
577 middle of the section, Paleocene deposits are directly found on top of the ophiolitic basement.
578 They are thrust over abundant Oligocene to Miocene lavas in the southern part. Some Plio-
579 Quaternary alkali-basalts are also present.

7.7. Birjand transect

581 Birjand cross-section (Fig. 9g) shows three main units stacked on top of one another and
582 was detailed before, when addressing the overall structure of the Birjand ophiolite (see section
583 6; Fig. 7). Peridotites of Unit 3 are thrust onto the Eocene sandy-limestone. Unit 2 is thrust over
584 Neogene conglomerates, testifying to the existence of recent deformation. This transect is
585 affected by large-scale sinistral strike-slip faults.

7.8. Ramengan transect

587 Ramengan cross-section (Fig. 11h) is separated from the Forg cross-section by an
588 extensive synclinorium of Neogene deposits (Fig. 4). In its southern part, the synclinorium is
589 cored by Eocene deposits showing two main lithologies, i.e. a turbiditic sequence and shaly

1 590 sediments. The shale deposits exhibit two orthogonal foliation planes. The Eocene lies
2 591 unconformably above Upper Cretaceous deposits or, locally, Paleocene sediments. Eo-
3
4 592 Oligocene magmatism is largely exposed (Fig. 10i). The Cretaceous deposits are pervasively
5
6
7 593 deformed, show southwest-vergent folds and are thrust over the northern flank of this
8
9
10 594 synclinorium (Figs. 10j, k). Serpentinite associated with basalts and/or radiolarites in the cores
11
12 595 of small thrust-related anticlines attests to the presence of an ophiolitic basement (Fig. 10l).
13
14 596 Paleocene sediments only crop out in the northern part of this cross-section.

16 597 7.9. Barak transect

18
19 598 This transect (Fig. 11i) exposes andalusite-bearing Jurassic metasandstones from the
20
21
22 599 Lut Block (Fig. 10m) and some marbles, both tilted to the north. The southern limit of the Neh
23
24 600 complex is marked by a hm-thick basalt succession. The contact between the Lut metasediments
25
26
27 601 and the Neh basalt is not well exposed and consists of basalts thrust onto metasediments. The
28
29 602 northern part of the Neh complex forms an antiformal stack with three main units: (1) a basal
30
31 603 unit composed by serpentinite intruded by gabbro and topped by pervasively deformed
32
33
34 604 Cretaceous sediments showing the highest Tmax determined by RSCM (between 460°C and
35
36 605 560°C); (2) a second unit showing amphibolite facies metatuffs and metabasalts capped by
37
38
39 606 peridotites (Figs. 10n-p); (3) on top, a third unit, mostly visible on the southern flank of the
40
41 607 antiform, is composed by strained amphibolites found immediately below peridotites.
42
43
44 608 Ultramafics are covered by Cretaceous sediments interlayered with basaltic lavas.

45
46 609 The core of this structure is intruded by a granitoid stock (Fig. 3q) affected by a slight
47
48
49 610 schistosity and locally lineated. It is dated from the base of the Eocene by Ar-Ar on biotite (see
50
51 611 below). A petrologically different muscovite-tourmaline-bearing granitic intrusion cuts across
52
53 612 the contact between the Neh complex and the Lut Block. It could belong the abundant Eo-
54
55
56 613 Oligocene magmatism observed in the area (Figs. 2a, 4).

614 **8. Metamorphic evolutions in the western part of the Sistan orogen**

1
2
3
4 615 This section focuses on two sets of metamorphic rocks found structurally below the Neh
5
6 616 ophiolite (Table 1; Figs. 10; see Figs. 2 for location): (1) those immediately underlying
7
8 617 peridotites, as do metamorphic soles (Wakabayashi and Dilek, 2000): amphibolite facies
9
10
11 618 metatuffs and metabasalts; lawsonite-bearing greenschist to blueschist facies metaradiolarites;
12
13 619 (2) metamorphic rocks present in the northern part of the Lut Block only: amphibolite to
14
15
16 620 granulite facies gneisses and metasediments (Deh-Salm area); pelitic metasediments showing
17
18 621 contact metamorphism. Blueschists and eclogites from the HP-LT zone were extensively
19
20
21 622 studied already and are not detailed here (Fotoohi Rad et al., 2005, 2009; Angiboust et al., 2013;
22
23 623 Bröcker et al., 2013; Kurzawa et al., 2017; Bonnet et al., 2018). Ocean-floor metamorphism
24
25 624 subsequent to ophiolite genesis (marked by amphibolitized gabbros, serpentinites) was briefly
26
27
28 625 presented in section 6.

30 626 8.1. Petrography

32 627 8.1.1. Birjand metasediments

34
35 628 Metamorphosed sediments were found within a tectonic slice between Units 2 and 3 in
36
37
38 629 the core of the Birjand ridge (Figs. 4, 7, 11g). Two main lithologies were observed (Table 1):
39

40 630 (1) Hm-scale boudins of metaradiolarites (Figs. 12a) composed of quartz and blue
41
42 631 amphibole associated with garnet, phengite, plagioclase, epidote, ilmenite, rare pyroxene and
43
44
45 632 retrograde chlorite. The schistosity is marked by the alignment of amphibole and phengite. The
46
47 633 same rock type was found as cm- to m-scale blocks in Eocene conglomerates (Mahmudali, Figs.
48
49
50 634 4; sample 15b-19).

51
52 635 (2) Clastic material within a carbonate matrix (Figs. 12b-d): (i) ophicalcite with
53
54 636 serpentine, magnetite, calcite, birefringent garnet and lawsonite; (ii) a basalt-rich breccia with
55
56
57 637 amphibole, titanite, calcite and lawsonite; (iii) a gabbro-rich breccia with calcite and lawsonite
58
59 638 in the matrix and plagioclase, clinopyroxene and lawsonite in the gabbroic clasts. Lawsonite
60
61
62
63
64
65

639 appears in equilibrium within both the clasts and the carbonate matrix, implying that the
1
2 640 brecciation occurred prior to the metamorphic event.
3

4 5 641 8.1.2. Amphibolite facies soles 6

7 642 Amphibolites and associated metasediments were collected in 10-20 m-thick horizons
8
9 643 below serpentinized peridotite in two distinct areas (Figs. 4, 10n-o-p, 11i), south of Barak and
10
11 644 to the north-east of Sahlabad, except for sample 14-01 which was found as a block in Eocene
12
13 645 conglomerates near Birjand). All of them exhibit a strong schistosity and lineation marked by
14
15 646 the orientation of amphibole (Figs. 12e-f).
16
17

18
19 647 Amphibolites comprise amphibole, plagioclase, accessory ilmenite (Table 1; samples
20
21 648 14-01, 16-45b; Figs. 12e) and secondary phases such as titanite, epidote and quartz. Some
22
23 649 additionally contain clinopyroxene (samples 14-11b2 to 17-18; Figs. 12g-h), either in the
24
25 650 foliation or present as boudins (in association with Ca-rich garnet).
26
27

28
29 651 Metasediments (samples 14-07, 14-23a, 16-80) are composed of quartz, and
30
31 652 phyllosilicates, i.e. white micas or biotite and retrograde chlorite. Two of them, which contain
32
33 653 organic matter, provided RSCM maximum temperatures of 515°C on average (Fig. 6).
34
35

36 654 8.1.3. Metamorphic rocks of the Lut block at the boundary with the Neh complex 37

38
39 655 These samples correspond to micaschists showing three mineral assemblages: (i) the
40
41 656 first one (Figs. 12i) is made by biotite and occasional garnet inclusions in andalusite (sample
42
43 657 16-74); (ii) the second one shows the destabilization of andalusite into sillimanite, associated
44
45 658 with white micas and biotite (Figs. 12i-j); (iii) the last one consists of biotite which marks the
46
47 659 main foliation, quartz and sometimes plagioclase (Figs. 12i-j). Accessory phases such as
48
49 660 tourmaline, Fe-Ti oxide, zircon and organic matter are present (Table 1).
50
51

52 53 661 8.1.4. Metamorphic rocks of the Lut Block: Deh-Salm complex 54

55
56 662 Rocks from the Deh-Salm metamorphic complex were reported during the mapping
57
58 663 programme in the 1970s and dated at ~165-160 Ma by Mahmoudi et al. (2010), yet their P-T
59
60
61
62
63
64
65

664 conditions and path are still poorly constrained. Three types of metamorphic rocks were
1 distinguished in this area:
2
3

4 (1) Micaschists in the northern part of the Deh-Salm complex, together with marbles
5
6
7 667 and metasandstones. Micaschists consist of quartz, biotite forming the foliation, plagioclase,
8
9
10 668 frequently associated with white mica, sillimanite and sometimes orthoclase. Tourmaline, rutile
11
12 669 and titanite are the main accessory phases. Biotite and white mica are altered into chlorite and
13
14 670 kaolinite, respectively.
15

16 (2) Migmatites exposed in the southern part of the Deh-Salm complex (Fig. 12k-n)
17
18
19 672 showing three successive parageneses: (i) the earliest is made of kyanite, garnet, biotite and
20
21
22 673 white mica (Figs. 12k-l); (ii) the second one comprises quartz, plagioclase and fibrous
23
24 674 sillimanite parallel to the main foliation and appears contemporaneous with formation of the
25
26
27 675 leucosome (Figs. 12l-m-n); (iii) the latest one comprises an association of prismatic sillimanite
28
29 676 associated with white mica and some biotite crosscutting the main foliation (Figs. 12n), which
30
31 677 likely postdates melting. Accessory minerals are tourmaline and Fe-Ti oxide (Table 1).
32

33 (3) Amphibolites, found as lenses into metasediments, comprising amphibole,
34
35
36 679 plagioclase and clinopyroxene associated with some epidote and titanite.
37

38 680 8.2. Mineral chemistry

41 681 Representative microprobe analysis are available on supplementary material 2.

42 682 8.2.1. Birjand metasediments

43
44
45
46 683 Results for three metaradiolarite samples (Fig. 13a; supplementary material 1) show that
47
48
49 684 blue amphibole is riebeckite ($\text{Na}_B \geq 1.5$, $(\text{Na}+\text{K})_B < 0.5$; $\text{XMg} < 0.5$; $\text{Fe}^{3+}/(\text{Fe}^{3+}+\text{Al}) > 0.5$; Si
50
51 685 between 7.5 and 8). White micas are phengitic with Si between 3.05 and 3.6 and XMg between
52
53
54 686 0.35 and 0.6. Garnet is manganese-rich ($\geq 38\%$ of spessartine endmember). Clinopyroxene from
55
56 687 sample 15b-19 corresponds to omphacite. Felspar in sample 15b-19 is pure albite. Chlorite
57
58
59
60
61
62
63
64
65

688 is close to the clinocllore end-member ($\geq 75\%$) with Si between 2.75 and 3.15 and XMg from
689 0.4 to 0.85.

690 The studied metagabbroic clasts show that clinopyroxene lies between the aegyrine-
691 augite and omphacite fields. Plagioclase is again pure albite. Chlorite is clinocllore with Si
692 between 2.85 and 3.175 and XMg from 0.45 to 0.9. Serpentine from the adjacent
693 metaophicalcite (sample 16-21b), determined through Raman spectroscopy corresponds to
694 lizardite. Likewise, the nature of the carbonate matrix of the opicalcite (16-21b) was
695 determined to be calcite.

8.2.2. Amphibolite facies soles

697 Microprobe analyses were performed on twelve amphibolites and one metasediment
698 (14-07; Figs. 13b, supplementary material 1). Amphibole is calcic and corresponds to Mg-
699 hornblende, except for some crystals trending towards the tschermakite or tremolite end-
700 members. XMg ranges between 0.4 and 0.85. While the composition is fairly homogeneous in
701 each sample, a wide range of compositions is observed from one sample to the other (Figs. 13b)
702 yet without clear spatial correlations between samples from the north-east (Sahlabad) to the
703 south (Barak). Feldspar is dominantly plagioclase, most commonly around 65% albite, yet
704 spanning the full range of compositions (from 94% anorthite to 98% albite). Four samples
705 contain minor amounts of K-feldspar.

706 Pyroxene is diopsidic in the four analysed samples (14-11b, 14-20, 14-26a and 17-18),
707 except in sample 14-20 where it is richer in Al and Na and poorer in Ca (i.e., with an augitic
708 composition close to that of sample 16-01c). Garnet (sample 14-11b) is intermediate between
709 grossular and andradite. White mica is slightly phengitic, with Si varying between 3.1 and 3.2
710 in the metasediment (with XMg ~ 0.6). In amphibolites, Si varies from 3.2 to 3.4 and XMg from
711 0.45 to 0.85. Biotite (14-18) has a XMg of 0.65 and Si of 2.8. Epidote is close to the ferric end-
712 member. Chlorite is close to clinocllore composition.

713 Trace element composition of titanites, in particular the Zr content, was obtained via
1
2 714 laser ablation split-stream inductively coupled plasma mass spectrometry (Figs. 13b; see LASS-
3
4 715 ICPMS methodology in Appendix). Mean values of the Zr content range between 110 and 185
5
6
7 716 ppm (14-09: 154 ppm, for a 114-216 range; 14-18: 111 ppm, 42-192 range; 16-42: 158 ppm,
8
9 717 35-460 ppm range; 17-18: 184 ppm, 80-339 ppm range).

12 718 8.2.3. Metamorphic rocks of the Lut block at the boundary with the Neh complex

14 719 Biotite has a XMg ranging between 0.35 and 0.5 and Si between 2.5 and 2.9 (Figs. 13c,
15
16
17 720 supplementary material 1), with homogeneous composition in each of the three studied samples.
18
19 721 Other minerals correspond to en-membre compositions: albite, muscovite, almandine (sample
20
21 722 16-74). Chlorites are clinoclone. Andalusite is partially replaced by sillimanite. Andalusite is
22
23
24 723 stable with garnet (for 16-74, Fig. 12i) and biotite, whereas sillimanite appears in equilibrium
25
26 724 with muscovite and biotite. The two texturally distinct biotite generations have the same
27
28
29 725 composition however.

31 726 8.2.4. Metamorphic rocks of the Lut Block: Deh-Salm complex

33
34 727 Measurements were performed for three micaschists (16-54, 55, 57), one migmatite (14-
35
36 728 29) and one amphibolite (16-56; Figs. 11d; supplementary material 1). Biotite shows XMg
37
38
39 729 values between 0.35 and 0.45 and Si between 2.55 and 2.9, except for samples 16-57 and partly
40
41 730 16-54 (XMg ~0.55). Chemical mapping (sample 14-29a) confirms the textural difference
42
43
44 731 observed between biotite crystals: biotite associated with garnet has $\text{XMg} \geq 0.4$, whereas biotite
45
46 732 replacing garnet has $\text{XMg} < 0.4$. Garnet from sample 14-29a are almandine-rich and
47
48
49 733 homogeneous, except for a small rim exhibiting Mn-enrichment. Feldspar is mainly Na-rich
50
51 734 plagioclase, with 50% to 100% albite end-member. Sample 16-57 also contains K-feldspar.
52
53 735 Plagioclase in amphibolite (16-56) exhibit a wide range of compositions between 42% and 96%
54
55
56 736 of albite end-member.

737 White mica is moderately phengitic. Si varies between 3 and 3.2, with rare values up to
1
2 738 3.4 and XMg ranges between 0.35 and 0.65. In sample 14-29a, white mica with the highest Si
3
4 739 contents (>3.05) is associated with garnet, kyanite and biotite ($\text{XMg}>0.4$), whereas others are
5
6 740 associated with retrograde sillimanite and biotite ($\text{XMg}<0.4$). Amphibole from sample 16-56 is
7
8
9 741 Mg-hornblende with a XMg between 0.5 and 0.7.

12 742 8.3.P-T estimates

14 743 8.3.1. Birjand metasediments

16 744 Only approximate P-T conditions can be determined for these rocks, although their
17
18
19 745 mineralogy hints to HP-LT conditions, as shown by the high Si content in phengite (up to 3.57
20
21 746 apfu) and the presence of omphacite in metaradiolarites, and the presence of lawsonite and
22
23
24 747 omphacite in metamafic rocks. P-T conditions are bracketed by the stability fields of lawsonite,
25
26 748 calcite and lizardite to lie between 150 and 300°C and 0.2 to 0.6 GPa (Fig. 14a).

29 749 8.3.2. Amphibolite facies soles

31 750 Plagioclase-amphibole geothermobarometry on eleven amphibolite samples gives a
32
33
34 751 large range of P-T conditions, with an average value at $730^{\circ}\text{C} \pm 40^{\circ}\text{C}$ and $0.65 \text{ GPa} \pm 0.2 \text{ GPa}$
35
36 752 (Figs. 14b). Samples from the south (in blue) or the north (in green) cannot be distinguished.
37
38
39 753 Thermobarometry based on the Zr content in titanite (Hayden et al., 2008; $\text{Zr} \sim 150\text{-}200$ ppm
40
41 754 for the samples, with estimated silica and titania activities of 1) is consistent with the results of
42
43 755 plagioclase-amphibole thermobarometry.

46 756 Thermodynamic modelling was performed for sample 15b-15c (bulk composition
47
48 757 available on supplementary material 3). Based on Ti and Si isopleths of amphibole and the
49
50
51 758 absence of melting, P-T conditions can be estimated at around 700°C and 0.6 GPa (green
52
53 759 rectangle on Figs. 14b), hence undistinguishable from the average P-T conditions estimated by
54
55 760 plagioclase-amphibole thermobarometry on 8 amphibole-plagioclase pairs in this sample (714
56
57
58 761 $\pm 40^{\circ}\text{C}$, $0.54 \pm 0.2 \text{ GPa}$; black rectangle on Figs. 14b). The predicted modes of the main phases
59
60
61
62
63
64
65

762 agree well with the observed mineralogy: between 40 and 45% of plagioclase, 40 to 45% of
1
2 763 amphiboles. Pseudosection modelling also predicts presence of biotite <2% and augite <7%
3
4 764 which have not been observed on thin-section (presumably due to their low abundance and/or
5
6
7 765 potential retrogression).
8

9 766 8.3.3. Metamorphic rocks of the Lut block at the boundary with the Neh complex

10
11
12 767 Thermodynamic modelling for sample 16-72 (Fig. 14c, bulk composition available on
13
14 768 supplementary material 3) allows constraining P-T conditions for the two main parageneses
15
16
17 769 observed, i.e. (1) the biotite-andalusite assemblage (red field; Fig. 14c) and (2) the white mica,
18
19 770 sillimanite and biotite assemblage (blue field; Fig. 14c). These P-T conditions are consistent
20
21
22 771 with the results of the garnet-biotite thermometry for sample 16-74 ($600-650^{\circ}\text{C} \pm 25^{\circ}\text{C}$). The
23
24 772 P-T position of the two paragenesis initiates an anticlockwise P-T path.

25 26 773 8.3.4. Metamorphic rocks of the Lut Block: Deh-Salm complex

27
28
29 774 Thermometry based on the Ti content of biotite in four samples reveals the existence of
30
31 775 two clusters of temperature (Figs. 12d), at $670^{\circ}\text{C} \pm 30^{\circ}\text{C}$ and $740^{\circ}\text{C} \pm 20^{\circ}\text{C}$. GBAQ
32
33
34 776 geobarometry coupled with garnet-biotite geothermometry shows that the P-T conditions of the
35
36 777 kyanite-garnet-biotite-phengite-bearing assemblage of sample 14-29a lie in the range 640-
37
38
39 778 $670^{\circ}\text{C} \pm 25^{\circ}\text{C}$ and $0.75-0.85 \text{ GPa} \pm 0.2 \text{ GPa}$ (Figs. 12d).
40

41 779 Thermodynamic modelling was performed for the migmatitic sample 14-29a (Figs. 14d,
42
43 780 bulk composition available on supplementary material 3). Caution is needed since the overall
44
45
46 781 chemistry may have been modified by partial melting. This does not apply, however, to the
47
48
49 782 paragenesis postdating melting (i.e., with prismatic sillimanite, white mica and biotite), which
50
51 783 yields conditions between 590 and 670°C and 0.35 to 0.6 GPa (blue field Figs. 14d). Small
52
53 784 garnet amounts are predicted (<2%) but probably too low to be observed on thin-section.
54
55
56 785 Conditions for the quartz-plagioclase-sillimanite leucosome lie above 690°C . Results of Ti-in-
57
58 786 biotite thermometry ($\sim 740^{\circ}\text{C}$) provide rough pressure estimate around 0.7 GPa (red circle on
59
60
61
62
63
64
65

787 Figs. 14d). The estimate for the early quartz-biotite-sillimanite-garnet-kyanite-
1
2 788 plagioclase±rutile paragenesis (~670°C, 0.8 GPa) lies close to the P-T conditions determined
3
4 789 using GBAQ/GB geothermobarometry, suggesting only minor modification of the overall
5
6
7 790 chemistry by partial melting. The succession of these mineral assemblages suggests a clockwise
8
9
10 791 P-T path (black dotted line, Figs. 14d).

13 792 **9. Geochronology**

16
17 793 Rocks corresponding to four domains have been dated. Figs. 15 gathers all the results
18
19 794 of our dating. All uncertainties are given as $\pm 2\sigma$ in the text.

21
22 795 - Ophiolitic rocks of the Neh complex

23
24 796 $^{40}\text{Ar}/^{39}\text{Ar}$ step-heating of amphiboles from the amphibolitic gabbro 15b-18 provided a
25
26
27 797 plateau age of 106.3 ± 3.1 Ma (Figs. 15a) that includes 100% of released ^{39}Ar .

28
29 798 - Birjand metasediments

30
31 799 $^{40}\text{Ar}/^{39}\text{Ar}$ step-heating of phengite from two metaradiolarite samples 14b-14 and 15b-
32
33
34 800 19 yielded by plateau ages of 72.2 ± 0.3 and 74.1 ± 0.3 Ma that includes 100% and 98.43% of
35
36 801 released ^{39}Ar respectively (Figs. 15b and c).

37
38
39 802 - Amphibolitic sole and associated rocks of the Neh complex

40
41 803 Datings on amphibolite give three populations of ages:

42
43 804 (1) The oldest was obtained on sample 14-18 (collected close to Sahlabad) by in-
44
45
46 805 situ U-Pb on 46 grains of titanite which yielded a Tera-Wasserburg isochron age of
47
48 806 108.6 ± 4.5 Ma (Figs. 15d);

49
50
51 807 (2) Intermediate ages were obtained on two samples collected close to Sahlabad
52
53 808 which gave two indistinguishable ages: one by $^{40}\text{Ar}/^{39}\text{Ar}$ step heating method on amphibole
54
55
56 809 provided a plateau age of 72.4 ± 0.6 that includes 100% and ^{39}Ar (Figs. 9e) and another by
57
58
59
60
61
62
63
64
65

810 in-situ U-Pb on 46 grains of titanite yielded a Tera-Wasserburg isochron age of 72.2 ± 2.1
1
2 811 Ma (Figs. 9f).

3
4 812 (3) The youngest ages were obtained on four samples collected in the area of Barak
5
6
7 813 which gave five indistinguishable ages: three obtained by $^{40}\text{Ar}/^{39}\text{Ar}$ step heating method
8
9 814 on amphibole provided age at 53.4 ± 1.7 , 54.9 ± 2.6 , 52.9 ± 0.5 Ma that includes 89%,
10
11 815 62.91% and 85.37% of released ^{39}Ar respectively (Figs. 13g, h and i) and two obtained by
12
13 816 in-situ U-Pb on 29 (14-09) or 45 (17-18) grains of titanite yielded Tera-Wasserburg
14
15 817 isochron ages of 54.1 ± 11.4 and 51.5 ± 1.4 Ma (Figs. 13g to k).

16
17
18
19 818 For the sample 14-09 the age obtained by Ar-Ar and U-Pb are undistinguishable,
20
21 819 respectively at 53.4 ± 1.7 and 54.1 ± 11.4 Ma while for sample 14-18 $^{40}\text{Ar}/^{39}\text{Ar}$ step heating
22
23 820 method on amphibole provide a 72.4 ± 0.6 Ma age significantly different from the U-Pb on
24
25 821 titanite ages obtained at 108.6 ± 4.5 Ma.

26
27
28
29 822 Interestingly, in the area of Mahmudali, amphibolite were collected close to an intrusive
30
31 823 and deformed granodiorite which was dated by $^{40}\text{Ar}/^{39}\text{Ar}$ step heating method on biotite
32
33 824 providing an age of 49.6 ± 0.2 Ma that includes 83.46% of released ^{39}Ar (Figs. 13l).

34
35
36 825 - Metamorphic rocks of the Deh-Salm metamorphic complex

37
38
39 826 14-29 migmatite sample have been dated by $^{40}\text{Ar}/^{39}\text{Ar}$ step heating method on biotite at
40
41 827 150.0 ± 0.5 Ma that includes 76.68% of released ^{39}Ar (Figs. 9m).

42 43 44 828 **10. Discussion**

45
46
47
48 829 10.1. Overall structure of the northern Sistan orogen: major tectonic domains,
49
50
51 830 boundaries and significance

52
53 831 Observations gathered from field investigations, from the different cross-sections and
54
55 832 collected samples, together with data recently published by this group (Jentzer et al., 2017,
56
57 833 2020; Bonnet et al., 2018), are combined into a synthetic SW-NE crustal-scale section of the
58
59
60
61
62
63
64
65

834 northern Sistan orogen (Fig. 16; see profile location on Figs. 4). Some first-order characteristics
1
2 835 and the relationships between the domains can be outlined:
3

4
5 836 - The HP-LT zone crops out as a series of discontinuous tectonic windows and marks the
6
7 837 location of the suture zone. Early tectonic stacking and later doming characterize this domain
8
9 838 (Bonnet et al., 2018). The suture zone contact is reworked by steeply dipping faults at present.
10

11
12 839
13
14 840 - The Afghan block, onto which the Sefidabeh basin developed, occupies the highest
15
16 841 structural position. Cross-sections evidence a widening of the Sefidabeh basin towards the
17
18 842 south, consistent with its larger extension in the southern Sistan orogen (Mohammadi et al.,
19
20 843 2016; Bagheri and Damani Gol, 2020). The Afghan block also preserves evidence for Early
21
22 844 Cretaceous (or earlier) normal faulting, which could reflect thinning of the continental margin
23
24 845 (see also Tirrul et al., 1983). The Western Unit, which is sandwiched between the HP-LT zone
25
26 846 and the Neh complex and corresponds to an unmetamorphosed ophiolitic sequence cross-cut
27
28 847 by Late Cretaceous adakitic lavas (~86-71 Ma; Zarrinkoub et al., 2012b; Jentzer et al., 2020), is
29
30 848 interpreted as a forearc of the Sistan subduction zone, possibly a reworked portion of the former
31
32 849 ocean-continent transition on the Afghan passive margin side.
33
34
35
36
37

38
39 850 - The Neh complex preserves a relatively continuous obducted ophiolite, 50 to 80 km large
40
41 851 across the profile (>100 km along strike; Figs. 16). Despite post-emplacement deformation of
42
43 852 the ophiolite thrust sheet, distinct km-scale units evidence lateral contrasts within the former
44
45 853 seafloor reminiscent of modern-day slow- to ultra-slow-spreading environments (e.g. Cannat et
46
47 854 al., 2009, Picazo et al., 2012; Escartín et al., 2017): discontinuous and highly variable pillow-
48
49 855 lava thicknesses, isolated masses of gabbro intruding serpentized peridotite, opicalcite or
50
51 856 brecciated basalt and gabbro (i.e., mass wasting deposits) directly atop serpentized peridotite,
52
53
54
55 857 together with a lack of sheeted dyke complex. $^{40}\text{Ar}/^{39}\text{Ar}$ age dating of an amphibolitized gabbro
56
57
58
59
60
61
62
63
64
65

1 858 yielded 106 ± 3 Ma (Figs. 15a), close to the U-Pb zircon dating of oceanic leucogabbros (~110
2 859 Ma; Zarrinkoub et al., 2012a).

3
4 860 - The Neh ophiolitic complex is thrust to the SW over the Lut Block and overlain by the
5
6
7 861 Ratuk complex or the Afghan Block (i.e., locally by the Western unit). A series of major NE-
8
9 862 dipping contacts, parallel to the main tectonic contact marking the suture zone, are observed
10
11 863 throughout this oceanic complex (Fig. 16). Sediments deposited onto the ophiolitic Neh
12
13 864 complex indicate a progressive southwestward migration of the depocenter with time. The
14
15 865 sedimentary thickness of the Paleocene and Eocene basins of the Neh complex, based on the
16
17 866 maximum temperature experienced by the sediments ($\sim 275^{\circ}\text{C}$ on average), could be on the
18
19 867 order of ~ 5 km assuming a $50^{\circ}\text{C.km}^{-1}$ thermal gradient. Such a relatively warm gradient is
20
21 868 similar to that of the upper continental crust of Central Tibet (Zhi Min and Wu, 1987) and
22
23 869 justified by the likely high heat flow associated with the profuse magmatic activity postdating
24
25 870 the Paleo/Eocene (Pang, 2013), or by the present-day value ($84\text{-}103 \text{ mW m}^{-2}$; Davies, 2013).
26
27 871 This thickness broadly agrees with the value proposed by Tirrul et al. (1983; ~ 4 km).
28
29
30
31
32

33
34 872 The overall structural organization and the fact that all the main contacts are dipping
35
36 873 towards the NE are consistent with (i) a SW vergence of the orogen, (ii) a general underthrusting
37
38 874 of the Neh complex below the Afghan block and (iii) the existence of a former NE dipping
39
40 875 subduction. The latter was already proposed by Tirrul et al. (1983) and is strengthened by the
41
42 876 location of a Late Cretaceous magmatic arc to the east of the suture zone (Jentzer et al., 2020).
43
44 877 The southwestward shift of depocenters suggests an “en sequence” migration of the flexure in
45
46 878 the lower plate with respect to the suture zone.
47
48
49
50

51 879 The series of thrusts marking the emplacement of the oceanic Neh complex onto the Lut
52
53 880 block are cross-cut by lowermost Eocene acidic intrusions ($\sim 55\text{-}50$ Ma). This indicates that
54
55 881 final closure of the Sistan marginal basin was completed by then.
56
57
58
59
60
61
62
63
64
65

882 Collisional shortening is probably relatively modest: structures associated with early
1
2 883 shortening like ophiolite sheets are well-preserved (Figs..7, 8), and the continental basement of
3
4 884 the Lut block is not exposed below the Neh complex, suggesting that thick-skin deformation is
5
6
7 885 insignificant and that the basement may not be significantly involved in the deformation.
8
9 886 However, the extension of the Lut block below the Neh complex (Fig. 16; and the thickness of
10
11
12 887 the Neh ophiolite, probably ~12 km at the onset of obduction processes; see below) is unknown.
13
14 888 Based on gravimetric data, Mousavi and Ebbing (2018) and Eshagh et al. (2019) estimated that
15
16 889 the thickness of the CEIM crust lies between 40 and 45 km with a slight increase up to 52 km
17
18
19 890 below the Sistan orogen, which would be consistent with some minor implication of the
20
21
22 891 basement of the Lut Block basement at depth. Shortening also varies along strike, as shown by
23
24 892 the increase of deformation of the Sefidabeh domain towards the N indicating a greater
25
26
27 893 shortening in the northern part of the orogen (see below).

28
29 894 In the absence of clear stratigraphic markers allowing to perform balanced cross-sections,
30
31 895 and because of the intensity of ductile deformation in the Cretaceous to Paleocene flyschs and
32
33 896 phyllites (as underlined by a well-developed schistosity; Figs. 5m, n), estimating the amount of
34
35
36 897 shortening in the Sistan orogen is fraught with large uncertainties. A crude unfolding of
37
38
39 898 ophiolite sheets and deformed basins suggests a minimum estimate of 80-100 km for the
40
41 899 obduction overthrust onto the Lut block, and 30-50 km since final closure of the oceanic realm.
42
43
44 900 We note that part of the first estimate may also have been acquired after closure.

45
46 901 10.2. Geodynamic significance of metamorphic rocks from the Neh complex and Lut
47
48 902 block

49
50
51 903 10.2.1. Neh complex: evidence for intra-oceanic slicing and metamorphic sole
52
53 904 formation during the onset of obduction
54
55
56
57
58
59
60
61
62
63
64
65

905 In addition to mineral transformations associated with oceanic deformation (see section 6)
1
2 906 and/or hydrothermal alteration (Tirrul et al., 1983; Saccani et al., 2010; Zarrinkoub et al.,
3
4 907 2012a), two new types of mineral recrystallization are reported here in the Neh complex:
5
6

7 908 (1) Strongly schistosed amphibolite facies metabasic and metasedimentary rocks, mostly
8
9 909 metatuffs showing a marked lineation in places (Figs. 10o), are found as a 10-20 m thick
10
11 910 horizons below the ophiolite (Figs. 10n, 11i, 16), particularly its southernmost exposures or
12
13 911 near Sarbisheh (Figs. 4). Their metamorphic peak, based on thermodynamic modelling,
14
15 912 amphibole-plagioclase thermobarometry and Zr content in titanite, lies at $700^{\circ}\text{C} \pm 50$ and ~ 0.6 -
16
17 913 0.7 GPa (e.g., sample 15b-15c; Figs. 14b). Such characteristics suggest that these rocks
18
19 914 represent a former metamorphic sole (Wakabayashi and Dilek, 2003; Agard et al., 2016), whose
20
21 915 P-T conditions are intermediate between that of granulite facies HT soles (i.e., clinopyroxene-
22
23 916 garnet bearing soles; Soret et al., 2017) and greenschist facies LT ones. Their protolith is also
24
25 917 intermediate in composition (Agard et al., 2020).
26
27
28
29
30

31 918 Since metamorphic soles mark the initiation of intra-oceanic subduction (e.g.,
32
33 919 Wakabayashi and Dilek, 2003; Agard et al., 2016; Plunder et al., 2016; Guilmette et al., 2018;
34
35 920 Dubacq et al., 2019), their age is an important constraint for the geodynamic evolution of the
36
37 921 Sistan orogen. $^{40}\text{Ar}/^{39}\text{Ar}$ step heating on amphibole and in-situ U-Pb on titanite yielded three
38
39 922 age populations for the metamorphic sole (Figs. 15d-k):
40
41
42

43 923 - two ages around 72 Ma, obtained by different methods on distinct samples (72.4 ± 0.6
44
45 924 Ma: $^{40}\text{Ar}/^{39}\text{Ar}$ step heating on amphibole, sample 14-18; 72.2 ± 1.1 Ma: in situ U-Pb on 59
46
47 925 titanite grains, sample 16-42; Figs. 15e-f).
48
49

50 926 - five ages between ca. 52 and 55 Ma (Figs. 15g-k), for samples collected in the vicinity of
51
52 927 the large granitoid intrusions cutting across the sole (Figs. 10q, 11i, 16). These ages correspond
53
54 928 within error to the ca. 50 Ma ages obtained for the granitoids (Fig. 15l) and are thus interpreted
55
56 929 as reflecting recrystallization (of amphibole or titanite) during the magmatic event.
57
58
59
60
61
62
63
64
65

930 - one U-Pb titanite age at 108 ± 2 Ma (Fig. 15d), which is undistinguishable from the one
1
2 931 obtained for the amphibolitic gabbro dated at 106 ± 3 Ma (Fig. 15a), and therefore interpreted
3
4 932 as inherited from the oceanic activity.
5
6

7 933 We infer that the two ca. 72 Ma dates, which cannot be linked to any geological event
8
9 934 reported so far in the Sistan orogen, correspond to the age of peak metamorphism for the
10
11 935 metamorphic soles. If confirmed (see below), this constrains the onset of intra-oceanic
12
13 936 subduction within the Sistan ocean and the start of the obduction process. This age lies between
14
15 937 (i) the 86 ± 3 Ma peak burial of the suture zone eclogites, which attest to already ongoing E-
16
17 938 dipping subduction below the Afghan Block, and (ii) final closure of the Sistan oceanic realm
18
19 939 at ~ 55 -50 Ma, as revealed by granitoid intrusions (e.g., sample 14-08) cross-cutting both the
20
21 940 Lut Block and the ophiolite, and by the presence of Eocene continental molasse-type sediments
22
23 941 (see below).
24
25
26
27
28

29 942 (2) Lawsonite-bearing rocks were found, in the mountain ridge south of Birjand, at the base
30
31 943 of the ophiolitic Unit 2 (Figs. 7, 11g). The presence of lawsonite, in both gabbro clasts and in
32
33 944 the carbonate matrix of an oceanic breccia, advocates for peak metamorphic conditions around
34
35 945 250°C and 0.4 GPa, at the transition between greenschist and blueschist facies conditions.
36
37 946 Further evidence for metamorphic recrystallization and similar burial is provided by the
38
39 947 presence of a phengite, spessartine-rich garnet, ferric blue amphibole and Al-bearing pyroxene
40
41 948 assemblage in nearby metaradiolarites (Figs. 13a). $^{40}\text{Ar}/^{39}\text{Ar}$ step heating of phengite from two
42
43 949 distinct metaradiolarite samples, located in the same structural position as the lawsonite-bearing
44
45 950 ones, yielded 74.1 ± 0.3 Ma and 72.2 ± 0.3 by $^{40}\text{Ar}/^{39}\text{Ar}$ step heating (Figs. 15b, c). These ages
46
47
48
49 951 are similar to those obtained for the metamorphic sole.
50
51
52

53 952 These metamorphic rocks collectively provide evidence for a specific deformation event
54
55 953 occurring within the Sistan ocean during the Upper Campanian. We propose that this tectono-
56
57 954 metamorphic event marks the initiation of intra-oceanic thrusting (and/or subduction), whose
58
59
60
61
62
63
64
65

955 amplitude was larger in the eastern part of the study area (metamorphic soles; Sarbisheh,
1
2 956 Malabad) than in the west (lawsonite-bearing samples; Birjand ridge).

3
4 957 Incidentally, the presence of lawsonite-bearing rocks places constraints on the thickness of
5
6
7 958 the ophiolitic material above, around 12-15 km at the time.

8
9 959 10.2.2. Lut Block contact metamorphism associated with Lower Eocene
10
11
12 960 intrusions?

13
14 961 Metapelites located near the contact between the obducted Neh ophiolitic complex and the
15
16
17 962 Lut Block show mineral assemblages indicative of contact metamorphism. Two main rock
18
19 963 types are observed:

20
21 964 (1)The most common type contains quartz, biotite, plagioclase and andalusite. P-T
22
23
24 965 conditions are estimated between 600 and 650°C and are lower than 0.3 GPa (red area on Figs.
25
26 966 14c). Whilst sedimentary layering is still visible, these rocks are slightly deformed and located
27
28
29 967 near granitoid intrusions. This assemblage therefore likely reflects contact metamorphism and
30
31 968 syn-kinematic growth during granitoid emplacement, at 49.6 ± 0.2 Ma (Fig. 15l).

32
33
34 969 (2)The second type comprises sillimanite overgrowing andalusite, white mica, plagioclase,
35
36 970 biotite and quartz. It is stable in similar but slightly higher P-T conditions, between 625 and
37
38
39 971 650°C and between 0.3 and 0.4 GPa (blue area on Fig. 14c). This second type may reflect a
40
41 972 stronger impact of contact metamorphism and/or additional thrusting following collision. The
42
43
44 973 latter interpretation would be consistent with the existence, in places, of a foliation affecting
45
46 974 granitoid intrusions, which advocates for some post-intrusion syn-collisional deformation.

47
48 975 In the absence of age constraints for these metamorphic rocks, we cannot rule out, however,
49
50
51 976 that their metamorphism could be older than the granitoid intrusions, especially because of their
52
53 977 similarity with some of the Jurassic metamorphic rocks of Anju or Dehsalm (Lut Block; see
54
55 978 below).

10.2.3. Lut Block Deh-Salm metamorphic complex: mid- to late-Jurassic (“Mid“-
Late-Cimmerian) regional metamorphism

The Deh-Salm metamorphic complex hosts amphibolites and metasediments exhibiting variable metamorphic degrees, from slightly deformed micaschists to migmatites showing an abundant leucosome and a strongly schistosed melanosome. In the migmatitic zone, the P-T-time path determined for the garnet-kyanite-biotite-plagioclase-phengite-bearing sample 14-29 shows three successive conditions (Figs. 14d): ~675°C and ~0.8 GPa for the peak of pressure, followed by a temperature increase associated with partial melting at around 725°C and 0.75GPa, and then retrograde conditions at 650°C and 0.4 GPa. ⁴⁰Ar/³⁹Ar step heating on biotite gave an age of 149.6 ± 0.5 Ma for this sample (Fig. 15m).

This metamorphic evolution is consistent with the regional metamorphism described by Masoudi et al. (2006; these authors also report contact metamorphism near granitic intrusions and thermal metamorphism marked by andalusite, sillimanite, and orthoclase isograds), with conditions increasing from chlorite-bearing rocks in the NE to staurolite-garnet-biotite-bearing amphibolite facies rocks in the SW. Our pressure estimates are higher than those obtained by Mahmoudi et al. (2010; 680°C and 0.35 GPa), possibly because these authors did not consider the presence of kyanite.

These previous studies (Mahmoudi et al., 2010; Masoudi et al., 2006) proposed that the protolith of the Deh-Salm complex is the Shemshak formation, i.e. the extensive Upper Triassic to Middle Jurassic siliciclastic formation covering most of northern Iran following Paleotethys closure, including the Lut Block. Based on U-Pb zircon and titanite dating of amphibolites and U-Pb monazite dating of metapelites (Mahmoudi et al., 2010), regional metamorphism is constrained between 165 and 160 Ma, and therefore Mid-Cimmerian. This age range overlaps with the 165 to 163 Ma ages obtained by U-Pb zircon or monazite dating (Mahmoudi et al., 2010) and Rb-Sr whole-rock dating of the nearby granitic intrusions (Esmaeily et al., 2005). Nd

1004 and Sr isotopes furthermore support an upper crustal source for these intrusions, suggesting that
1
21005 they derive from the partial melting of metasediments (Esmaeily et al., 2005).
3

4
51006 A similar metamorphic setting was described by Bröcker et al. (2014) north of Birjand, in
6
71007 the Anjul area: protoliths were attributed to the Semshak formation and migmatites and granitic
8
91008 intrusions dated by U-Pb (on zircon cores from leucosomes) between 169 and 168 Ma, thus
10
11
121009 close to the age of Deh-Salm regional metamorphism. In the case of Anjul, two younger ages
13
14
151010 were also obtained: ~110 Ma, by U-Pb dating of zircon overgrowths, and 102-96 Ma by Rb-Sr
16
171011 on K-feldspar or biotite separates. Bröcker et al. (2014) interpreted these two Cretaceous ages
18
191012 as marking the opening of the Sistan ocean and the cooling of the passive margin, respectively.
20

21
221013 In this framework, our 149.6 ± 0.5 Ma Ar/Ar dating of biotite appears younger than the
23
241014 165-160 Ma age proposed for regional metamorphism (Mahmoudi et al., 2010) yet older than
25
26
271015 the 110 Ma age thought to reflect the rifting stage (Bröcker et al., 2014). Although further age
28
291016 determinations are needed, this plateau age precludes mixing of different biotite populations
30
31
321017 and thus seems to reflect a distinct thermal event. We tentatively propose that this ~150 Ma
33
341018 event could represent cooling of regional metamorphic rocks or, since age constraints on
35
361019 gabbros and radiolarites suggest that the Sistan ocean is already open by ~120-110 Ma, a
37
38
391020 thermal event associated with the onset of rifting.
40

411021 10.2.4. Summary of the main metamorphic events recorded in the Sistan orogen 42

43
441022 Figure 17 summarizes the major metamorphic events associated with the Sistan orogeny.
45
461023 Whether the older, ~150 Ma age reflects a thermal event associated with rifting or cooling of
47
48
491024 the older Mid-Late-Cimmerian regional metamorphism of Deh-Salm is unclear. The oldest
50
511025 Sistan metamorphism, at ~106 Ma, corresponds to amphibolite facies recrystallization of
52
53
541026 oceanic gabbros (see section 6). The second one is the HP-LT blueschist to eclogitic facies
55
561027 marking subduction of the Sistan ocean beneath the Afghan Block, dated at 86 ± 3 Ma (Fotoohi
57
581028 Rad et al., 2005,2009; Angiboust et al., 2013; Bröcker et al., 2013; Kurzawa et al., 2017; Bonnet
59
60
61
62
63
64
65

1029 et al., 2018). The third one is marked by lawsonite-bearing metasediments and metamorphic
1
21030 soles found at the base of the Neh ophiolite, which advocate for intra-oceanic slicing/subduction
3
41031 starting between 74 and 72 Ma. This intra-oceanic thrusting would account for the later
5
6
71032 obduction of the Neh ophiolite onto the Lut Block. Last, metasediments recording contact
8
91033 metamorphism, which are located in the vicinity of the granitoids intruding both the Lut block
10
11
121034 and the southermost exposures of the Neh ophiolitic complex, are inferred to be dated at ~50
13
141035 Ma. Some of these rocks may testify to metamorphic conditions marking incipient collision in
15
16
171036 the Sistan orogen.

18 191037 20 21 221038 10.3. Tectonic evolution of the northern Sistan orogen and regional implications

23
241039 Based on the synthetic cross-section of the northern Sistan orogen and the tectono-
25
261040 metamorphic events documented here (Figs. 3, 16, 17), the following section, together with
27
28
291041 Figure 18, propose a tentative reconstruction of the main geodynamic stages of the Sistan
30
311042 orogeny, from the rifting stage to the present.

32 33 341043 10.3.1. Rifting and slow-spreading ocean basin (Cretaceous)

35
361044 The oldest evidence in support of an oceanic domain between the Lut and Afghan Blocks
37
38
391045 was provided by K-Ar dating of amphibole from a gabbroic intrusion at 124 Ma (Delaloye and
40
411046 Desmons, 1980), in agreement with the Early Aptian biostratigraphic ages of radiolarian chert
42
43
441047 interlayered with basalts in the ophiolitic sequence (~120 Ma; Western Unit, Sulabest area:
45
461048 Babazadeh and De Wever, 2004). Other age constraints obtained by biostratigraphy (of
47
48
491049 radiolarites: Ozsvárt et al., 2020), U-Pb zircon dating of leucogabbro (Zarrinkoub et al., 2012a)
50
511050 or $^{40}\text{Ar}/^{39}\text{Ar}$ step heating of amphibole from gabbro (Figs. 13a) give a consistent (minimum)
52
531051 Albian age between 113 and 106 Ma for the ophiolite. This indicates that the rifting stage must
54
55
561052 predate the Early Aptian. As a result, the Barremian to Aptian Orbitolina limestone (Maurizot
57
581053 et al., 1990) found on both the Lut and Afghan Blocks could be broadly contemporaneous with
59
60
61
62
63
64
65

1054 the rifting of the Sistan ocean. Sediments found in the footwall of normal faults on the Afghan
1
21055 Block are nevertheless somewhat older, possibly pointing to an even earlier extension/rifting
3
4
51056 stage.

6
71057 Geochemical investigations of the Sistan ophiolite show that the crustal section of the
8
9
101058 ophiolite, whenever present, essentially comprises N-MORB basalts and gabbros. Associated
11
121059 depleted harzburgite is interpreted as residual mantle, following melting. However, depending
13
14
151060 on the proxy used (i.e., #Cr in spinel, Ti in clinopyroxene or trace element modelling),
16
171061 contrasting degrees of partial melting were proposed to produce these N-MORB and/or the
18
191062 residual depleted harzburgite, from low (Zarrinkoub et al., 2012a) to high (Moazzen et al.,
20
21
221063 2006) and in one or several melting stages (Saccani et al., 2010). Some E-MORB were
23
241064 interpreted as coming from an interaction between the DMM and an enriched deeper source
25
26
271065 (Saccani et al., 2010; Zarrinkoub et al., 2012a), whereas rare, supra-subduction zone affinity
28
291066 magmatic rocks were interpreted as produced by a DMM source fluxed by subduction-derived
30
31
321067 fluids (Saccani et al., 2010; Zarrinkoub et al., 2012a). Our structural observations on the
33
341068 ophiolitic sequence show that the Sistan ophiolite exhibits all the characteristics of a fossil slow-
35
361069 spreading ocean, implying that the last partial melting stage was low (e.g.: Cannat et al., 2009;
37
38
391070 Lagabrielle et al., 2015; Eddy et al., 2017; Escartín et al., 2017), and that some of the early
40
411071 oceanic detachments are probably partly preserved (Fig. 18a).

42 43 441072 10.3.2. Subduction beneath the Afghan margin (~90-55 Ma?)

45
461073 Initiation of E- to NE-dipping subduction of the Sistan ocean below the Afghan Block is
47
48
491074 difficult to date and locate precisely, but several markers support its existence from at least 90
50
511075 Ma (Turonian, Fig. 18a), and possibly before: (1) Peak burial of the blueschist and eclogite
52
53
541076 facies units of the Ratuk complex was dated at 86 ± 3 Ma by several methods (Bröcker et al.,
55
561077 2013; Kurzawa et al., 2017; Bonnet et al., 2018); (2) The flexural flysch basin, whose
57
581078 depocenter lies on the Afghan block, expands during the Senonian (Coniacian to Maastrichtian:
59
60
61
62
63
64
65

1079 90-72 Ma; Tirrul et al., 1983; Maurizot et al., 1990a; 1990b); (3) Typical juvenile arc magmatic
1
21080 rocks and/or high silica adakites are intrusive or interbedded into the Sefidabeh flysch basin,
3
4
51081 the Western Unit and the HP-LT units. U-Pb dating on zircon gave ages between c.a. 86 and
6
71082 71 Ma for this magmatism (Zarrinkoub et al., 2012b; Jentzer et al., 2020). (4) The main thrusts
8
9
101083 indicate W/SW-vergent deformation. Unlike the HP-LT suture zone located between the Neh
11
121084 complex and the Afghan Block, no suture zone exists between the Neh complex and the Lut
13
141085 Block, making the hypothesis of a west-dipping subduction zone below the Lut Block (e.g.,
15
16
171086 Pang et al. 2012) difficult.

18
191087 After the formation of cold ($7^{\circ}\text{C km}^{-1}$) eclogites, the formation of high silica adakites
20
21
221088 (requiring partial melting of the downgoing slab crust) reflects a change in the thermal regime
23
241089 of the subduction and points to a likely slab breakoff event at ~80 Ma (see discussion in Jentzer
25
261090 et al., 2020 ; Fig. 18b). Incidentally, the presence of high silica adakite dykes and sills intruding
27
28
291091 the Western Unit implies that this unit belonged to the upper plate of the subduction system.
30
31
321092 Since the Western Unit comprises non-metamorphosed ophiolitic rocks (i.e., serpentinized
33
341093 peridotite, gabbroic intrusions and basalts), it could either represent a portion of the Sistan ocean
35
361094 or a piece of forearc and/or ocean-continent transitional domain connected to the Afghan
37
38
391095 margin.

40
411096 Assuming that the Sistan ocean opened at ~125 Ma and subduction started below the
42
43
441097 Afghan Block at 90 Ma, the slow-opening Sistan ocean ($<\sim 2\text{cm.y}^{-1}$) was probably not wider
45
461098 than ~700 km.

47 48 491099 10.3.3. Intra-oceanic subduction and obduction of the Neh complex (~73 Ma)

50
511100 Two types of metamorphic rocks provide evidence for a specific deformation event
52
53
541101 affecting the Sistan ocean during the Upper Campanian: (1) The strongly schistosed, 10-20 m
55
561102 thick horizons of amphibolite facies metabasic and metasedimentary rocks underlying the
57
581103 ophiolite, best exposed in the south of the study area and near Sarbisheh (Figs. 4), with an
59
60
61
62
63
64
65

1104 inferred metamorphic age around 72 Ma (Figs. 15). Their structural characteristics and
1
21105 metamorphic peak, around $700^{\circ}\text{C} \pm 50$ and 0.6-0.7 GPa (Figs. 14), suggest that they represent
3
4
51106 a metamorphic sole and therefore mark the initiation of intra-oceanic subduction (e.g.,
6
71107 Wakabayashi and Dilek, 2003; Agard et al., 2016; Plunder et al., 2016; Guilmette et al., 2018;
8
9
101108 Dubacq et al., 2019); (2) The lawsonite-bearing metasediments located at the base of the
11
121109 ophiolitic Unit 2 (Figs. 7 and 11g), south of Birjand, with a coincident metamorphic age
13
14
151110 between 74 and 72 Ma, which indicate a synchronous intra-oceanic thrusting, though possibly
16
171111 of a lesser extent (i.e., with pressure of 0.4 GPa advocating for only ~15 km of burial). These
18
191112 tectono-metamorphic events are interpreted here to reflect initiation of intra-oceanic thrusting
20
21
221113 and/or subduction at 73 ± 1 Ma, whose amplitude was larger in the eastern part of the study area
23
241114 (metamorphic soles; Sarbisheh, Malabad) than in the western part (lawsonite-bearing samples;
25
26
271115 Birjand ridge). This event is coeval with large-scale plate reorganization further east, with
28
291116 Indian starting its northward migration and obduction of ophiolites east of the Afghan block
30
31
321117 (i.e., Bela and Muslim Bagh ophiolites, Gnos et al., 1997).

33
341118 In order to account for the emplacement of the obducted Neh complex onto the Lut
35
361119 Block, this intra-oceanic subduction must have been dipping to the NE (in present-day
37
38
391120 coordinates, i.e. without correcting for the $\sim 30^{\circ}$ Cenozoic rotation; Mattei et al., 2015; Figs.
40
411121 18c,d, 19). Further evidence may come from the existence of supra-subduction ophiolitic
42
43
441122 material reported in the south of the study area (near Barak; Saccani et al., 2010), but age
45
461123 constraints are lacking for now. Likewise, the ~ 71 Ma intrusive adakitic magmatism described
47
48
491124 in the Neh complex (Zarrinkoub et al., 2012b) could support intra-oceanic subduction, during
50
511125 which small volumes of adakitic melts can be produced by partial melting of the downgoing
52
531126 slab crust ($< 5\text{-}10\%$ vol at 850°C ; Agard et al., 2016).

54
55
561127 At the same in the eastern part of the orogen, the HP-LT metamorphic units are already
57
581128 exposed as shown by the presence of unconformable Maastrichtian deposits (Bonnet et al.,
59
60
61
62
63
64
65

1129 2018). The HP-LT units were exhumed along the suture, and now exposed into the thinned
1
21130 Afghan margin, at 4 mm yr⁻¹ on average. Lower Maastrichtian sedimentation in the innermost
3
4
51131 part of the orogen is characterized by a drastic regression (from deep Senonian flysch to
6
71132 Maastrichtian conglomerate and reefal limestone; section 5) leading to the individualization of
8
9
101133 distinct sedimentary basins, i.e. the Sefibadeh basin with shallower deposits than the finely
11
121134 laminated turbidites of the Neh basin (Tirrul et al., 1983).

14
151135 These important changes could relate to the slowdown of the main NE-dipping subduction,
16
171136 as a result of the suspected ~80 Ma slab breakoff (Jentzer et al., 2020), and/or to some large-
18
191137 scale reorganization of regional geodynamics

221138 10.3.4. End of obduction and onset of collision between the Lut and Afghan 23 241139 Blocks (~55-50 Ma)

26
271140 After the beginning of intra-oceanic subduction at 74-72 Ma, another change occurs during
28
291141 the Eocene (Fig. 18e), marked by: (1) The change from Upper Paleocene flysch-dominated
30
311142 sediments to Eocene coarse grain continental conglomerates and molasse-type sediments (i.e.,
32
33
341143 'red beds'). In the SW part of the Neh complex, Eocene deposits are still fine grained with thin
35
361144 argillite layers, indicating a deeper environment than for the conglomerate deposits and
37
38
391145 suggesting southwestward migration of depocenters with time; (2) A deformation event is
40
411146 revealed by the unconformity of the Eocene deposits onto Paleocene sediments. Tirrul et al.
42
43
441147 (1983) recognized two stages of deformation of the Eocene deposits, whereas the Oligocene
45
461148 conglomerates are much less deformed; (3) Obduction movements, i.e. the respective
47
48
491149 movements of the Lut Block and Neh complex, have largely ended by then (Fig. 18e) since a
50
511150 weakly deformed granitoid intrusion dated at 49.6 ± 0.2 Ma cuts through both units (Fig. 15l).

531151 The change in sedimentary regime and the unconformity between the Paleocene and
54
55
561152 Eocene deposits suggest that the collision began during the Eocene, between ~55 Ma and 50
57
581153 Ma (according to current biostratigraphic knowledge). Syn-kinematic emplacement of
59
60
61
62
63
64
65

1154 granitoids cutting through the obduction nappe thrust could be associated with the first
1
21155 collisional movements.

4 51156 10.3.5. Events following the onset of collision (after ~45 Ma)

6
71157 A large calc-alkaline (to alkaline) magmatic production develops from the Mid-Eocene
8
9
101158 onwards (46-25 Ma; Fig. 18f, g). Two stages were identified (Camp and Griffis, 1982; Pang et
11
121159 al., 2013; Mohammadi et al. 2016): the older one (46-40 Ma; Lutetian) reflects mixed
13
141160 contributions from mantle and upper crustal sources. Partial melting of the upper crust was
15
16
171161 tentatively associated with the onset of lithospheric delamination; the younger one <30 Ma
18
191162 (Rupelian) has a dominant mantle source and was interpreted as resulting from complete
20
21
221163 delamination and formation of a wide asthenospheric window.

23
241164 Shortening of the Sistan orogen prevailed during the first period (i.e. possible inception of
25
26
271165 delamination), as evidenced by the unconformity between the Oligocene and the Eocene
28
291166 deposits. In contrast, only minor shortening is observed after the beginning of the Oligocene
30
31
321167 (~30 Ma; Tirrul et al., 1983). Neogene conglomerates unconformably overlying older deposits
33
341168 indicate weak folding and faulting and reworking of earlier contacts (Walker and Khatib, 2006;
35
361169 Jentzer et al., 2017).

37
38
391170 Tectono-magmatic events resumed from the Mid-Late Miocene onwards, as shown by
40
411171 alkaline magmatism along major strike-slip faults (marking asthenospheric upwelling along
42
43
441172 major lithospheric discontinuities; e.g., Pang et al., 2012). Three groups of active faults were
45
461173 recognized: (1) N-S to NNE–SSW dextral strike-slip faults, which accommodated up to 95 km
47
48
491174 of motion; (2) ENE-WSW sinistral conjugate faults and (3) NW–SE trending thrust faults.
50
511175 Walker et al. (2004) proposed that these faults initiated at 7-5 Ma (during the Messinian).

52
531176 The dextral strike-slip faults likely accommodated the counterclockwise rotation of at least
54
55
561177 35° which affected the Central Iranian microcontinent, including the Lut block, since the Mid-
57
581178 Late Miocene (Mattei et al., 2015). These deformations likely relate to the increase in the
59
60
61
62
63
64
65

1179 intensity of the Arabia-Eurasia collision since 15-10 Ma (Ballato et al., 2011), as shown by the
1
21180 progressive alignment of the main horizontal stress component across Iran and in the northern
3
41181 Sistan (Jentzer et al., 2017).
5
6

71182 10.4. Tectonic significance of the Sistan orogen within the Neotethyan realm 8

91183 10.4.1. The Sistan ophiolite vs the other ophiolites of the 'Inner ophiolite belt' 10

11
121184 The Sistan ophiolite is one amongst the many ophiolite belts preserved, across the Iranian
13
141185 territory, between the Neotethys and Paleotethys suture zones (Fig. 1b; Stöcklin, 1968;
15
161186 Moghadam and Stern, 2015). These Mesozoic ophiolitic domains (Table 2 and references
17
181187 therein) have commonly been interpreted as marginal basins opened within the upper plate of
19
201188 the Neotethys subduction system, mostly during the Cretaceous (Agard et al., 2011), although
21
221189 their exact tectonic evolution and mutual relationships remain obscure. These (partly
23
241190 independent?) basins likely developed along inherited boundaries separating the Cimmerian
25
261191 Blocks.
27
28
29
30

311192 The Sistan ophiolite is the most extensive, along with the Makran ophiolites (i.e., Band e
32
331193 Zeyarat, Fanuj-Makutan). Despite large uncertainties on the timing of their initiation, these
34
351194 ophiolitic basins can be collectively regarded as having lasted between ~140-120 and ~70-55
36
371195 Ma and were already closed by the Paleocene to Eocene (Table 2). A slightly diachronous
38
391196 opening of these basins is suspected, for example (i) to the north, in the Sabzevar domain (Late
40
411197 Jurassic?; Lindenberg and Groler, 1984; Omrani, 2017; Stöcklin, 1974), possibly coeval with
42
431198 the Waras Panjaw ocean in Afghanistan or the Caspian sea, or (ii) to the south in the Nain-
44
451199 Deshir-Baft-Bad e Zeyarat, Fanuj-Maskutan (145 Ma or older?; Saccani et al., 2018; Hunziker
46
471200 et al., 2015; Ghazi et al., 2004; Ghazi et al., 2012; Moghadam and Stern, 2015, Pirnia et al.,
48
491201 2020), but ages are still somewhat contradictory.
50
51
52
53
54

551202 The Sistan differs in several ways: it is the only one exposing subduction-related cold HP-
56
571203 LT metamorphic rocks and arc magmatic rocks, km-scale unmetamorphosed slices of ophiolite
58
59
60
61
62
63
64
65

1204 from a former slow spreading ocean and rather extensive metamorphic soles. These specificities
1
21205 can be questioned: was the Sistan ocean initially larger or is it better preserved because of its
3
41206 orientation or because of different obduction processes (i.e., with respect to mechanisms and/or
5
6
71207 intensity)?
8

9
101208 Contrary to the many ophiolites worldwide (Agard et al., 2016, 2020), most commonly
11
121209 formed in a supra-subduction zone environment (Dilek and Furnes, 2019), and to several other
13
141210 Neotethyan ophiolites (Semail, Nain-Baft), the metamorphic soles of Sistan only exhibit
15
16
171211 intermediate (MP-MT) conditions and in particular no granulite facies HT soles (Soret et al.,
18
191212 2017). The Sistan ophiolite is also different in that it is mainly N- to E-MORB-type, it is older
20
21
221213 than the metamorphic sole, no HP-LT metamorphism is observed in the underthrust continental
23
241214 margin and no significant extension postdates ophiolite emplacement (contrary to the Semail
25
26
271215 ophiolite; Fournier et al., 2006; Hansmann et al., 2017; Ninkabou et al., 2021). Similar
28
291216 characteristics are found for the Sevan ophiolite (Hässig et al, 2015; Rolland et al., 2019).
30

31
321217 A tentative explanation could be that the ~73 Ma intra-oceanic subduction within the Sistan
33
341218 ocean reached shallower depths than in the main Neotethys ocean, thereby never leading to the
35
361219 formation of a supra-subduction ophiolite like the Semail ophiolite. This could relate to the slow
37
38
391220 spreading character of the Sistan ophiolite, with a thick and weak serpentized zone at its base
40
411221 hampering the formation of HT metamorphic soles and promoting strain localization at
42
43
441222 shallower depths compared to other large-scale ophiolites (hence without proper slabitization:
45
461223 Agard et al., 2020).
47

48 491224 10.4.2. Sistan orogeny within the Neotethyan realm

50
511225 A qualitative paleotectonic reconstruction, with the aim to set back the tectonic evolution
52
531226 of the Sistan orogen with the larger Neotethyan realm and address uncertainties on the initial
54
55
561227 orientation of the Sistan ocean (see section 2), is proposed in Figure 20. It places emphasis on:
57
58
59
60
61
62
63
64
65

1228 (i) the opening of the Sistan basin around 125 Ma (Fig. 20b) and inception of the main
1
21229 Sistan subduction zone below the Afghan Block around 100-90 Ma, following the regional-
3
4
51230 scale plate reorganization (Agard et al 2006; Matthews et al., 2012) marked by other obduction
6
71231 events in the Neotethys (e.g., Turkey, Armenia, ~104-88 Ma; Zagros: Neyriz, 95 Ma; Lanphere
8
9
101232 and Pamic, 1983; Pourteau et al., 2018; Oman, between 104 and 95 Ma; Rioux et al., 2016;
11
121233 Guilmette et al., 2018; Burg, 2018 and references therein; Fig. 20c) and widespread blueschist
13
14
151234 exhumation (Monié and Agard, 2009; Angiboust et al., 2016). This age also corresponds to the
16
171235 beginning of the transform motion between India and Africa (Rodriguez et al., 2020 and
18
191236 references therein).

21
221237 (iii) the initiation of intra-oceanic subduction within the Sistan oceanic domain at ~73 Ma,
23
241238 ultimately leading to the emplacement of the ophiolitic Neh complex onto the Lut Block. This
25
26
271239 period coincides with a second major reorganization of the eastern Neotethys and Indian ocean
28
291240 (Gaina et al., 2015), marked by the onset of fast convergence of the Indian continent towards
30
31
321241 Eurasia and obduction of the Masirah, Ra's Madehah, Bela, Muslim Bagh or Spontang
33
341242 ophiolites between 70 and 65 Ma (Gnos et al., 1997; Corfield et al., 2001; Figs. 20d).

361243 During the mid-Jurassic, following Paleotethys closure and inception of Neotethys
37
38
391244 subduction, a magmatic arc starts forming at ~175 Ma along the Sanandaj-Sirjan and Bajgan-
40
411245 Durkan domains (Fig. 20a; e.g. Stampfli and Borel, 2002; Agard et al., 2011; Seton et al., 2012;
42
43
441246 Burg, 2018). Fragmentation of the upper plate starts in the Mid-Jurassic to the east of the future
45
461247 Sistan domain, with the opening of the back-arc Waras-Panjaw basin separating the Band-e
47
48
491248 Bayan and Helmand Blocks (Fig. 20a). A similar yet slightly younger (Mid to Late Jurassic)
50
511249 evolution affects the Iranian region, as shown by the opening of the south Caspian basin,
52
53
541250 possibly extending eastward to Sabzevar and Torbat-e-Heydarieh, and extensional movements
55
561251 in the Kopeh-Dagh (Stöcklin, 1974; Brunet et al., 2003; Robert et al., 2014; Omrani, 2017). To
57
581252 the south of the CEIM, the magmatic evolution advocates for back-arc extension at the rear of
59
60
61
62
63
64
65

1253 the Neotethyan subduction zone, in the future Makran region (Hunziker et al., 2015; Burg,
1
21254 2018), in the Kandahar basin (Siehl, 2017) and possibly along the Sanandaj-Sirjan zone (Azizi
3
41255 and Stern, 2019).

6
71256 During the Early Cretaceous (Fig. 20b), extensional movements lead to rifting and to the
8
91257 formation of the Fannuj ocean between the CEIM et Bajgan-Durkan (e.g. Pirnia, 2020; Sepidbar
10
11
121258 et al., 2020), extending to the northwest in the future Nain-Baft domain up to the Dorouneh-
13
141259 Grat Kavir fault, suspected to have been active at the time (e.g. Mattei et al., 2015). In contrast,
15
16
171260 on the Afghan side, the Waras-Panjaw ocean is progressively closing (Montenat, 2009).
18
191261 Opening of the Sistan basin in an oblique transtensional (pull-apart) setting, as shown in Figure
20
21
221262 20b, would explain the contrasting evolution between the Lut and Afghan transects, as well as
23
241263 its peculiar N-S orientation. Similar settings were proposed for the oceanic domain where the
25
261264 future Pakistani Bela and Muslim Bagh ophiolites formed along the Chaman fault or for the
27
28
291265 north-Somalia basin (Gaina et al., 2015), or in the Caiman sea (Leroy et al., 2000). This
30
311266 geometry would be consistent with the existence of a STEP fault (Govers and Wortel, 2005)
32
33
341267 separating the sinking Neotethyan slab across the present-day Neh fault.

35
361268 Between 115 and 85 Ma, the Arabia-Eurasia convergence rate steadily increases and
37
38
391269 changes orientation (Fig. 20c; e.g. Agard et al., 2006; DeMets et al., 2010), leading to a major
40
411270 reorganization in the Neotethys, with initiation of intraoceanic subduction zones at 105-95 Ma,
42
43
441271 leading to the formation and emplacement of several ophiolites and intraoceanic arcs (e.g.
45
461272 Guilmette et al., 2018; Pourteau et al., 2018; Bonnet et al., 2020). We relate these kinematic
47
48
491273 changes to the onset of closure of the Iranian marginal basins: to the north, the metamorphic
50
511274 evolution in the Sabzevar domain (through the presence of granulites similar to metamorphic
52
531275 soles; Rossetti et al., 2010) likely advocates for the onset of subduction, and the Waras-Panjaw
54
55
561276 ocean is closed (Montenat, 2009; Siehl, 2017). In the Nain-Baft domain, metamorphic soles
57
581277 marking closure were dated at 100-90 Ma (Shafai Moghadam et al., 2009). In the south, in the
59
60
61
62
63
64
65

1278 Makran region, arc magmatism is still active and blueschists are exhumed at 100-95 Ma (Burg,
1
21279 2018), as along the southern Sanandaj-Sirjan zone (Agard et al., 2006; Angiboust et al., 2016).
3
4
51280 In the Sistan region, peak burial of blueschists and eclogites at ~86 Ma (Bröcker et al., 2013;
6
71281 Bonnet et al., 2018) indicates that subduction has been active since a few millions years at least.
8
9
101282 During the Campanian (~75 Ma; Figs. 20d), most of the Iranian marginal basins are
11
121283 actively closing. The Sistan ocean records the onset of intraoceanic shortening at ~73 Ma,
13
141284 contemporaneous with the northward migration of India, changes in subduction dynamics and
15
16
171285 obduction movements marked by the emplacement of the Masirah, Muslim Bagh, Bela and
18
191286 Spontang ophiolites (Gnos et al., 1997; Corfield et al., 2001; Gaina et al., 2015). The Sistan
20
21
221287 ocean, probably due to its central location in the Neotethyan realm, appears to have strikingly
23
241288 recorded the major plate reorganizations at 100-90 Ma and 75-70 Ma which triggered the main
25
26
271289 obduction events of the Neotethys (Gnos et al., 1997; Agard et al., 2007; Gaina et al., 2015).
28
291290 To the east of the Sistan domain, magmatic arcs form in the southern Afghan Block (Chagai
30
311291 Hills; Ras Koh, where small ophiolitic remnants are also found). Whether these represent
32
33
341292 accreted forearcs or formed within a lateral equivalent of the microcontinental Kabul Block is
35
361293 unknown (Siehl, 2017; Burg, 2018). Maastrichtian sediments unconformably overlying the Ras
37
38
391294 Koh, Makran, Baft and Deshir ophiolites indicate that these were obducted by then (later
40
411295 Paleocene sediments in the Nain ophiolite may indicate diachronous closure, younging towards
42
43
441296 the NW).

45
461297 During the Lower Eocene, obduction of the Sistan and Sabzevar ophiolites is over, all
47
48
491298 Iranian marginal basins are closed except the south Caspian basin. From the Eocene
50
511299 onwards, calc-alkaline magmatism affects most of Iran, along the Urumieh–Dokhtar arc, from
52
531300 the Alborz to Kopeh Dagh, and in the Lut Block west of Sistan (Fig. 20e). This episode reflects
54
55
561301 large-scale distributed extension triggered by lithospheric delamination and/or Neotethyan slab
57
581302 retreat (Omrani et al., 2008; Agard et al., 2011; Verdel et al., 2011; Rossetti et al., 2014).
59
60
61
62
63
64
65

1303 **11. Conclusions**

1
2
3
4
5
6
7
8
9
10
11
12
13
14
15
16
17
18
19
20
21
22
23
24
25
26
27
28
29
30
31
32
33
34
35
36
37
38
39
40
41
42
43
44
45
46
47
48
49
50
51
52
53
54
55
56
57
58
59
60
61
62
63
64
65

(1) This study provides new insights on the units and structural organization of the Sistan orogenic belt. The Afghan Block and Western Unit occupy the highest structural position, through which the HP-LT suture zone is exposed as a tectonic window, while the Neh complex is represented by a continuous, weakly deformed ophiolite thrust to the SW over the Lut Block. Sediments of the Neh complex evidence a progressive southwestward migration of depocenters and burial (up to ~275°C on average) in a warm thermal gradient (50°C.km⁻¹). Major thrusts within the Neh complex dip to the NE and post-emplacement shortening is relatively modest (30-50 km). The ophiolitic part of the Neh complex, which attests to a former slow- to ultra-slow spreading ocean with extensive hydrothermal alteration, exposes in its basal part a 74-72 Ma metamorphic sole. Ophiolite emplacement was largely achieved by 55-50 Ma when granitoids intruded both the ophiolite and the Lut Block. Two types of metamorphism are observed in the Lut Block: contact metamorphism (andalusite/sillimanite- and biotite-bearing micashists) related to the ~55-50 Ma granitoid intrusions, possibly lightly imprinted by later collision; regional metamorphism, marked by the presence of micashists and migmatites, dated at ca. 150 Ma and probably associated with the Mid- to Late Cimmerian events which affected Central Iran.

(2) Based on the tectono-metamorphic data and events documented here and literature data, a tentative reconstruction of the geodynamic evolution of the Sistan orogen is proposed: (i) between 124 and 90 Ma, and possibly earlier, the slow- to ultra-slow spreading Sistan ocean was active, suggesting a maximum width of ~700 km; (ii) since 90 Ma at least, NE-dipping subduction of the Sistan ocean below the Afghan margin was active: this was responsible for the flexural subsidence a deposition of the Senonian flyschs, the formation and exhumation of blueschists and eclogites and the emplacement of calc-alkaline and adakitic arc magmatism; (iii) between 74 and 72 Ma, an intra-oceanic NE-dipping thrusting or subduction was initiated,

1328 as attested by metamorphic sole rocks, which ultimately led to the obduction of the Neh
1
21329 complex ophiolitic domain onto the Lut Block, largely completed by 55-50 Ma; (v) Eocene
3
4
51330 collision, marked by a drastic change in sedimentation, was only moderate, with around 30-40
6
71331 km of shortening, and rather short-lived, being mostly achieved during the Oligocene. Later,
8
9
101332 post-collisional shortening was limited (probably ~10-20 km).

121333 (3) In a Neo-Tethyan perspective, the comparison between the tectonic evolution of Sistan
13
14
151334 and those of the other Inner ophiolite belts of Central Iran suggests that: (i) the Sistan ocean
16
171335 formed as an independent pull-apart basin along an inherited transfer fault located between Iran
18
191336 and Afghanistan, as a result of transtensional movements and contrasting slab dynamics along
20
21
221337 the Neo-Tethyan subduction zone; (ii) the triggering of the ~90 Ma main subduction zone
23
241338 coincides with a major kinematic change (in both velocity and direction) within the Neo-
25
26
271339 Tethyan realm, coeval with the exhumation of Zagros and Makran blueschists and the obduction
28
291340 of the Western Tethyan ophiolites (e.g. Oman, Turkey); (iii) initiation of the 74-72 Ma intra-
30
31
321341 oceanic thrusting/subduction coincides with the obduction of the Eastern Tethyan ophiolites
33
341342 (e.g. Bela, Muslim Bagh, Spontang) and the closure of most of the Inner Iranian ophiolitic
35
36
371343 basins. The Sistan orogen, with its central position in the Tethyan realm, therefore appears to
38
391344 have recorded all the main tectonic stages accompanying Neo-Tethyan closure.

411345 42 431346 **Acknowledgements**

45
461347 We feel indebted to the Geological Survey of Iran, and especially to Dr. Shahidi, to the
47
481348 geologists and all the staff (drivers, cooks and chief of camp) for their kindness, constant
49
50
511349 support and for enabling us to visit the region since 2014. This work was financially supported
52
531350 by the CNRS-INSU programs, by IStEP lab of Sorbonne University and by the over-head of
54
55
561351 the project “Zooming in Between Plates” (Marie Curie International Training Network of the
57
581352 European Union’s Seventh Framework Program FP7/2007/2013/ under REA grant agreement

1353 no. 604713). We would like to warmly thank M. Eric Delairis who produced the thin sections
1
21354 studied; M. Omar Boudouma for its help during SEM sessions; M. Michael Fialin and M.
3
41355 Nicolas Rividi for their technical support during microprobe analyses. Main thanks to M. Eric
5
6
71356 Barrier for taking the time to discuss tectonic reconstructions.
8

9 101357 11 121358 **Appendix: Methods used**

13 14 15 161359 1. Analytical methods used

17 181360 1.1. Mineral chemistry

19
20
211361 The electron microprobes used for this study were Cameca SX-5 and SX-100 at Camparis
22
231362 (Sorbonne Université, 4 place Jussieu, 75005 Paris, France). Point measurements were made in
24
251363 classical analytical conditions (15 kV acceleration voltage and 10 nA beamcurrent allowing ~2
26
27
281364 μm beam size in wavelength-dispersive spectroscopy mode) using diopside (Ca,Mg, Si),
29
301365 MnTiO_3 (Mn, Ti), orthoclase (K, Al), Fe_2O_3 (Fe), albite (Na) and Cr_2O_3 (Cr) as standards for
31
32
331366 calibration of elements indicated in parentheses. Elemental mapping has been carried out with
34
351367 identical voltage and an increased current (100 nA) with a counting time of 100 ms per point.
36
37
381368 Analyses were calibrated with the manufacturer's software using standards as point analyses
39
401369 (Pouchou and Pichoir, 1991). All analysis were sorted based on their structural formulae
41
42
431370 calculated with Fe^{3+} estimates using the method of Droop (1987) for garnet and clinopyroxene,
44
451371 and the method exposed in Leake et al. (1997) for amphibole. We considered all iron as ferric
46
471372 in epidote and lawsonite, and as ferrous in mica.

49 501373 1.2. RAMAN spectroscopy and mineral determination

51
521374 RAMAN spectroscopy on polished thin sections was used to identify the serpentine and
53
54
551375 the carbonate minerals. Following Schwartz et al, (2013), the spectral regions investigated to
56
571376 characterize serpentine species are from 150 to 1150 cm^{-1} and from 3600 to 3720 cm^{-1} because
58
59
601377 they include the lattice vibrational modes and the OH stretching mode region. The nature of
61
62
63
64
65

1378 carbonate material was determined using the spectral region between 600 to 800 cm^{-1} as
1
21379 indicated in Kontoyannis and Vagenas (2000).
3

4 51380 2. Thermometric methods used 6

71381 2.1. Raman spectroscopy on carbonaceous material: T_{max} estimation 8

9
101382 The Raman spectrum of carbonaceous materials (RSCM) between 1100 and 1800 cm^{-1} can
11
121383 exhibit a characteristic graphitic band at $\sim 1580 \text{ cm}^{-1}$ and four defect bands at ~ 1200 (D4), ~ 1350
13
141384 (D1), ~ 1500 (D3) and ~ 1620 (D2) cm^{-1} . The increase of temperature during diagenesis and
15
161385 metamorphism induces a progressive and irreversible loss of the defect bands, thus for a
17
181386 temperature $>655^\circ\text{C}$, all the organic matter is changed into pure graphite. Nowadays, several
19
201387 calibrated methods using Raman spectra allow to quantify the maximum temperature (T_m)
21
221388 reached by the carbonaceous materials (CM) between 150°C and 655°C with an intrinsic error
23
241389 of $\pm 50^\circ\text{C}$ (Beysac et al., 2002; Lahfid et al., 2010; Kouketsu et al., 2014). In this study, we
25
261390 used for $T_m \geq 330^\circ\text{C}$ the calibration from Beysac et al. (2002) and the calibration from Lahfid
27
281391 et al. (2010) for $T_m < 330^\circ\text{C}$.
29
30
31
32

33
341392 Raman spectra were collected with a Raman microspectrometer (Renishaw inVia located
35
361393 at the ENS and at the IMPMC, both in Paris, France) on conventional petrographic thin sections.
37
381394 Textural position of the CM was carefully checked and the focus was made beneath the surface
39
401395 of a transparent adjacent grain to limit some potential parasitic effects. Analysis was performed
41
421396 in the center of the carbonaceous particles, using argon laser beam (514 nm, Spectra Physics)
43
441397 equipped with a LEICA 50 x magnification objective (0.5 numerical aperture) and using a
45
461398 circular polarization of the laser. The Raman scattered light was dispersed by wavelength using
47
481399 a holographic grating with 1800 lines/mm and detected by a CCD camera. The spectra were
49
50
511400 recorded in the 700 to 2000 cm^{-1} range (first order spectrum). For each sample between 11 and
52
53
541401 20 coherent Raman spectra were obtained.
55
56
57

581402 2.2. Ti in biotite: empirical thermometry 59 60 61 62 63 64 65

1403 For metapelitic rocks saturated in Al, in Ti, and in Si (aluminosilicate, rutile or ilmenite
 1404 and quartz bearing rock) and for biotite with $X_{Mg} \geq 0.275$ and $0.04 < Ti < 0.6$ apfu, the
 1405 incorporation of Ti in octahedral sites of biotite depends on temperature. Henry (2005) proposed
 1406 an empirical function linking Ti in biotite and temperature as defined in equation (A) with an
 1407 uncertainty of $\pm 24^\circ\text{C}$. This relationship can be used between 0.3 and 0.6 GPa and 480 to 800°C .
 1408 Presence of CM in the rock is recommended to use this geothermometer because CM buffers
 1409 the oxygen and limits the formation of Fe^{3+} .

$$(A) \quad T = \left(\frac{\ln(Ti) - a - c(X_{Mg})^3}{b} \right)^{0.333}$$

1411 Where T is temperature in $^\circ\text{C}$, Ti is the Ti content of the analysed biotite in apfu, X_{Mg} of
 1412 the analysed biotite and a, b and c three adjustment coefficients respectively defined as:

$$a = -2.3594, \quad b = 4.6482 \cdot 10^{-9} \quad \text{and} \quad c = -1.7283.$$

3. Thermobarometric methods used

3.1. Plagioclase-amphibole

1417 Holland and Blundy (1994) proposed an edenite-richterite thermometer (edenite + albite =
 1418 richterite + anorthite), based on the exchange (Na Si)-(Ca Al) between amphibole and
 1419 plagioclase as described in the equation B. This method can be used over a broad range of bulk
 1420 rocks composition (with or without quartz), in a range of 400 to 1000°C and 0.1 to 1.5 GPa
 1421 with an uncertainty around $\pm 40^\circ\text{C}$.

$$(B) \quad T = \frac{78.44 + Y_{ab-an} - 33.6 X_{Na}^{M4} - (66.8 - 2.92P) X_{Al}^{M2} + 78.5 X_{Al}^{T1} + 9.4 X_{Na}^A}{0.071 - R \ln \left(\frac{27 X_{Na}^{M4} X_{Si}^{T1} X_{an}^{Pl}}{64 X_{Ca}^{M4} X_{Al}^{T1} X_{ab}^{Pl}} \right)}$$

1423 Where the Y_{ab-an} term is given by: for $X_{ab} > 0.5$ then $Y_{ab-an} = 3$ kJ otherwise $Y_{ab-an} =$
 1424 $12.0 (2X_{ab} - 1) + 3$ kJ, T is the temperature in Kelvins, P is the pressure in kbar and the $X^{\Phi i}$
 1425 terms denote the molar fraction of species (or component) i in phase (or crystallographic site)
 1426 Φ .

1427 Molina et al. (2015) proposed a barometer using the Al-Si partitioning between plagioclase
 1
 21428 and Ca-amphibole as described in equation (C). This method can be used over a broad range of
 3
 41429 bulk rocks composition (with or without quartz) but only with amphibole containing more than
 6
 71430 0.02 apfu of Ti and more than 0.05 apfu of Al_{VI}, in a range of 650 to 1050°C and 0.15 to 0.23
 8
 91431 GPa with an uncertainty $\leq \pm 0.2$ GPa.

$$(C) \quad P = \frac{8.3144 T \ln D^{pl/amph}_{Al/Si} - 8.7 T + 23337 X^{Ti}_{Al} + 7579 X_{ab} - 11302}{-274}$$

161433 Where $D^{pl/amph}_{Al/Si} = (X_{plAl}/X_{plSi})/(X_{amphAl}/X_{amphSi})$: molar plagioclase/amphibole
 17
 181434 Al-Si partition coefficient, T is the temperature in Kelvins, P is the pressure in kbar and the $X^{\Phi i}$
 19
 20
 211435 terms denote the molar fraction of species (or component) i in phase (or crystallographic site)
 22
 231436 Φ .

261437 Using both B and C equations for Ca-amphibole and plagioclase bearing metamorphic
 27
 281438 rocks, P-T conditions can be estimated between 650 and 1000°C and 0.1 to 1.5 GPa with an
 29
 30
 311439 uncertainty of $\pm 40^\circ\text{C}$ and ± 0.2 GPa.

3.2. Ti-Al amphiboles

351441 In meta-basaltic rocks saturated in Ti, Al and Ti content of Ca-amphibole can be used to
 36
 37
 381442 estimate semi-quantitatively P-T conditions (Ernst and Liu, 1998). This method has been tested
 39
 401443 for natural and experimental samples on a range of temperature between 400 and 1100°C and
 41
 42
 431444 a range of pressure between 0 and 2.2 GPa but the best fit between this method and independent
 44
 451445 P-T estimations have been obtained for low grade metamorphism. Amphibole isopleths do not
 46
 47
 481446 seem to be affected by small variations in bulk rocks composition. During cooling, the
 49
 501447 exsolution in amphibole of rutile, titanite or ilmenite which are Ti bearing phases can lead to
 51
 521448 an underestimation of the Ti content of the amphibole and must be considered.

3.3. GB and GBAQ: empirical thermobarometry

571450 Wu (2017) proposed a garnet–biotite–aluminosilicate–quartz (GBAQ) geobarometer
 58
 59
 601451 which can be used for a broad garnet and biotite composition and under P–T conditions from

1452 450 to 950°C and from 0.1 to 1.7 GPa with a random error inferred to be around ± 0.18 GPa.
1
21453 This geobarometer need to be used the type of aluminosilicate bearing in the rock and an
3
4
51454 estimated temperature which is obtained by the geothermometer garnet-biotite (GB) from
6
71455 Holdaway (2000). In this method the temperature is calculated with an estimated uncertainty of
8
9
101456 $\pm 25^\circ\text{C}$, using the Fe-Mg partition coefficient between garnet and biotite and an estimation of
11
121457 pressure. GBAQ geobarometer and GB geothermometer can be simultaneously applied to
13
141458 iteratively estimate metamorphic P–T conditions. These methods are applied only for low value
15
16
171459 of ferric iron in biotite (around 11 ± 3 mol %) which can be buffered by ilmenite and/or graphite
18
191460 in the rocks. For samples without aluminosilicate, only GB geothermometer was used.
20

21461 4. Thermodynamic modelling 22

23
241462 Pseudosections were calculated using Perple_X (6.8.6 version, Connolly, 2005, 1990).
25
26
271463 with the internally consistent thermodynamic dataset and equation of state of H₂O used come
28
291464 from Holland and Powell (2011), the useful solution models and the bulk rocks composition
30
31
321465 here obtained after crushing, dissolution and ICP-OES iCap 6 500 analysis performed in Nancy
33
341466 CRPG (results on Table 8. 4). For metabasite sample (15b-15c), the system used was Na₂O–
35
361467 CaO–K₂O–FeO–MgO–Al₂O₃–SiO₂–H₂O–TiO₂ and the solution models considered were:
37
38
391468 amphibole, augite and melt with thermodynamic properties from Green et al. (2016), garnet,
40
411469 orthopyroxene, white mica, biotite, chlorite and ilmenite with thermodynamic properties from
42
43
441470 White et al. (2014), Holland and Powell (2011) for epidote, White et al. (2002) for titanite and
45
461471 Holland and Powell (2003) for feldspar. The amount of water was chosen at 1 wt%. All the iron
47
48
491472 was considered as ferrous. For metapelitic samples (14-29a and 16-72) the system used was
50
511473 Na₂O–CaO–K₂O–FeO–MgO–MnO–Al₂O₃–SiO₂–H₂O–TiO₂ and the solution models
52
53
541474 considered were: garnet, chloritoid, staurolite, white mica, biotite, chlorite, ilmenite and melt
55
561475 with thermodynamic properties from White et al. (2014), Holland and Powell (2011) for epidote
57
581476 and Holland and Powell (2003) for feldspar. The amount of water was chosen at 2.5 wt% for
59
60
61
62
63
64
65

1477 sample 14-29a and 2 wt% for sample 16-72. All the iron was considered as ferrous. By
1
21478 minimizing Gibbs free energy, the software calculates for each desired P-T conditions the
3
4
51479 sTable 8. mineralogical assemblage and the composition of each solid solution. These models
6
71480 were compared to the natural mineral compositions obtained by microprobe analysis to estimate
8
9
101481 the P-T conditions of the mineral assemblages of our samples.

14 151483 Table 3 : Bulk rock composition used for pseudosection

16 171484 5. Geochronology methods used

18 191485 5.1. Ar-Ar

20
21
221486 Samples were carefully chosen for dating so that: they bear minerals with enough K to be
23
241487 dated with the Ar–Ar method (white mica, biotite or amphibole) and these minerals constitute
25
26
271488 a well-understood paragenesis in the rock. Selected samples were crushed and sieved; single
28
291489 grains were handpicked under binocular microscope and cleaned in ultrasonic bath with acetone
30
31
321490 and distilled water. They were packaged in Al foils and irradiated for 40 hours in the core of
33
341491 the Triga Mark II nuclear reactor of Pavia (Italia) with several aliquots of the Fish Canyon
35
361492 sanidine standard (28.03 ± 0.08 Ma; Jourdan and Renne, 2007) as flux monitor. Argon isotopic
37
38
391493 interferences on K and Ca were determined by irradiation of KF and CaF₂ pure salt. Argon
40
411494 analyses were performed at Géosciences Montpellier (France) with two analytical devices that
42
43
441495 each consist of: (a) an IR-CO₂ laser of 100 kHz used at 5–15% during 60 s, (b) a lenses system
45
461496 for beam focusing, (c) a steel chamber, kept at 10^{-8} – 10^{-9} bar, with a drilled copper plate, (d) an
47
48
491497 inlet line for purification of gases including two Zr–Al getters, (e) a multi-collector mass
50
511498 spectrometer (Argus VI from Thermo-Fisher). A custom-made software controls the laser
52
53
541499 intensity, the timing of extraction/purification and the data acquisition. To measure the Ar
55
561500 background within the system, one blank analysis was performed every three sample analyses.
57
581501 ArArCalc© v2.5.2 was used for data reduction and plotting. The one-sigma errors reported on
59
60
61
62
63
64
65

1502 plateau, isochron and total gas ages include the error on the irradiation factor J. Atmospheric
1
21503 ^{40}Ar was estimated using a value of the initial $^{40}\text{Ar}/^{36}\text{Ar}$ of 295.5.

5.2. U-Pb in titanite

71505 In situ U-Pb analyses of titanites were performed by laser ablation split-stream inductively
8
91506 coupled plasma mass spectrometry (LASS ICP-MS, Kylander-Clark et al., 2013) at the
10
111507 University of California, Santa Barbara. Samples were ablated using a Photon Machines 193
12
131508 nm ArF ultraviolet laser with a laser fluence of $\sim 1 \text{ J.cm}^{-2}$, and U-Pb isotopes and trace elements
14
151509 were analysed simultaneously on the same $35 \mu\text{m}$ spots, using a Nu Instrument Plasma 3D
16
171510 multi-collector inductively coupled plasma mass spectrometer (MC-ICP-MS) and an Agilent
18
191511 7700X quadrupole inductively coupled plasma mass spectrometer (Q-ICP-MS), respectively.
20
21
221512 The laser was fired twice at 50% power to remove surface contamination and this material was
23
241513 allowed to wash out for 15 s. Samples were then ablated at 4 Hz for 15 seconds with a laser
25
261514 energy of 1 J.cm^{-2} . Analyses of unknowns were bracketed by analyses of matrix-matched
27
28
291515 titanite standard MKED ($1518.87 \pm 0.31 \text{ Ma}$ isotope dilution thermal ionization mass
30
31
321516 spectrometry date; Spandler et al., 2016), which was used as a primary standard for U-Pb
33
341517 analyses. Secondary titanite standards BLR ($1047.1 \pm 0.4 \text{ Ma}$ concordia date; Aleinikoff et al.,
35
361518 2007), FC ($28.395 \pm 0.049 \text{ Ma}$ Concordia date; Schmitz and Bowring, 2001) and Y17 ($388.6 \pm$
37
38
391519 0.5 Ma isotope dilution thermal ionization mass spectrometry data; Spencer et al., 2013) were
40
411520 included to monitor accuracy and internal error. We obtained ^{207}Pb -corrected $^{206}\text{Pb}/^{238}\text{Pb}$ ages
42
43
441521 (using Stacey-Kramers common Pb correction in IsoplotR; Vermeesch, 2018) of $1033.41 \pm$
45
46
471522 3.43 Ma for BLR (n=17), 27.99 ± 0.14 for FC (n=10), and $391.94 \pm 1.71 \text{ Ma}$ for Y17 (n=11).
48
49
50
511523 These ages are accurate to within 1.3%, 1.4% and 0.8% of standard values, respectively.
52

531524 All unknowns were additionally bracketed by analyses of international glass standard
54
55
561525 NIST612, that was used as a primary standard for trace elements (Pearce et al., 1997), using
57
581526 ^{44}Ca as the internal standard element (assuming 19.2 wt.% Ca). The spectra were reduced using
59
60
61
62
63
64
65

1527 Iolite v2.5 (Paton et al., 2011), error correlations were recalculated after Schmitz and Schoene
1
21528 (2007), and discordia ages were calculated using IsoplotR (Vermeesch, 2018).

4
51529

71530 **Captions**

111531

141532 Figure 1. Geological setting of the Sistan in the Tetyan realm. **a)** Elevation map with GPS
15
161533 horizontal velocities, in Eurasia-fixed reference frame, for the eastern Alpine–Himalayan belt
17
18
191534 (modified after Vernant et al., 2004), the main Tethyan ophiolites (modified after Khan et al.,
20
211535 2006), the Paleo- and Neo-Tethyan sutures and the main continental blocks implied in the
22
23
241536 Tethyan orogeny. **b)** Shaded relief map from ETOPO1
25
261537 (<http://www.ngdc.noaa.gov/mgg/global/relief/ETOPO1>) with the main Paleo- and Neo-
27
28
291538 Tethyan sutures, the main faults (in *italic*), the orogenic belt (in **bold**) neighboring the Sistan
30
311539 and the supposed marginal basins associated with the closure of the Neo-Tehtys (in orange).

341540 Figure 2. The Sistan orogen **a)** Elevation map with the location of the main Iranian ophiolites,
35
361541 the Cenozoic magmatic provinces (modified after Paul et al., 2010) and the Moho depth
37
38
391542 (modified after Mousavi and Ebbing, 2018). **b)** Schematic structure of the North Sistan belt. **c)**
40
411543 Location of the main targets of this study.

441544 Figure 3. Review of the main information available for the Sistan Orogen: synthetic logs
45
461545 modified from Tirrul et al. (1983), metamorphic landmarks from Bonnet et al. (2018; Amph:
47
48
491546 Amphibolitic facies; BS: blueschist facies; GS: greenschist facies), magmatic landmarks from
50
511547 Jentzer et al. (2020), tectonic landmarks from Jentzer et al. (2017), paleomagnetic from Mattei
52
53
541548 et al. (2005; CCW: counterclockwise rotation) and the geodynamic evolution inferred from
55
561549 these previous studies. Data provide in this study and their integration in the geodynamic
57
58
591550 evolution of the Sistan orogeny are also mentioned.

60
61
62
63
64
65

1551 Figure 4. Structural map of the North Sistan belt. **a)** locations of the anchor points (in black)
1
21552 and metamorphic rocks sampled. **b)** representative structural measurement and position of
3
4
51553 cross-sections.
6
7
81554 Figure 5. Representative sedimentary rocks **a-k)** of the Sefidabeh basin; l-r) of the Neh complex
9
101555 (GPS coordinates in supplementary material 1-logs).
11
12
131556 Figure 6. RSCM results with Tmax obtained localized on the structural map (see details in
14
15
161557 supplementary material 2)
17
18
191558 Figure 7. Overall structure of Birjand ophiolitic ridge. **a)** Location of Birjand ridge ophiolite
20
211559 and our anchor points; **b-d)** Representative tectonic contact; **e)** Structural map of Birjand
22
23
241560 ophiolite ridge; **f-j)** Lithologies of representative outcrops (located on a). GPS coordinates of
25
261561 each photography available in supplementary material 1-ophiolite.
27
28
291562 Figure 8. Representative lithologies of each Birjand ophiolite unit. **a-f)** Unit 1; **g-h)** Unit 2; **i-**
30
311563 **k)** Unit 3. GPS coordinates of each photography available in supplementary material 1-
32
33
341564 ophiolite.
35
36
371565 Figure 9. Representative thin section photomicrographs of the ophiolite lithologies.
38
391566 Abbreviations are from Whitney and Evans (2010).
40
41
421567 Figure 10. Representative outcrops and landscapes of the Sistan. GPS coordinates of each
43
441568 photography available in supplementary material 1-cross-sections.
45
46
471569 Figure 11. Same scale cross-sections across the Sistan. And: Andalusite; BS: Blueschist facies;
48
491570 E: Eclogitic facies; GS: Greenschist facies; J: Jurassic; C: Cretaceous; LC: Lower Cretaceous;
50
511571 UC: Upper Cretaceous; SB: Sefidabeh basin; WU: Western Unit
52
53
541572 Figure 12. Representative thin section and SEM photomicrographs **a-d)** Birjand metasediments;
55
561573 **e-h)** Amphibolitic sole; **i-j)** Metamorphic rocks of the Lut block at the boundary with the Neh
57
58
591574 complex; **k-n)** Dehsalm metamorphic complex
60
61
62
63
64
65

1575 Figure 13. Compositional plots of minerals. **a)** for the Birjand metasediments; **b)** Amphibolitic
1
21576 sole; **c)** Metamorphic rocks of the Lut block at the boundary with the Neh complex; **d)** Dehsalm
3
41577 metamorphic complex. Representative examples are given in supplementary material 2.
5
6
71578 Figure 14. Estimation of the P-T conditions. **a)** On Birjand metasediments using mineral
8
91579 assemblage compared to initiation or mature subduction gradient (Agard et al., 2018, 2020;
10
111580 Bonnet et al., 2019) **b)** On amphibolitic sole using (on top) amphibole-plagioclase
12
131581 thermobarometry and Zr in titanite (grey areas corresponds to P-T conditions observed in
14
151582 metamorphic sole worldwide Agard et al., 2016) or using isopleths on pseudosection for sample
16
171583 15b-15c (mineral assemblage for the fields 1 to 8 are available on supplementary material 3).
18
191584 **c)** On metasimentary rocks of the Lut Block using garnet-biotite thermometry and mineral
20
211585 assemblage on pseudosection for sample 16-72 (3: WM, Bt, Fsp, Ilm, Sil, Qz, H₂O; 4: Bt, Fsp₁,
22
231586 Fsp₂, Ilm, Sil, Qz, H₂O; all mineral assemblage for the fields 1 to 10 are available on
24
251587 supplementary material 3). **d)** On Deh-Salm complex metasedimentary rocks using Ti-in biotite
26
271588 for thermometry, garnet-biotite-aluminosilicate-quartz for thermobarometry and both mineral
28
291589 assemblage and composition on pseudosection for sample 14-29 (7: Grt, Melt, WM, Bt, Fsp,
30
311590 Ky, Qz, Rt, H₂O; 8: Grt, WM, Bt, Fsp, Ky, Qz, Rt, H₂O; 9: Grt, WM, St, Bt, Fsp, Ky, Qz, Rt,
32
331591 H₂O; 33: Grt, Melt, WM, Bt, Fsp, Sil, Qz, Rt, H₂O; 34: Grt, Melt, WM, Bt, Fsp, Sil, Qz, Rt; 35:
34
351592 Grt, Melt, Bt, Fsp, Sil, Qz, Rt; 36: Grt, Melt, Bt, Fsp, Ilm, Sil, Qz, Rt, H₂O; 37: Grt, Melt, WM,
36
371593 Bt, Fsp, Ilm, Sil, Qz, Rt, H₂O; 38: Grt, Melt, WM, Bt, Fsp, Ilm, Sil, Qz, H₂O; 39: Grt, WM, St,
38
391594 Bt, Fsp, Ilm, Sil, Qz, H₂O; 40: WM, Bt, Fsp, Ilm, Sil, Qz, H₂O; all mineral assemblage for the
40
411595 fields 1 to 44 are available on supplementary material 3). The shade of grey on the
42
431596 pseudosection indicate the field variance.
44
45
461597 Figure 15. Synthesis of the geochronological work, including Tera-Wasserburg diagrams
47
481598 showing U-Pb analytical data of titanite with error ellipses of the 95% confidence interval or
49
50
511599 ⁴⁰Ar-³⁹Ar age degassing spectra for amphibole, biotite or white mica. **a)** for ophiolitic gabbro;
52
53
54
55
56
57
58
59
60
61
62
63
64
65

1600 **b-c)** for Birjand metachert; **d-k)** for Neh amphibolitic sole; **l)** for granitoid intrusion; **m)** for
1
21601 Dehsalm metamorphic complex migmatite.
3
4
51602 Figure 16. Synthetic cross-section of the Sistan orogen. And: Andalusite; BS: Blueschist facies;
6
71603 Cong.: Conglomerate; E: Eclogitic facies; Eo: Eocene; GS: greenschist facies; J: Jurassic; C or
8
91604 Cret.: Cretaceous; LC: Lower Cretaceous; UC: Upper Cretaceous; Ng: Neogen; Pe: Paleocen;
10
11
121605 SB: Sefidabeh basin; WU: Western Unit.
13
14
151606 Figure 17. Major metamorphic events associated with the Sistan orogeny. **a)** Results provided
16
171607 by this study ; **b)** Comparison between the HP-BT Ratuk complex metamorphism (Fotoohi Rad
18
191608 et al., 2009, 2005; Angiboust et al., 2013; Bonnet et al., 2018;) and the green-schist to
20
21
221609 amphibolite metamorphism of the Neh complexe.
23
241610 Figure 18. Tectonic reconstruction along NNE-SSW profile (located on Figs. 4) of the Sistan
25
26
271611 from Turonian to present day.
28
29
301612 Figure 19. 3D block diagram emphasizing the initiation of intra-oceanic subduction between 74
31
321613 and 72 Ma.
33
34
351614 Figure 20. Tectonic evolution of the Sistan in the Tethyan real from Late Jurassic to Eocene. BD:
36
371615 Bajgan-Durkan; K: Kandahar; TeH: Torbat-e-Heydarieh; SaSi: Sanandaj-Sirjan.
38
39
401616
41
421617 Table 1. Petrology and mineralogy of the main metamorphic lithologies studied
43
44
451618 Table 2. Comparison between the main inner ophiolite of Iran
46
471619
48
49
501620 Supplementary material 1: GPS coordinates of the studied outcrops
51
521621 Supplementary material 2: Raman results and representative microprobe analyses for minerals
53
541622 of each metamorphic rocks type.
55
56
571623 Supplementary material 3: Bulk composition and mineral assemblage for each pseudosections.
58
591624
60
61
62
63
64
65

1625 **References**

1
2
3
4
5
6
7
8
9
10
11
12
13
14
15
16
17
18
19
20
21
22
23
24
25
26
27
28
29
30
31
32
33
34
35
36
37
38
39
40
41
42
43
44
45
46
47
48
49
50
51
52
53
54
55
56
57
58
59
60
61
62
63
64
65

1626 Agard, P., Monié, P., Gerber, W., Omrani, J., Molinaro, M., Meyer, B., Labrousse, L.,
1627 Vrielynck, B., Jolivet, L., Yamato, P., 2006. Transient, synobduction exhumation of Zagros
1628 blueschists inferred from P-T, deformation, time, and kinematic constraints: Implications for
1629 Neotethyan wedge dynamics: TRANSIENT EXHUMATION PROCESSES IN ZAGROS.
1630 Journal of Geophysical Research: Solid Earth 111, n/a-n/a.
1631 <https://doi.org/10.1029/2005JB004103>
1632 Agard, P., Omrani, J., Jolivet, L., Whitechurch, H., Vrielynck, B., Spakman, W., Monié, P.,
1633 Meyer, B., Wortel, R., 2011. Zagros orogeny: a subduction-dominated process. Geological
1634 Magazine 148, 692–725. <https://doi.org/10.1017/S001675681100046X>
1635 Agard, P., Yamato, P., Soret, M., Prigent, C., Guillot, S., Plunder, A., Dubacq, B., Chauvet, A.,
1636 Monié, P., 2016. Plate interface rheological switches during subduction infancy: Control on
1637 slab penetration and metamorphic sole formation. Earth and Planetary Science Letters 451,
1638 208–220. <https://doi.org/10.1016/j.epsl.2016.06.054>
1639 Ajirlu, M.S., Moazzen, M., Hajjalioghli, R., 2016. Tectonic evolution of the Zagros Orogen in
1640 the realm of the Neotethys between the Central Iran and Arabian Plates: An ophiolite
1641 perspective. Central European Geology 59, 1–27. <https://doi.org/10.1556/24.59.2016.001>
1642 Aleinikoff, J.N., Wintsch, R.P., Tollo, R.P., Unruh, D.M., Fanning, C.M., Schmitz, M.D., 2007.
1643 Ages and origins of rocks of the Killingworth dome, south-central Connecticut: Implications
1644 for the tectonic evolution of southern New England. American Journal of Science 307, 63–118.
1645 <https://doi.org/10.2475/01.2007.04>
1646 Angiboust, S., Agard, P., De Hoog, J.C.M., Omrani, J., Plunder, A., 2013a. Insights on deep,
1647 accretionary subduction processes from the Sistan ophiolitic “mélange” (Eastern Iran). Lithos
1648 156–159, 139–158. <https://doi.org/10.1016/j.lithos.2012.11.007>

1649 Angiboust, S., Agard, P., De Hoog, J.C.M., Omrani, J., Plunder, A., 2013b. Insights on deep,
1
21650 accretionary subduction processes from the Sistan ophiolitic “mélange” (Eastern Iran). *Lithos*
3
4
51651 156–159, 139–158. <https://doi.org/10.1016/j.lithos.2012.11.007>
6
71652 Azizi, H., Stern, R.J., 2019. Jurassic igneous rocks of the central Sanandaj–Sirjan zone (Iran)
8
9
101653 mark a propagating continental rift, not a magmatic arc. *Terra Nova* 31, 415–423.
11
121654 <https://doi.org/10.1111/ter.12404>
13
14
151655 Babazadeh, S.A., De Wever, P., 2004. Early Cretaceous radiolarian assemblages from
16
171656 radiolarites in the Sistan Suture (eastern Iran). *Geodiversitas* 26, 185–206.
18
191657 Bagheri, S., Damani Gol, S., 2020. The eastern Iranian orocline. *Earth-Science Reviews* 210,
20
21
221658 103322. <https://doi.org/10.1016/j.earscirev.2020.103322>
23
241659 Barrier, E., Vrielynck, B., Brouillet, J.-F., Brunet, M.-F., 2018. Paleotectonic reconstruction of
25
26
271660 the Central Tethyan realm. *Atlas of 20 maps*.
28
291661 Berberian, F., Berberian, M., 1981. Tectono-plutonic episodes in Iran. *Zagros Hindu Kush*
30
311662 *Himalaya Geodynamic Evolution* 5–32.
32
33
341663 Berberian, M., Jackson, J.A., Qorashi, M., Talebian, M., Khatib, M., Priestley, K., 2000. The
35
361664 1994 Sefidabeh earthquakes in eastern Iran: blind thrusting and bedding-plane slip on a growing
37
38
391665 anticline, and active tectonics of the Sistan suture zone. *Geophysical Journal International* 142,
40
411666 283–299.
42
43
441667 Berberian, M., King, G.C.P., 1981. Towards a paleogeography and tectonic evolution of Iran.
45
461668 *Canadian Journal of Earth Sciences* 18, 210–265. <https://doi.org/10.1139/e81-019>
47
48
491669 Besse, J., Torcq, F., Gallet, Y., Ricou, L.E., Krystyn, L., Saidi, A., 1998. Late Permian to Late
50
511670 Triassic palaeomagnetic data from Iran: constraints on the migration of the Iranian block
52
53
541671 through the Tethyan Ocean and initial destruction of Pangaea. *Geophysical Journal*
55
561672 *International* 135, 77–92. <https://doi.org/10.1046/j.1365-246X.1998.00603.x>
57
58
59
60
61
62
63
64
65

- 1673 Beyssac, O., Goffé, B., Chopin, C., Rouzaud, J.N., 2002. Raman spectra of carbonaceous
1
21674 material in metasediments: a new geothermometer: RAMAN SPECTROSCOPY OF
3
41675 CARBONACEOUS MATERIAL. *Journal of Metamorphic Geology* 20, 859–871.
6
71676 <https://doi.org/10.1046/j.1525-1314.2002.00408.x>
8
91677 Bonnet, G., Agard, P., Angiboust, S., Monié, P., Jentzer, M., Omrani, J., Whitechurch, H.,
10
11
121678 Fournier, M., 2018. Tectonic slicing and mixing processes along the subduction interface: The
13
141679 Sistan example (Eastern Iran). *Lithos* 310–311, 269–287.
15
161680 <https://doi.org/10.1016/j.lithos.2018.04.016>
18
191681 Bonnet, G., Agard, P., Whitechurch, H., Fournier, M., Angiboust, S., Caron, B., Omrani, J.,
20
21
221682 2020. Fossil seamount in southeast Zagros records intraoceanic arc to back-arc transition: New
23
241683 constraints for the evolution of the Neotethys. *Gondwana Research* 81, 423–444.
25
261684 <https://doi.org/10.1016/j.gr.2019.10.019>
27
28
291685 Boulin, J., 1991. Structures in Southwest Asia and evolution of the eastern Tethys.
30
311686 *Tectonophysics* 196, 211–268.
32
33
341687 Bröcker, M., Fotoohi Rad, G., Abbaslu, F., Rodionov, N., 2014. Geochronology of high-grade
35
361688 metamorphic rocks from the Anjul area, Lut block, eastern Iran. *Journal of Asian Earth Sciences*
37
38
391689 82, 151–162. <https://doi.org/10.1016/j.jseaes.2013.12.021>
40
411690 Bröcker, M., Fotoohi Rad, G., Burgess, R., Theunissen, S., Paderin, I., Rodionov, N., Salimi,
42
43
441691 Z., 2013. New age constraints for the geodynamic evolution of the Sistan Suture Zone, eastern
45
461692 Iran. *Lithos* 170–171, 17–34. <https://doi.org/10.1016/j.lithos.2013.02.012>
47
48
491693 Brunet, M.-F., Korotaev, M.V., Ershov, A.V., Nikishin, A.M., 2003. The South Caspian Basin:
50
511694 a review of its evolution from subsidence modelling. *Sedimentary Geology* 156, 119–148.
52
531695 [https://doi.org/10.1016/S0037-0738\(02\)00285-3](https://doi.org/10.1016/S0037-0738(02)00285-3)
54
55
56
57
58
59
60
61
62
63
64
65

1696 Burg, J.-P., 2018. Geology of the onshore Makran accretionary wedge: Synthesis and tectonic
1
21697 interpretation. *Earth-Science Reviews* 185, 1210–1231.
3
4
51698 <https://doi.org/10.1016/j.earscirev.2018.09.011>
6
71699 Camp, V.E., Griffis, R.J., 1982a. Character, genesis and tectonic setting of igneous rocks in the
8
9
101700 Sistan suture zone, eastern Iran. *Lithos* 15, 221–239.
11
121701 Camp, V.E., Griffis, R.J., 1982b. Character, genesis and tectonic setting of igneous rocks in the
13
14
151702 Sistan suture zone, eastern Iran. *Lithos* 15, 221–239.
16
171703 Cannat, M., Sauter, D., Escartin, J., Lavier, L., Picazo, S., 2009. Oceanic corrugated surfaces
18
191704 and the strength of the axial lithosphere at slow spreading ridges. *Earth and Planetary Science*
20
21
221705 *Letters* 288, 174–183. <https://doi.org/10.1016/j.epsl.2009.09.020>
23
241706 Connolly, J.A.D., 2005. Computation of phase equilibria by linear programming: A tool for
25
26
271707 geodynamic modeling and its application to subduction zone decarbonation. *Earth and*
28
291708 *Planetary Science Letters* 236, 524–541. <https://doi.org/10.1016/j.epsl.2005.04.033>
30
31
321709 Connolly, J.A.D., 1990. Multivariable phase diagrams: an algorithm based on generalized
33
341710 thermodynamics. *American Journal of Science* 290, 666–718.
35
36
371711 Corfield, R.I., Searle, M.P., Pedersen, R.B., 2001. Tectonic Setting, Origin, and Obduction
38
391712 History of the Spontang Ophiolite, Ladakh Himalaya, NW India. *The Journal of Geology* 109,
40
411713 715–736. <https://doi.org/10.1086/323191>
42
43
441714 Davies, J.H., 2013. Global map of solid Earth surface heat flow: Global Surface Heat Flow
45
461715 Map. *Geochemistry, Geophysics, Geosystems* 14, 4608–4622.
47
48
491716 <https://doi.org/10.1002/ggge.20271>
50
511717 Davoudzadeh, M., Soffel, H., Schmidt, K., 1981. On the rotation of the Central-East-Iran
52
53
541718 microplate. *Neues Jahrbuch für Geologie und Paläontologie - Abhandlungen* 180–192.
55
561719 Delaloye, M., Desmons, J., 1980. Ophiolites and mélange terranes in Iran: a geochronological
57
581720 study and its paleotectonic implications. *Tectonophysics* 68, 83–111.
59
60
61
62
63
64
65

- 1721 Delavari, M., Amini, S., Saccani, E., Beccaluva, L., 2009. Geochemistry and Petrogenesis of
1
21722 Mantle Peridotites from the Nehbandan Ophiolitic Complex, Eastern Iran. *Journal of Applied*
3
4
51723 *Sciences* 9, 2671–2687.
6
71724 DeMets, C., Gordon, R.G., Argus, D.F., 2010. Geologically current plate motions. *Geophysical*
8
9
101725 *Journal International* 181, 1–80. <https://doi.org/10.1111/j.1365-246X.2009.04491.x>
11
121726 Dercourt, J. et al, Zonenshain, L.P., Ricou, L.-E., Kazmin, V.G., Le Pichon, X., Knipper, A.L.,
13
141727 Grandjacquet, C., Sbertshikov, I.M., Geysant, J., Lepvrier, C., others, 1986. Geological
15
161728 evolution of the Tethys belt from the Atlantic to the Pamirs since the Lias. *Tectonophysics* 123,
17
18
191729 241–315.
20
21
221730 Dubacq, B., Soret, M., Jewison, E., Agard, P., 2019. Early subduction dynamics recorded by
23
241731 the metamorphic sole of the Mt. Albert ophiolitic complex (Gaspé, Quebec). *Lithos* 334–335,
25
26
271732 161–179. <https://doi.org/10.1016/j.lithos.2019.03.019>
28
291733 Eddy, M.P., Jagoutz, O., Ibañez-Mejia, M., 2017. Timing of initial seafloor spreading in the
30
311734 Newfoundland-Iberia rift. *Geology* 45, 527–530. <https://doi.org/10.1130/G38766.1>
32
33
341735 Eftekhari Nezhad, J., Ohanian, T., Tatevosian, S., Afaghi, A., Hosseini, Z., Ghomashi, A.,
35
361736 Afharian Zadeh, A., Etemadi, N., 1987. Birjand Geological map.
37
38
391737 Ernst, W.G., Liu, J., 1998. Experimental phase-equilibrium study of Al- and Ti-contents of
40
411738 calcic amphibole in MORB; a semiquantitative thermobarometer. *American Mineralogist* 83,
42
43
441739 952–969. <https://doi.org/10.2138/am-1998-9-1004>
45
461740 Escartín, J., Mével, C., Petersen, S., Bonnemains, D., Cannat, M., Andreani, M., Augustin, N.,
47
48
491741 Bezos, A., Chavagnac, V., Choi, Y., Godard, M., Haaga, K., Hamelin, C., Ildefonse, B.,
50
511742 Jamieson, J., John, B., Leleu, T., MacLeod, C.J., Massot-Campos, M., Nomikou, P., Olive, J.A.,
52
531743 Paquet, M., Rommevaux, C., Rothenbeck, M., Steinfuhrer, A., Tominaga, M., Triebe, L.,
54
55
561744 Campos, R., Gracias, N., Garcia, R., 2017. Tectonic structure, evolution, and the nature of
57
581745 oceanic core complexes and their detachment fault zones (13°20'N and 13°30'N, Mid Atlantic
59
60
61
62
63
64
65

1746 Ridge): 13°N MAR CORRUGATED OCEANIC DETACHMENTS. *Geochemistry,*
1
21747 *Geophysics, Geosystems* 18, 1451–1482. <https://doi.org/10.1002/2016GC006775>
3
4
51748 Eshagh, Mehdi, Tenzer, R., Eshagh, Mehrdad, 2019. Elastic thickness of the Iranian lithosphere
6
71749 from gravity and seismic data. *Tectonophysics* 228186.
8
9
101750 <https://doi.org/10.1016/j.tecto.2019.228186>
11
121751 Esmaeily, D., Nédélec, A., Valizadeh, M.V., Moore, F., Cotten, J., 2005. Petrology of the
13
141752 Jurassic Shah-Kuh granite (eastern Iran), with reference to tin mineralization. *Journal of Asian*
15
161753 *Earth Sciences* 25, 961–980. <https://doi.org/10.1016/j.jseaes.2004.09.003>
17
18
191754 Festa, A., Pini, G.A., Ogata, K., Dilek, Y., 2019. Diagnostic features and field-criteria in
20
211755 recognition of tectonic, sedimentary and diapiric mélanges in orogenic belts and exhumed
22
231756 subduction-accretion complexes. *Gondwana Research.*
24
25
261757 <https://doi.org/10.1016/j.gr.2019.01.003>
27
28
291758 Fotoohi Rad, G.R., Droop, G.T.R., Amini, S., Moazzen, M., 2005. Eclogites and blueschists of
30
311759 the Sistan Suture Zone, eastern Iran: A comparison of P–T histories from a subduction mélange.
32
331760 *Lithos* 84, 1–24. <https://doi.org/10.1016/j.lithos.2005.01.007>
34
35
361761 Fotoohi Rad, G.R., Droop, G.T.R., Burgess, R., 2009. Early Cretaceous exhumation of high-
37
381762 pressure metamorphic rocks of the Sistan Suture Zone, eastern Iran. *Geological Journal* 44,
39
40
411763 104–116. <https://doi.org/10.1002/gj.1135>
42
43
441764 Gaina, C., van Hinsbergen, D.J.J., Spakman, W., 2015. Tectonic interactions between India and
45
461765 Arabia since the Jurassic reconstructed from marine geophysics, ophiolite geology, and seismic
47
481766 tomography: INDIA-ARABIA TECTONIC INTERACTIONS. *Tectonics* 34, 875–906.
49
50
511767 <https://doi.org/10.1002/2014TC003780>
52
531768 Gnos, E., Immenhauser, A., Peters, Tj., 1997. Late Cretaceous/early Tertiary convergence
54
551769 between the Indian and Arabian plates recorded in ophiolites and related sediments.
56
57
581770 *Tectonophysics* 271, 1–19. [https://doi.org/10.1016/S0040-1951\(96\)00249-1](https://doi.org/10.1016/S0040-1951(96)00249-1)
59
60
61
62
63
64
65

1771 Green, E.C.R., White, R.W., Diener, J.F.A., Powell, R., Holland, T.J.B., Palin, R.M., 2016.
1
21772 Activity-composition relations for the calculation of partial melting equilibria in metabasic
3
4
51773 rocks. *Journal of Metamorphic Geology* 34, 845–869. <https://doi.org/10.1111/jmg.12211>
6
71774 Guilmette, C., Smit, M.A., van Hinsbergen, D.J.J., Güerer, D., Corfu, F., Charette, B., Maffione,
8
9
101775 M., Rabeau, O., Savard, D., 2018. Forced subduction initiation recorded in the sole and crust
11
121776 of the Semail Ophiolite of Oman. *Nature Geoscience* 11, 688–695.
13
141777 <https://doi.org/10.1038/s41561-018-0209-2>
15
16
171778 Hayden, L.A., Watson, E.B., Wark, D.A., 2008. A thermobarometer for sphene (titanite).
18
191779 *Contributions to Mineralogy and Petrology* 155, 529–540. <https://doi.org/10.1007/s00410-007->
20
21
221780 0256-y
23
241781 Henry, D.J., 2005. The Ti-saturation surface for low-to-medium pressure metapelitic biotites:
25
26
271782 Implications for geothermometry and Ti-substitution mechanisms. *American Mineralogist* 90,
28
291783 316–328. <https://doi.org/10.2138/am.2005.1498>
30
31
321784 Holdaway, M.J., 2000. Application of new experimental and garnet Margules data to the garnet-
33
341785 biotite geothermometer. *American Mineralogist* 85, 881–892. <https://doi.org/10.2138/am->
35
361786 2000-0701
37
38
391787 Holland, T., Blundy, J., 1994. Non-ideal interactions in calcic amphiboles and their bearing on
40
411788 amphibole-plagioclase thermometry. *Contributions to mineralogy and petrology* 116, 433–447.
42
43
441789 Holland, T., Powell, R., 2003. Activity composition relations for phases in petrological
45
461790 calculations: an asymmetric multicomponent formulation. *Contributions to Mineralogy and*
47
48
491791 *Petrology* 145, 492–501. <https://doi.org/10.1007/s00410-003-0464-z>
50
511792 Holland, T.J.B., Powell, R., 2011. An improved and extended internally consistent
52
531793 thermodynamic dataset for phases of petrological interest, involving a new equation of state for
54
55
561794 solids: THERMODYNAMIC DATASET FOR PHASES OF PETROLOGICAL INTEREST.
57
58
59
60
61
62
63
64
65

1795 Journal of Metamorphic Geology 29, 333–383. <https://doi.org/10.1111/j.1525->
1
21796 1314.2010.00923.x
3
4
51797 Hunziker, D., Burg, J.-P., Bouilhol, P., von Quadt, A., 2015. Jurassic rifting at the Eurasian
6
71798 Tethys margin: Geochemical and geochronological constraints from granitoids of North
8
91799 Makran, southeastern Iran. *Tectonics* 34, 571–593. <https://doi.org/10.1002/2014TC003768>
10
11
121800 Jentzer, M., Fournier, M., Agard, P., Omrani, J., Khatib, M.M., Whitechurch, H., 2017.
13
141801 Neogene to Present paleostress field in Eastern Iran (Sistan belt) and implications for regional
15
16
171802 geodynamics: Paleostress Field in Eastern Iran. *Tectonics* 36, 321–339.
18
191803 <https://doi.org/10.1002/2016TC004275>
20
21
221804 Jentzer, M., Whitechurch, H., Agard, P., Ulrich, M., Caron, B., Zarrinkoub, M.H., Kohansal,
23
241805 R., Miguet, L., Omrani, J., Fournier, M., 2020. Late Cretaceous calc-alkaline and adakitic
25
261806 magmatism in the Sistan suture zone (Eastern Iran): Implications for subduction polarity and
27
28
291807 regional tectonics. *Journal of Asian Earth Sciences* 104588.
30
311808 <https://doi.org/10.1016/j.jseaes.2020.104588>
32
33
341809 Jourdan, F., Renne, P.R., 2007. Age calibration of the Fish Canyon sanidine $^{40}\text{Ar}/^{39}\text{Ar}$ dating
35
361810 standard using primary K–Ar standards. *Geochimica et Cosmochimica Acta* 71, 387–402.
37
38
391811 <https://doi.org/10.1016/j.gca.2006.09.002>
40
411812 Kontoyannis, C.G., Vagenas, N.V., 2000. Calcium carbonate phase analysis using XRD and
42
43
441813 FT-Raman spectroscopy. *The Analyst* 125, 251–255. <https://doi.org/10.1039/a908609i>
45
461814 Kouketsu, Y., Mizukami, T., Mori, H., Endo, S., Aoya, M., Hara, H., Nakamura, D., Wallis, S.,
47
48
491815 2014. A new approach to develop the Raman carbonaceous material geothermometer for low-
50
511816 grade metamorphism using peak width: Raman CM geothermometer using FWHM. *Island Arc*
52
531817 23, 33–50. <https://doi.org/10.1111/iar.12057>
54
55
561818 Kurzawa, T., Bröcker, M., Fotoohi Rad, G., Berndt, J., Lisker, F., 2017. Cretaceous high-
57
581819 pressure metamorphism and low pressure overprint in the Sistan Suture Zone, eastern Iran:
59
60
61
62
63
64
65

1820 Additional temperature estimates for eclogites, geological significance of U-Pb zircon ages and
1
21821 Rb-Sr constraints on the timing of exhumation. *Journal of Asian Earth Sciences* 147, 332–344.
3
41822 <https://doi.org/10.1016/j.jseaes.2017.07.051>
5
6
71823 Kylander-Clark, A.R.C., Hacker, B.R., Cottle, J.M., 2013. Laser-ablation split-stream ICP
8
91824 petrochronology. *Chemical Geology* 345, 99–112.
10
111825 <https://doi.org/10.1016/j.chemgeo.2013.02.019>
12
13
141826 Lagabrielle, Y., Vitale Brovarone, A., Ildefonse, B., 2015. Fossil oceanic core complexes
15
161827 recognized in the blueschist metaophiolites of Western Alps and Corsica. *Earth-Science*
17
181828 *Reviews* 141, 1–26. <https://doi.org/10.1016/j.earscirev.2014.11.004>
19
20
211829 Lahfid, A., Beyssac, O., Deville, E., Negro, F., Chopin, C., Goffé, B., 2010. Evolution of the
22
231830 Raman spectrum of carbonaceous material in low-grade metasediments of the Glarus Alps
24
251831 (Switzerland): RSCM in low-grade metasediments. *Terra Nova* 22, 354–360.
26
271832 <https://doi.org/10.1111/j.1365-3121.2010.00956.x>
28
29
30
311833 Lanphere, M.A., Pamic, J., 1983. $^{40}\text{Ar}/^{39}\text{Ar}$ ages and tectonic setting of ophiolite from the
32
331834 Neyriz area, southeast Zagros range, Iran. *Tectonophysics* 245–256.
34
35
361835 Leroy, S., Mauffret, A., Patriat, P., Mercier de Lepinay, B., 2000. An alternative interpretation
37
381836 of the Cayman trough evolution from a reidentification of magnetic anomalies. *Geophysical*
39
401837 *Journal International* 141, 539–557. <https://doi.org/10.1046/j.1365-246x.2000.00059.x>
41
42
431838 Lucazeau, F., 2019. Analysis and mapping of an updated terrestrial heat flow dataset.
44
451839 *Geochemistry, Geophysics, Geosystems*. <https://doi.org/10.1029/2019GC008389>
46
47
481840 Mahmoudi, S., Masoudi, F., Corfu, F., Mehrabi, B., 2010. Magmatic and metamorphic history
49
501841 of the Deh-Salm metamorphic Complex, Eastern Lut block, (Eastern Iran), from U–Pb
51
521842 geochronology. *International Journal of Earth Sciences* 99, 1153–1165.
53
54
551843 <https://doi.org/10.1007/s00531-009-0465-x>
56
57
58
59
60
61
62
63
64
65

- 1844 Masoudi, F., Mehrabi, B., Mahmoudi, S., 2006. Garnet (Almandine-Spessartine) Growth
1
21845 Zoning and Its Application to Constrain Metamorphic History in Dehsalm Complex, Iran 17,
3
4
51846 11.
6
71847 Mattei, M., Cifelli, F., Muttoni, G., Zanchi, A., Berra, F., Mossavvari, F., Eshraghi, S.A., 2012.
8
91848 Neogene block rotation in central Iran: Evidence from paleomagnetic data. Geological Society
10
11
121849 of America Bulletin 14.
13
141850 Mattei, M., Cifelli, F., Muttoni, G., Rashid, H., 2015. Post-Cimmerian (Jurassic-Cenozoic)
15
16
171851 paleogeography and vertical axis tectonic rotations of Central Iran and the Alborz Mountains.
18
191852 Journal of Asian Earth Sciences 102, 92–101. <https://doi.org/10.1016/j.jseaes.2014.09.038>
20
21
221853 Maurizot, P., Fauvelet, E., Eftekhar-Nezhad, J., 1990. Explanatory text of the Gazik quadrangle
23
241854 map 1:250,000.
25
26
271855 Metcalfe, I., 2013. Gondwana dispersion and Asian accretion: Tectonic and palaeogeographic
28
291856 evolution of eastern Tethys. Journal of Asian Earth Sciences 66, 1–33.
30
311857 <https://doi.org/10.1016/j.jseaes.2012.12.020>
32
33
341858 Moazzen, M., Modjarrad, M., Zarrinkoub, M., 2006. Mineral chemistry, petrogenesis and P-T
35
361859 conditions of formation of harzburgitic peridotites from south of Birjand, Eastern Iran. Journal
37
38
391860 of Asian Earth Sciences. <https://doi.org/10.1016/j.jseaes.2005.07.009>
40
411861 Mohammadi, A., Burg, J.-P., Bouilhol, P., Ruh, J., 2016a. U-Pb geochronology and
42
43
441862 geochemistry of Zahedan and Shah Kuh plutons, southeast Iran: Implication for closure of the
45
461863 South Sistan suture zone. Lithos 248–251, 293–308.
47
48
491864 <https://doi.org/10.1016/j.lithos.2016.02.003>
50
511865 Mohammadi, A., Burg, J.-P., Winkler, W., Ruh, J., von Quadt, A., 2016b. Detrital zircon and
52
531866 provenance analysis of Late Cretaceous–Miocene onshore Iranian Makran strata: Implications
54
55
561867 for the tectonic setting. Geological Society of America Bulletin 128, 1481–1499.
57
581868 <https://doi.org/10.1130/B31361.1>
59
60
61
62
63
64
65

- 1869 Montenat, C., 2009. The Mesozoic of Afghanistan. *GeoArabia* 14, 64.
- 1
21870 Mousavi, N., Ebbing, J., 2018. Basement characterization and crustal structure beneath the
3
41871 Arabia–Eurasia collision (Iran): A combined gravity and magnetic study. *Tectonophysics* 731–
5
6
71872 732, 155–171. <https://doi.org/10.1016/j.tecto.2018.03.018>
8
- 91873 Omidianfar, S., Monsef, I., Rahgoshay, M., Zheng, J., Cousens, B., 2020. The middle Eocene
10
11
121874 high-K magmatism in Eastern Iran Magmatic Belt: constraints from U-Pb zircon
13
141875 geochronology and Sr-Nd isotopic ratios. *International Geology Review* 1–18.
15
16
171876 <https://doi.org/10.1080/00206814.2020.1716272>
18
- 191877 Omrani, H., 2017. Geodynamic evolution of the Sabzevar zone, northern central Iranian micro-
20
21
221878 continent. *Miner Petrol* 19. <https://doi.org/10.1007/s00710-017-0505-3>
23
- 241879 Omrani, J., Agard, P., Whitechurch, H., Benoit, M., Prouteau, G., Jolivet, L., 2008. Arc-
25
261880 magmatism and subduction history beneath the Zagros Mountains, Iran: A new report of
27
28
291881 adakites and geodynamic consequences. *Lithos* 106, 380–398.
30
311882 <https://doi.org/10.1016/j.lithos.2008.09.008>
32
- 33
341883 Ozsvárt, P., Bahramnejad, E., Bagheri, S., Sharifi, M., 2020. New Albian (Cretaceous)
35
361884 radiolarian age constraints for the Dumak ophiolitic mélange from the Shuru area, Eastern Iran.
37
38
391885 *Cretaceous Research* 104451. <https://doi.org/10.1016/j.cretres.2020.104451>
40
- 411886 Pang, K.-N., Chung, S.-L., Zarrinkoub, M.H., Khatib, M.M., Mohammadi, S.S., Chiu, H.-Y.,
42
43
441887 Chu, C.-H., Lee, H.-Y., Lo, C.-H., 2013. Eocene–Oligocene post-collisional magmatism in the
45
461888 Lut–Sistan region, eastern Iran: Magma genesis and tectonic implications. *Lithos* 180–181,
47
48
491889 234–251. <https://doi.org/10.1016/j.lithos.2013.05.009>
50
- 511890 Pang, K.-N., Chung, S.-L., Zarrinkoub, M.H., Mohammadi, S.S., Yang, H.-M., Chu, C.-H.,
52
531891 Lee, H.-Y., Lo, C.-H., 2012. Age, geochemical characteristics and petrogenesis of Late
54
55
561892 Cenozoic intraplate alkali basalts in the Lut–Sistan region, eastern Iran. *Chemical Geology*
57
581893 306–307, 40–53. <https://doi.org/10.1016/j.chemgeo.2012.02.020>
59
60
61
62
63
64
65

1894 Paton, C., Hellstrom, J., Paul, B., Woodhead, J., Hergt, J., 2011. Iolite: Freeware for the
1
21895 visualisation and processing of mass spectrometric data. *Journal of Analytical Atomic*
3
41896 *Spectrometry* 26, 2508. <https://doi.org/10.1039/c1ja10172b>
6
71897 Pearce, N.J.G., Perkins, W.T., Westgate, J.A., Gorton, M.P., Jackson, S.E., Neal, C.R.,
8
91898 Chenery, S.P., 1997. A Compilation of New and Published Major and Trace Element Data for
10
121899 NIST SRM 610 and NIST SRM 612 Glass Reference Materials. *Geostandards and*
13
141900 *Geoanalytical Research* 21, 115–144. <https://doi.org/10.1111/j.1751-908X.1997.tb00538.x>
15
16
171901 Picazo, S., Cannat, M., Delacour, A., Escartin, J., Rouméjon, S., Silantyev, S., 2012.
18
191902 Deformation associated with the denudation of mantle-derived rocks at the Mid-Atlantic Ridge
20
21
221903 13°-15°N: The role of magmatic injections and hydrothermal alteration: DENUDATION OF
23
241904 ULTRAMAFIC ROCKS. *Geochemistry, Geophysics, Geosystems* 13.
25
261905 <https://doi.org/10.1029/2012GC004121>
27
28
291906 Pirnia, T., 2020. Cretaceous tectonic evolution of the Neo-Tethys in Central Iran: Evidence
30
311907 from petrology and age of the Nain-Ashin ophiolitic basalts. *Geoscience Frontiers* 25.
32
33
341908 Plunder, A., Agard, P., Chopin, C., Soret, M., Okay, A.I., Whitechurch, H., 2016. Metamorphic
35
361909 sole formation, emplacement and blueschist facies overprint: early subduction dynamics
37
38
391910 witnessed by western Turkey ophiolites. *Terra Nova* 28, 329–339.
40
411911 <https://doi.org/10.1111/ter.12225>
42
43
441912 Pouchou, J.-L., Pichoir, F., 1991. Quantitative Analysis of Homogeneous or Stratified
45
461913 Microvolumes Applying the Model “PAP,” in: *Electron Probe Quantitation* 31–75.
47
48
491914 Richards, J.P., Şengör, A.M.C., 2017. Did Paleo-Tethyan anoxia kill arc magma fertility for
50
511915 porphyry copper formation? *Geology* 45, 591–594. <https://doi.org/10.1130/G38954.1>
52
53
541916 Richards, J.P., Sholeh, A., 2016. Chapter 7 The Tethyan Tectonic History and Cu-Au
55
561917 Metallogeny of Iran 20.
57
58
59
60
61
62
63
64
65

1918 Robert, A.M.M., Letouzey, J., Kavooosi, M.A., Sherkati, S., Müller, C., Vergés, J., Aghababaei,
1
21919 A., 2014. Structural evolution of the Kopeh Dagh fold-and-thrust belt (NE Iran) and interactions
3
4
51920 with the South Caspian Sea Basin and Amu Darya Basin. *Marine and Petroleum Geology* 57,
6
71921 68–87. <https://doi.org/10.1016/j.marpetgeo.2014.05.002>
8
9
101922 Rodriguez, M., Huchon, P., Chamot-Rooke, N., Fournier, M., Delescluse, M., Smit, J., Plunder,
11
121923 A., Calvès, G., Ninkabou, D., Pubellier, M., François, T., Agard, P., Gorini, C., 2020.
13
141924 Successive shifts of the India-Africa transform plate boundary during the Late Cretaceous-
15
161925 Paleogene interval: Implications for ophiolite emplacement along transforms. *Journal of Asian*
17
18
191926 *Earth Sciences* 191, 104225. <https://doi.org/10.1016/j.jseaes.2019.104225>
20
21
221927 Rossetti, F., Nasrabad, M., Theye, T., Gerdes, A., Monié, P., Lucci, F., Vignaroli, G., 2014.
23
241928 Adakite differentiation and emplacement in a subduction channel: The late Paleocene Sabzevar
25
261929 magmatism (NE Iran). *Geological Society of America Bulletin* 27.
27
28
291930 Rossetti, F., Nasrabad, M., Vignaroli, G., Theye, T., Gerdes, A., Razavi, M.H., Vaziri, H.M.,
30
311931 2010. Early Cretaceous migmatitic mafic granulites from the Sabzevar range (NE Iran):
32
33
341932 implications for the closure of the Mesozoic peri-Tethyan oceans in central Iran. *Terra Nova*
35
361933 22, 26–34. <https://doi.org/10.1111/j.1365-3121.2009.00912.x>
37
38
391934 Saccani, E., Delavari, M., Beccaluva, L., Amini, S., 2010. Petrological and geochemical
40
411935 constraints on the origin of the Nehbandan ophiolitic complex (eastern Iran): Implication for
42
43
441936 the evolution of the Sistan Ocean. *Lithos* 117, 209–228.
45
461937 <https://doi.org/10.1016/j.lithos.2010.02.016>
47
48
491938 Schmitz, M.D., Bowring, S.A., 2001. U-Pb zircon and titanite systematics of the Fish Canyon
50
511939 Tuff: an assessment of high-precision U-Pb geochronology and its application to young
52
531940 volcanic rocks. *Geochimica et Cosmochimica Acta* 65, 2571–2587.
54
55
561941 [https://doi.org/10.1016/S0016-7037\(01\)00616-0](https://doi.org/10.1016/S0016-7037(01)00616-0)
57
58
59
60
61
62
63
64
65

- 1942 Schmitz, M.D., Schoene, B., 2007. Derivation of isotope ratios, errors, and error correlations
1
21943 for U-Pb geochronology using ^{205}Pb - ^{235}U -(^{233}U)-spiked isotope dilution thermal
3
41944 ionization mass spectrometric data: U-PB ISOTOPE RATIO DERIVATION. *Geochemistry,*
5
6
71945 *Geophysics, Geosystems* 8, n/a-n/a. <https://doi.org/10.1029/2006GC001492>
8
91946 Schwartz, S., Guillot, S., Reynard, B., Lafay, R., Debret, B., Nicollet, C., Lanari, P., Auzende,
10
11
121947 A.L., 2013. Pressure–temperature estimates of the lizardite/antigorite transition in high pressure
13
141948 serpentinites. *Lithos* 178, 197–210. <https://doi.org/10.1016/j.lithos.2012.11.023>
15
16
171949 Sengor, A.M.C., Altiner, D., Cin, A., Ustaömer, T., Hsü, K.J., 1988. Origin and assembly of
18
191950 the Tethyside orogenic collage at the expense of Gondwana Land. Geological Society, London,
20
21
221951 *Special Publications* 37, 119–181. <https://doi.org/10.1144/GSL.SP.1988.037.01.09>
23
241952 Sepidbar, F., Frederico, L., Habib, B., Mohamed Zaki, K., Peng, J., 2020. Geochemistry and
25
26
271953 tectonic significance of the Fannuj-Maskutan SSZ-type ophiolite (Inner Makran, SE Iran).
28
291954 *International Geology Review* 29. <https://doi.org/10.1080/00206814.2020.1753118>
30
311955 Seton, M., Müller, R.D., Zahirovic, S., Gaina, C., Torsvik, T., Shephard, G., Talsma, A., Gurnis,
32
33
341956 M., Turner, M., Maus, S., Chandler, M., 2012. Global continental and ocean basin
35
361957 reconstructions since 200Ma. *Earth-Science Reviews* 113, 212–270.
37
38
391958 <https://doi.org/10.1016/j.earscirev.2012.03.002>
40
411959 Siehl, A., 2017. Structural setting and evolution of the Afghan orogenic segment – a review.
42
43
441960 Geological Society, London, *Special Publications* 427, 57–88. <https://doi.org/10.1144/SP427.8>
45
461961 Soffel, H.C., Davoudzadeh, M., Rolf, C., Schmidt, S., 1996. New palaeomagnetic data from
47
48
491962 Central Iran and a Triassic palaeoreconstruction. *Geologische Rundschau* 85, 293–302.
50
511963 <https://doi.org/10.1007/s005310050075>
52
531964 Soffel, H.C., Förster, H.G., 1984. Polar Wander Path of the Central-East-Iran Microplate
54
55
561965 Including New Results. *Neues Jahrbuch für Geologie und Paläontologie - Abhandlungen* 168,
57
581966 165–172. <https://doi.org/10.1127/njgpa/168/1984/165>
59
60
61
62
63
64
65

- 1967 Soret, M., Agard, P., Dubacq, B., Plunder, A., Yamato, P., 2017. Petrological evidence for
1 stepwise accretion of metamorphic soles during subduction infancy (Semail ophiolite, Oman
21968 and UAE). *Journal of Metamorphic Geology*. <https://doi.org/10.1111/jmg.12267>
3
41969
5
6
71970 Spandler, C., Hammerli, J., Sha, P., Hilbert-Wolf, H., Hu, Y., Roberts, E., Schmitz, M., 2016.
8
91971 MKED1: A new titanite standard for in situ analysis of Sm–Nd isotopes and U–Pb
10
111972 geochronology. *Chemical Geology* 425, 110–126.
12
13
141973 <https://doi.org/10.1016/j.chemgeo.2016.01.002>
15
16
171974 Spencer, K.J., Hacker, B.R., Kylander-Clark, A.R.C., Andersen, T.B., Cottle, J.M., Stearns,
18
191975 M.A., Poletti, J.E., Seward, G.G.E., 2013. Campaign-style titanite U–Pb dating by laser-
20
211976 ablation ICP: Implications for crustal flow, phase transformations and titanite closure. *Chemical*
22
23
241977 *Geology* 341, 84–101. <https://doi.org/10.1016/j.chemgeo.2012.11.012>
25
26
271978 Stampfli, G.M., Borel, G.D., 2002. A plate tectonic model for the Paleozoic and Mesozoic
28
291979 constrained by dynamic plate boundaries and restored synthetic oceanic isochrons. *Earth and*
30
311980 *Planetary Science Letters* 196, 17–33. [https://doi.org/10.1016/S0012-821X\(01\)00588-X](https://doi.org/10.1016/S0012-821X(01)00588-X)
32
33
341981 Stöcklin, J., 1974. Possible ancient continental margins in Iran. *The Geology of continental*
35
361982 *Margins* 873–887.
37
38
391983 Tirrul, R., Bell, I.R., Griffis, R.J., Camp, V.E., 1983. The Sistan suture zone of eastern Iran.
40
411984 *Geological Society of America Bulletin* 94, 134–150.
42
43
441985 Verdel, C., Wernicke, B.P., Hassanzadeh, J., Guest, B., 2011. A Paleogene extensional arc
45
461986 flare-up in Iran: iranian volcanism. *Tectonics* 30, n/a-n/a.
47
481987 <https://doi.org/10.1029/2010TC002809>
49
50
511988 Vermeesch, P., 2018. IsoplotR: A free and open toolbox for geochronology. *Geoscience*
52
531989 *Frontiers* 9, 1479–1493. <https://doi.org/10.1016/j.gsf.2018.04.001>
54
55
561990 Wakabayashi, J., Dilek, Y., 2003. What constitutes ‘emplacement’ of an ophiolite?:
57
581991 *Mechanisms and relationship to subduction initiation and formation of metamorphic soles.*
59
60
61
62
63
64
65

1992 Geological Society, London, Special Publications 218, 427–447.
1
21993 <https://doi.org/10.1144/GSL.SP.2003.218.01.22>
3
41994 Walker, R.T., Gans, P., Allen, M.B., Jackson, J., Khatib, M., Marsh, N., Zarrinkoub, M., 2009.
5
6
71995 Late Cenozoic volcanism and rates of active faulting in eastern Iran. *Geophysical Journal*
8
91996 *International* 177, 783–805. <https://doi.org/10.1111/j.1365-246X.2008.04024.x>
10
11
121997 Walker, R.T., Khatib, M.M., 2006. Active faulting in the Birjand region of NE Iran: active
13
141998 faulting at Birjand in NE Iran. *Tectonics* 25, n/a-n/a. <https://doi.org/10.1029/2005TC001871>
15
16
171999 White, R.W., Powell, R., Clarke, G.L., 2002. The interpretation of reaction textures in Fe-rich
18
192000 metapelitic granulites of the Musgrave Block, central Australia: constraints from mineral
20
21
222001 equilibria calculations in the system $K_2O-FeO-MgO-Al_2O_3-SiO_2-H_2O-TiO_2-Fe_2O_3$:
23
242002 REACTION TEXTURES, MUSGRAVE BLOCK GRANULITES. *Journal of Metamorphic*
25
26
272003 *Geology* 20, 41–55. <https://doi.org/10.1046/j.0263-4929.2001.00349.x>
28
292004 White, R.W., Powell, R., Holland, T.J.B., Johnson, T.E., Green, E.C.R., 2014. New mineral
30
312005 activity-composition relations for thermodynamic calculations in metapelitic systems. *Journal*
32
33
342006 *of Metamorphic Geology* 32, 261–286. <https://doi.org/10.1111/jmg.12071>
35
362007 Zarrinkoub, M. H., Pang, K.-N., Chung, S.-L., Khatib, M.M., Mohammadi, S.S., Chiu, H.-Y.,
37
38
392008 Lee, H.-Y., 2012a. Zircon U-Pb age and geochemical constraints on the origin of the Birjand
40
412009 ophiolite, Sistan suture zone, eastern Iran. *Lithos* 154, 392–405.
42
43
442010 <https://doi.org/10.1016/j.lithos.2012.08.007>
45
462011 Zarrinkoub, M. H., Mohammadi, S.S., Khatib, M.H., 2012b. Evaluation of adakites in the
47
48
492012 northern part of Sistan suture zone, eastern Iran, for porphyry mineralization. *Recent*
50
512013 *Researches in Environmental and Geological Sciences* 4.
52
532014
54
55
56
57
58
59
60
61
62
63
64
65

March 10, 2021

Professor M. Santosh
Editor-In-chief
Gondwana Research

Dear Editor,

Please find enclosed a manuscript entitled:

“The Sistan orogen (Eastern Iran): Tectonic evolution and significance within the Tethyan realm”

by Michael Jentzer, Philippe Agard, Guillaume Bonnet, Patrick Monié, Marc Fournier, Hubert Whitechurch, Jafar Omrani, Mohammad Hossein Zarrinkoub, Mohammad Mahdi Khatib, Reza Kohansal, Damien Do Couto, Camille Godbillot and Dia Ninkabou that we wish to submit for publication to Gondwana Research.

We were invited some time ago by Timothy Horscroft to submit this work to your journal (potentially tagged as a GR Focus Review).

Gondwana Research seems indeed particularly well suited for our ms: this work provides a fully original, comprehensive petrological and tectonic study of the Sistan orogen, i.e. the belt formed as a result of the convergence between two Gondwana-derived Cimmerian Blocks, namely the Lut block and the Afghan block.

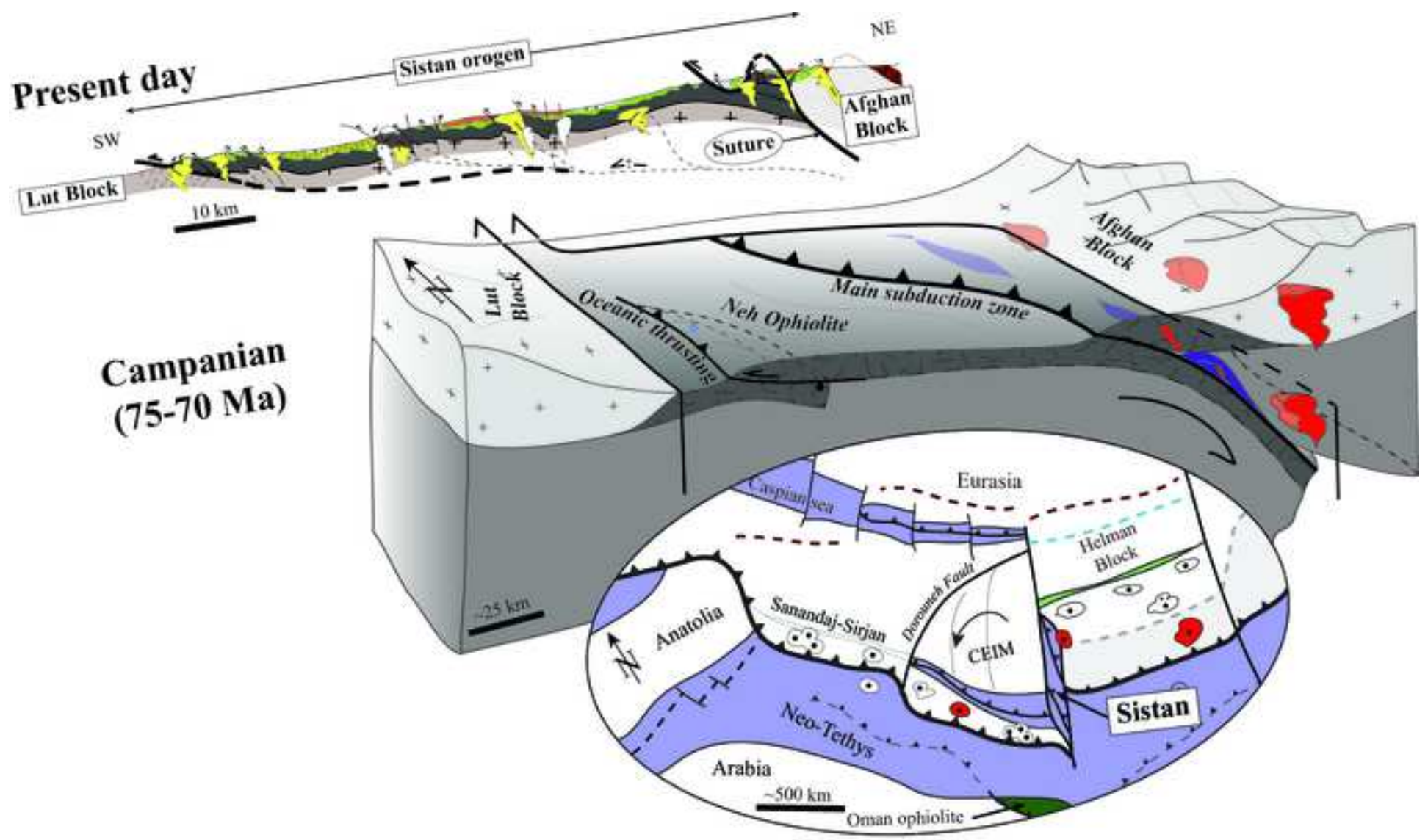
Results allow to reappraise the geodynamic evolution of the entire region and of the Neo-Tethyan realm. We therefore feel that this ms might be of interest to the broad readership of Gondwana Research, as well as to our Iranian colleagues.

Hoping you will find the enclosed manuscript fit for review, and looking forward to hearing from you,

Best regards,

Michael Jentzer

(corresponding author, email: michael.jentzer@upmc.fr)



Highlights:

- Sistan ocean opened as a pull apart basin at ~125 Ma with a slow spreading rate.
- Closure of the Sistan started since 90 Ma with a NE-dipping subduction.
- 73 Ma metamorphic sole argues for an oceanic thrusting inducing the obduction process.
- Sistan recorded both ~90 and ~75 Ma geodynamic events affecting the Tethys closure.

Fig 1

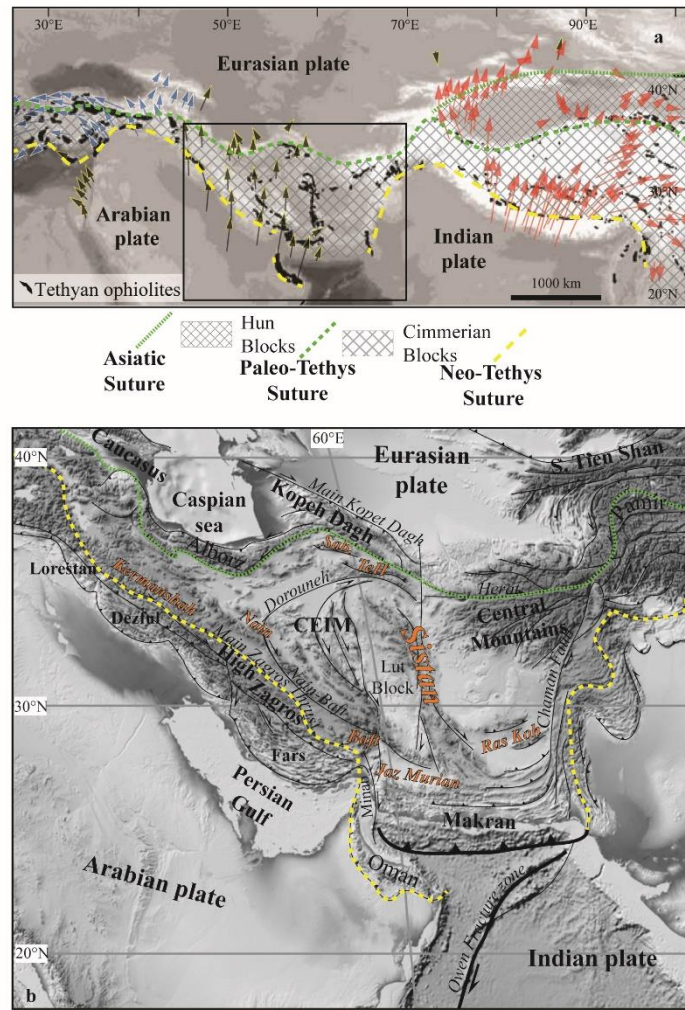


Fig 2

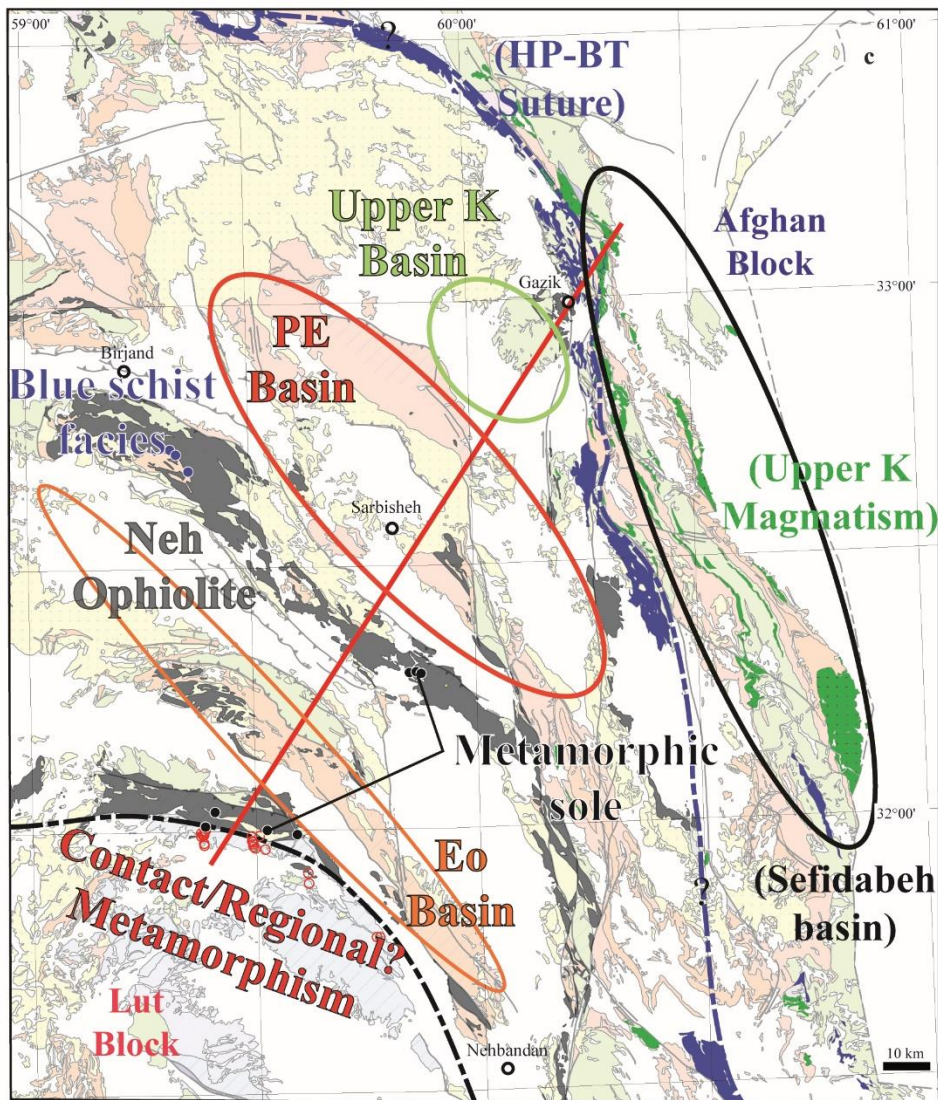
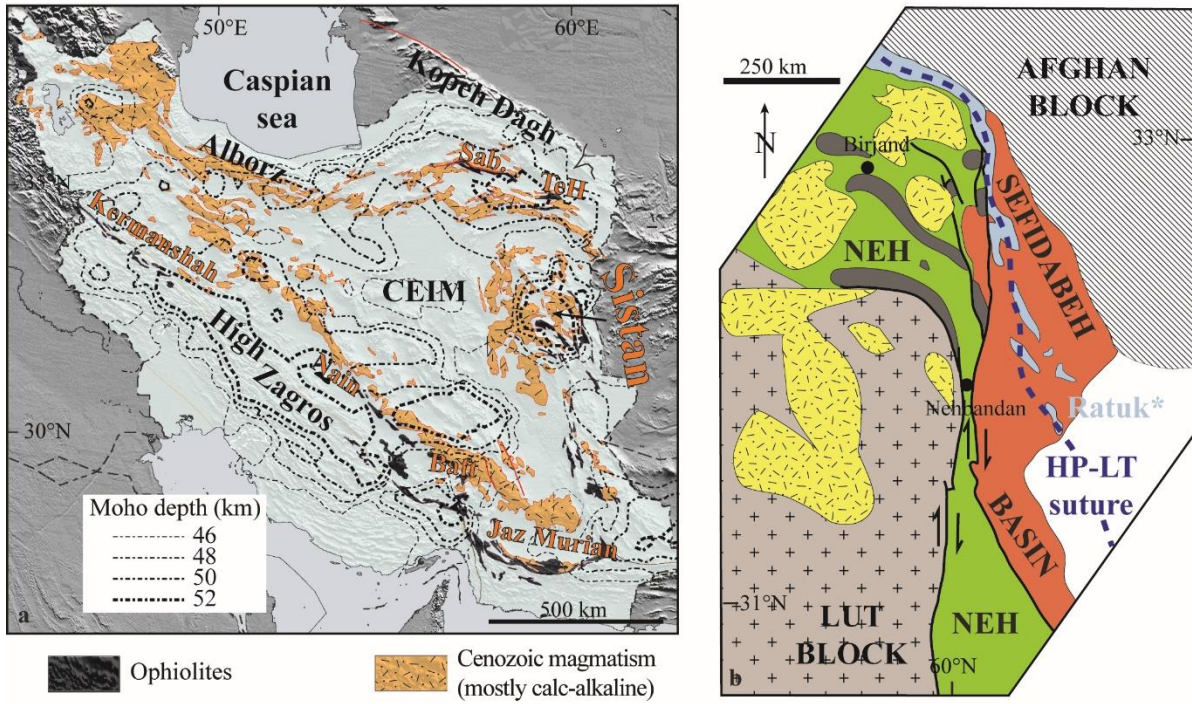


Fig. 3

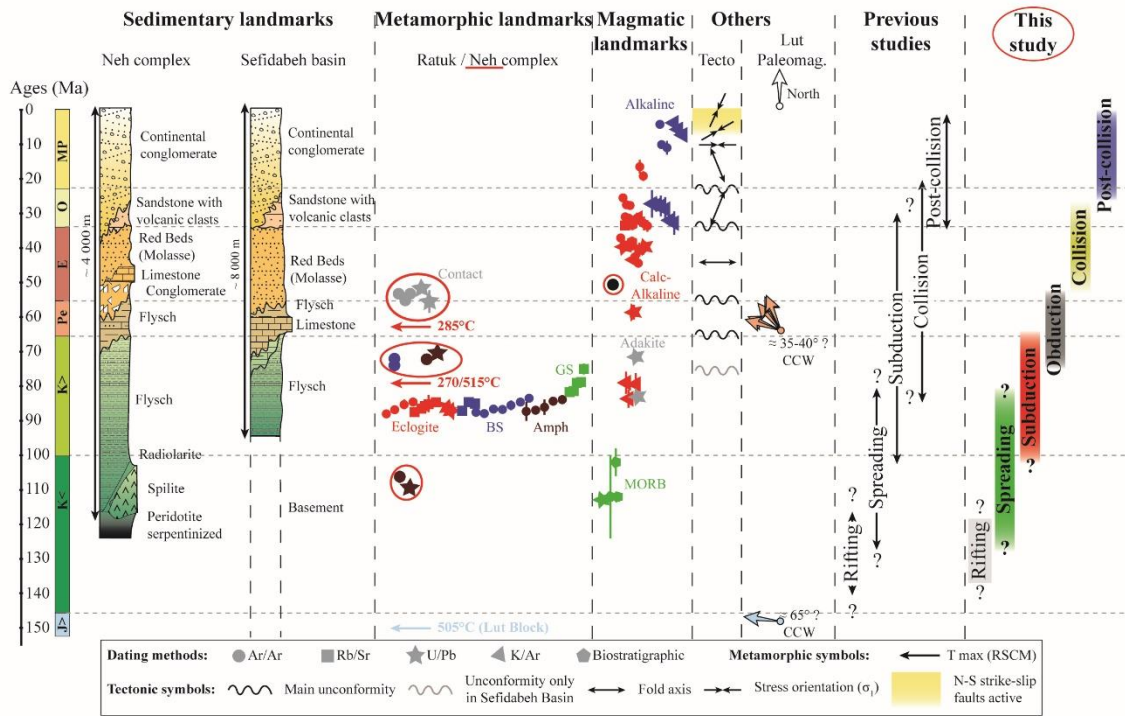
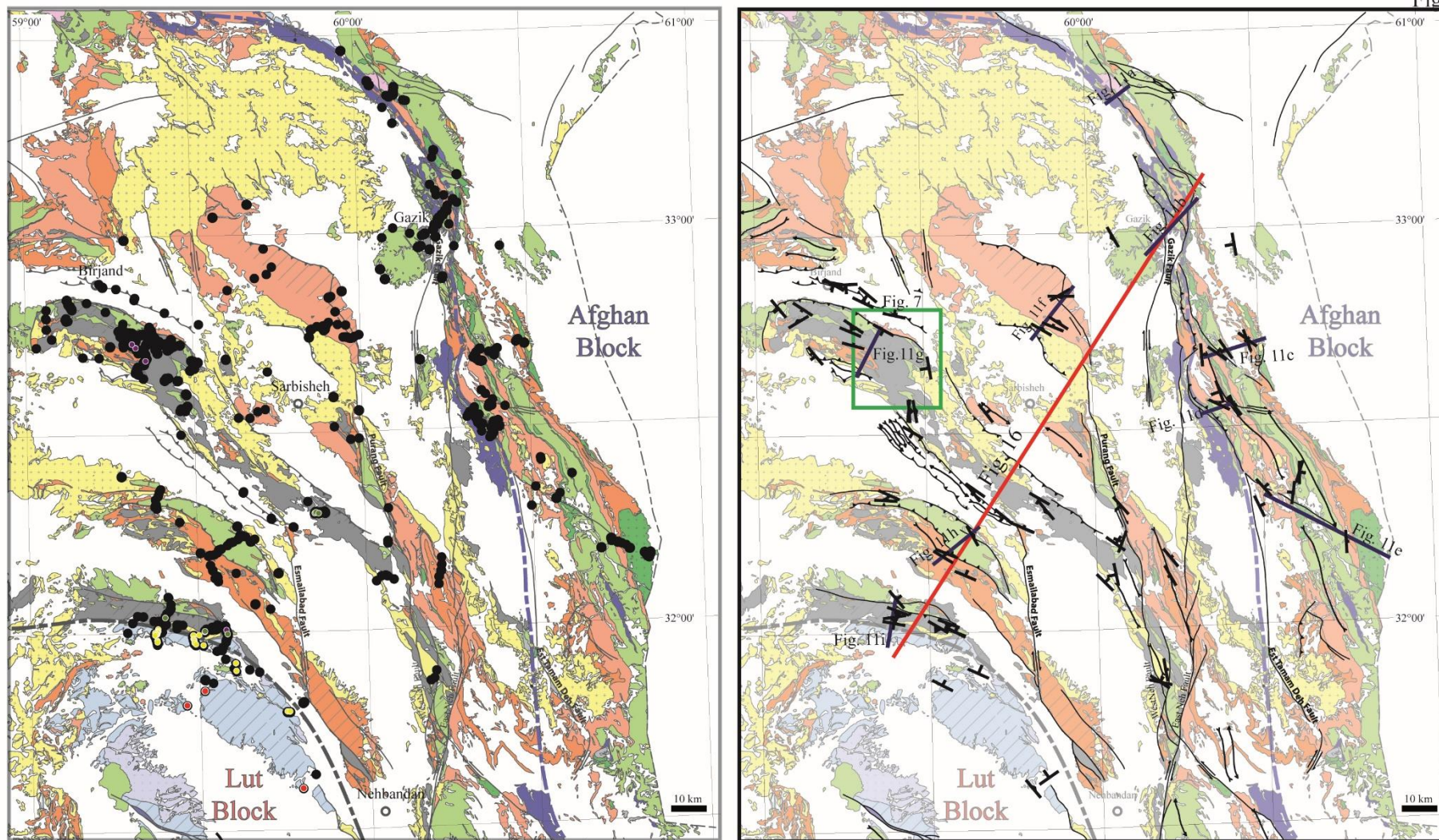


Fig. 4



Dehsalm metamorphic complex

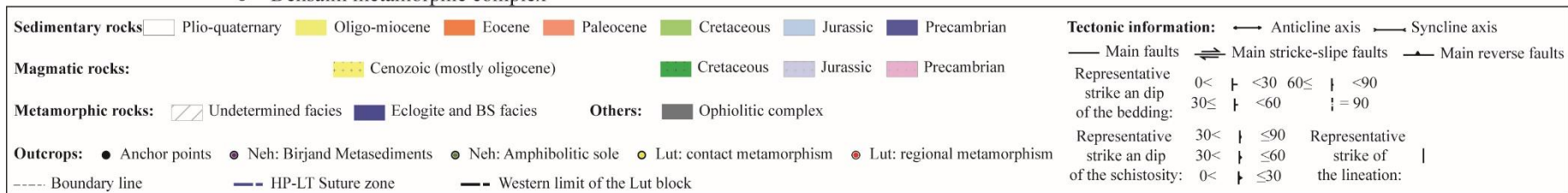


Fig. 5

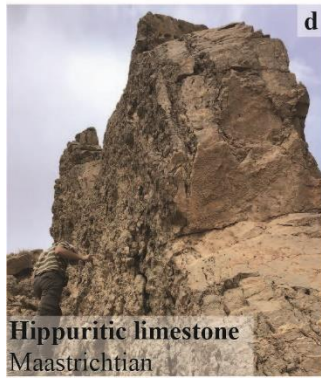


Fig. 5-continued

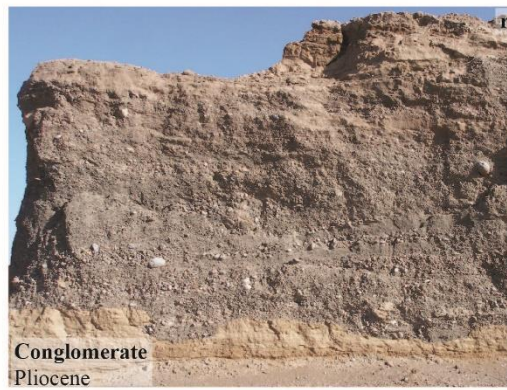
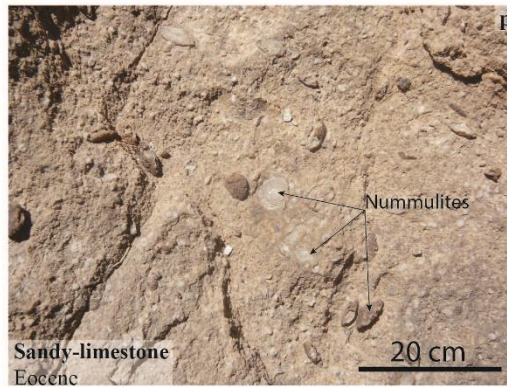
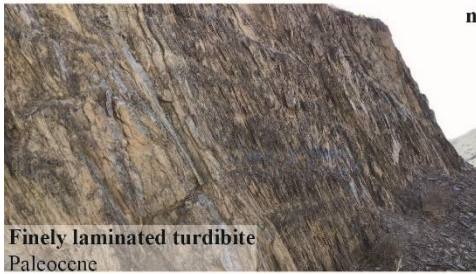


Fig. 6

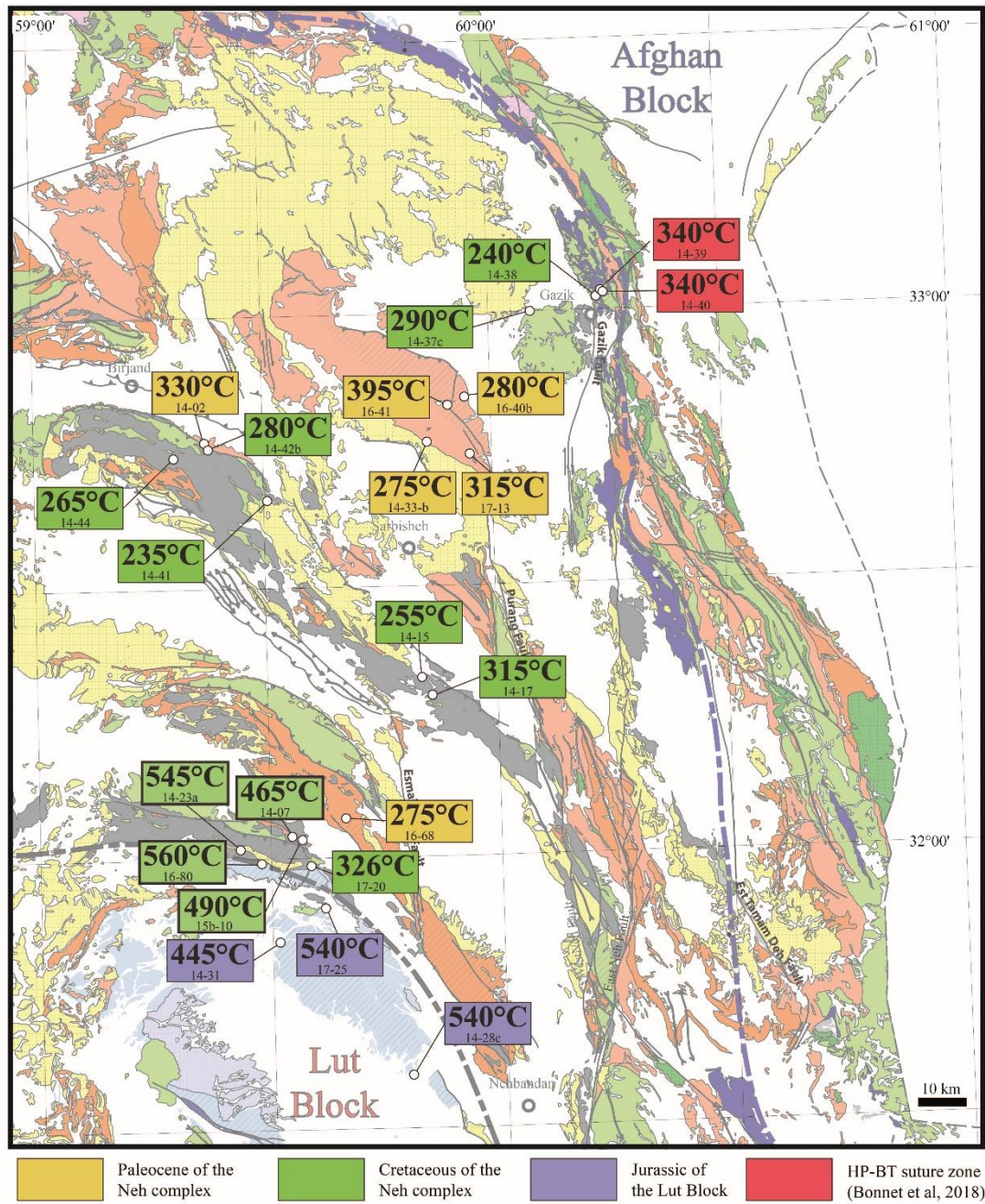


Fig 7

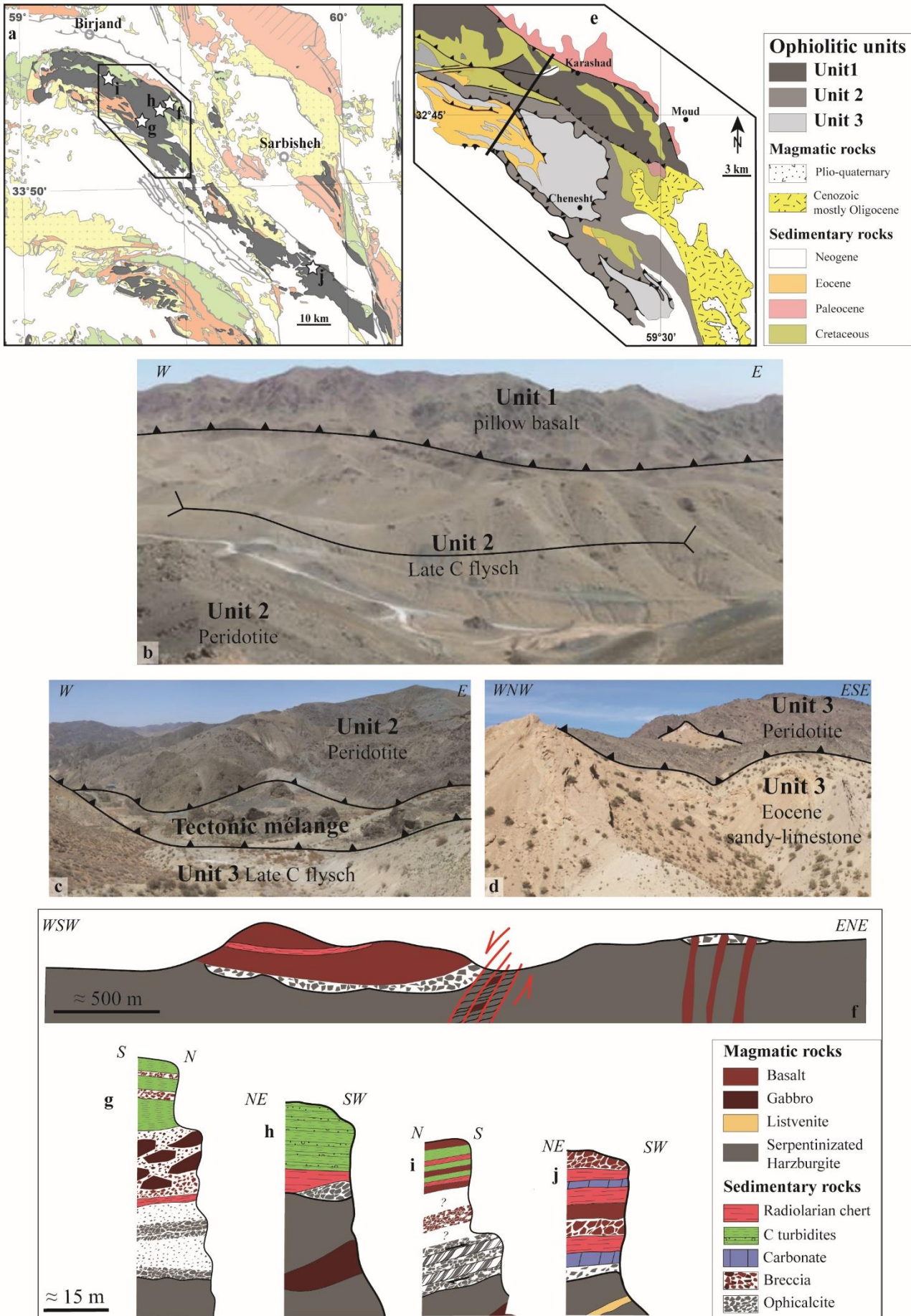


Fig 8

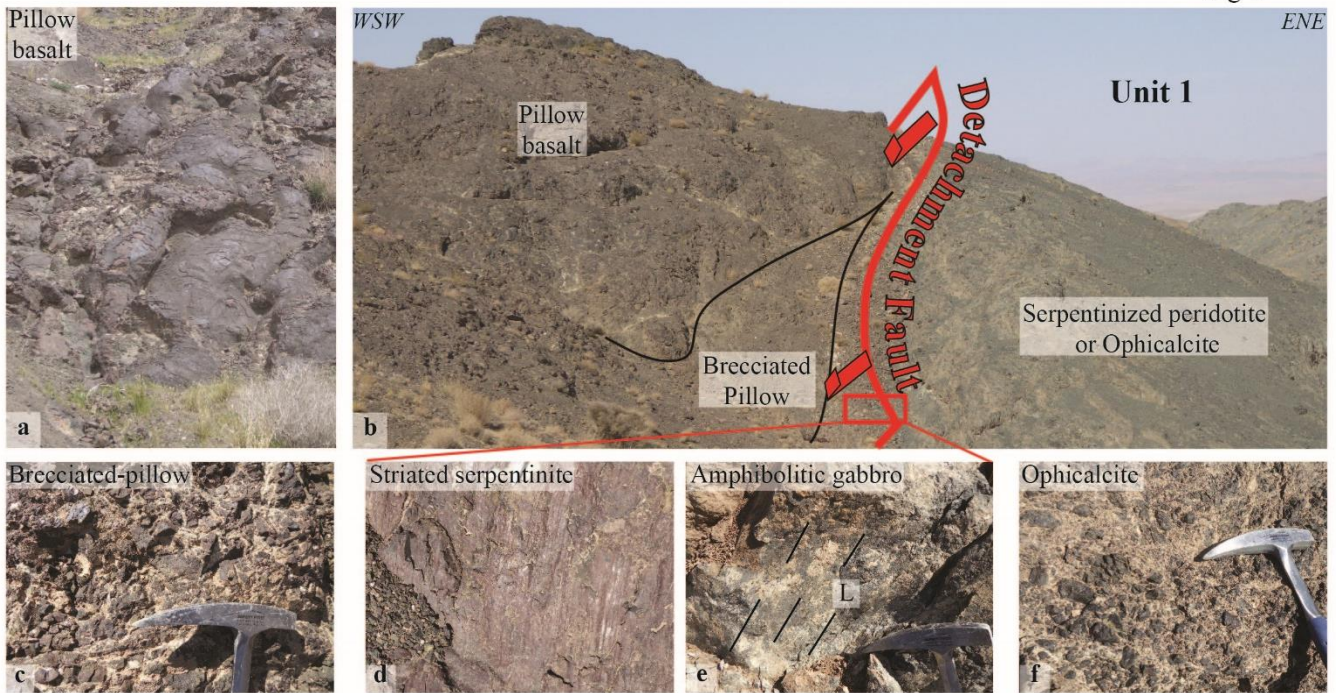


Fig 8 continued

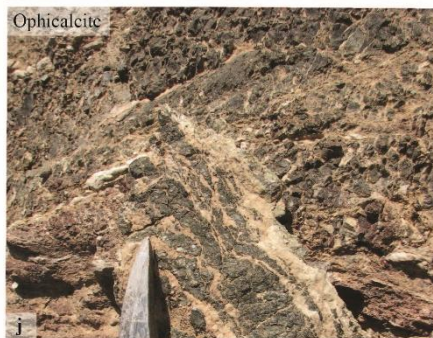
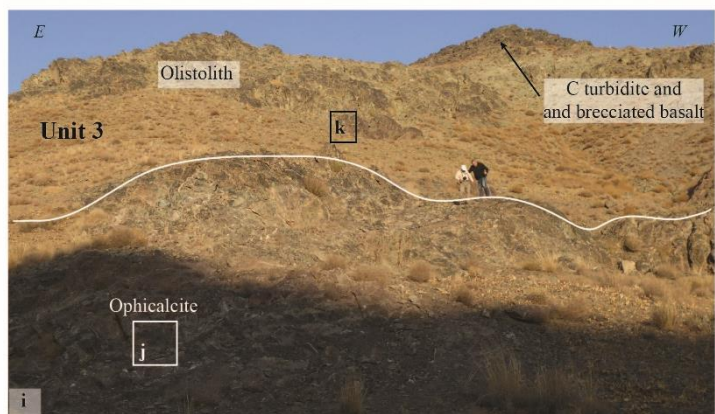
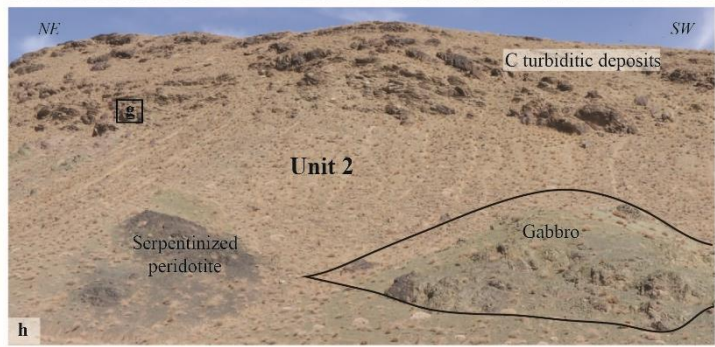


Fig 9

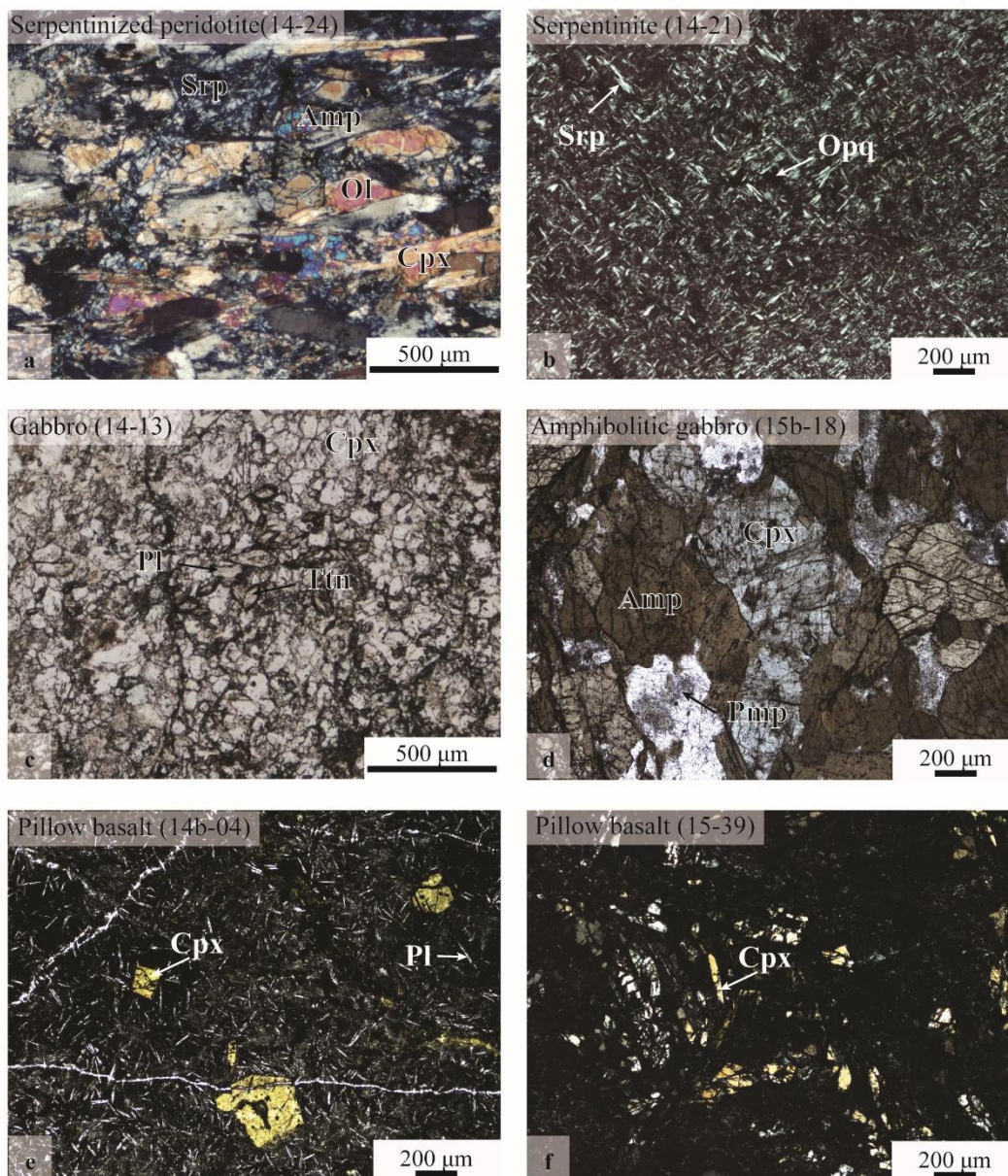


Fig 10

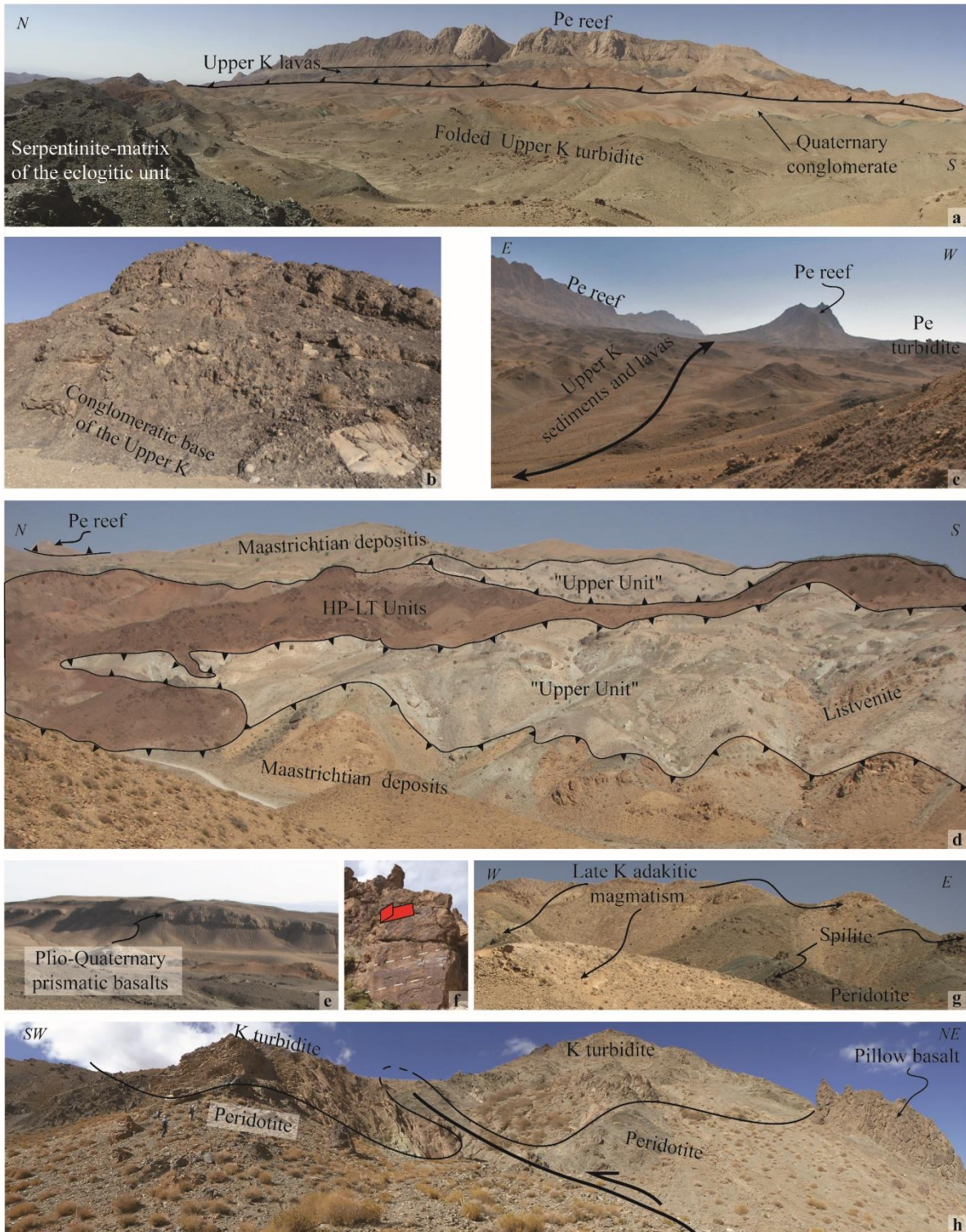
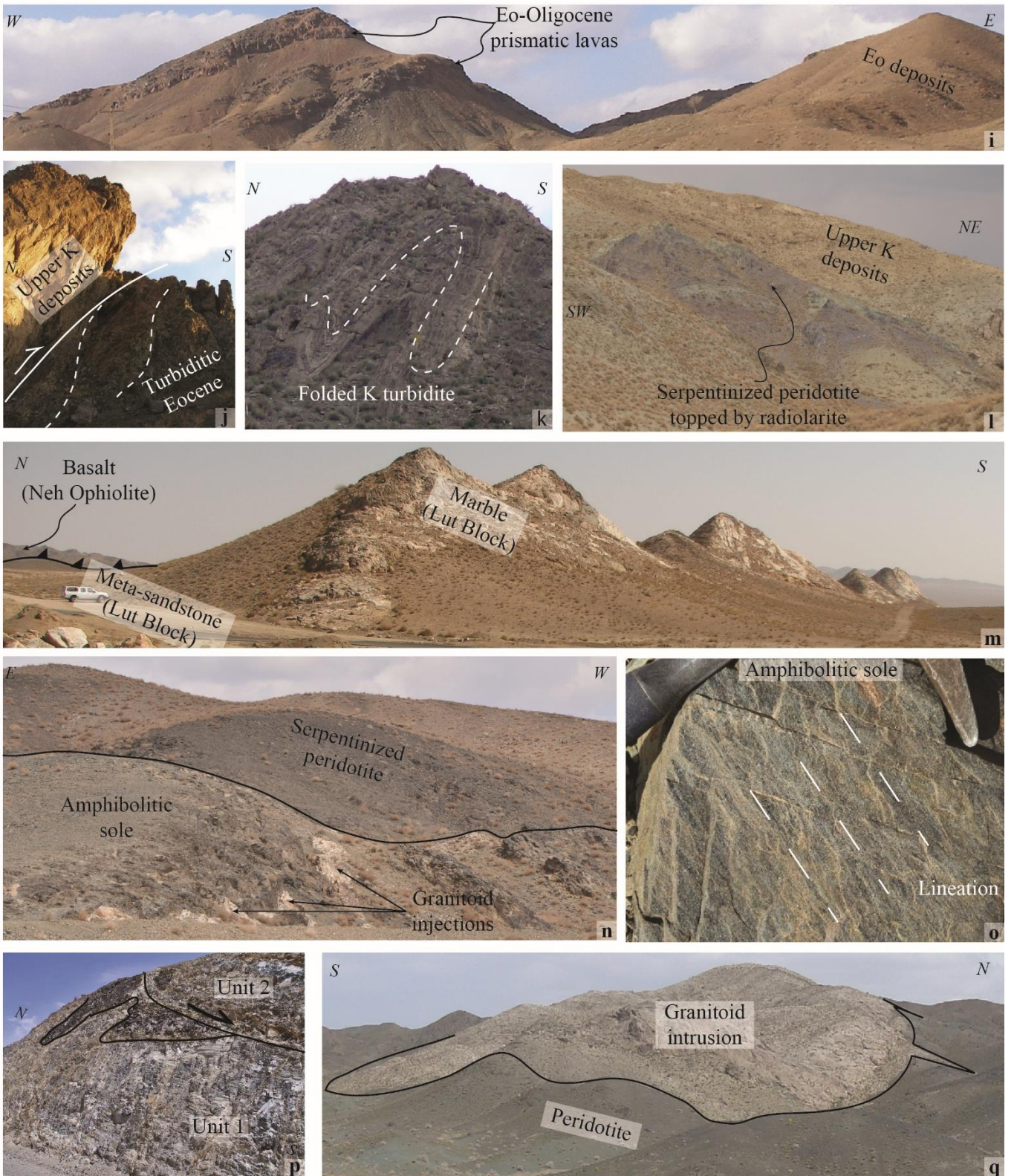


Fig 10 continued



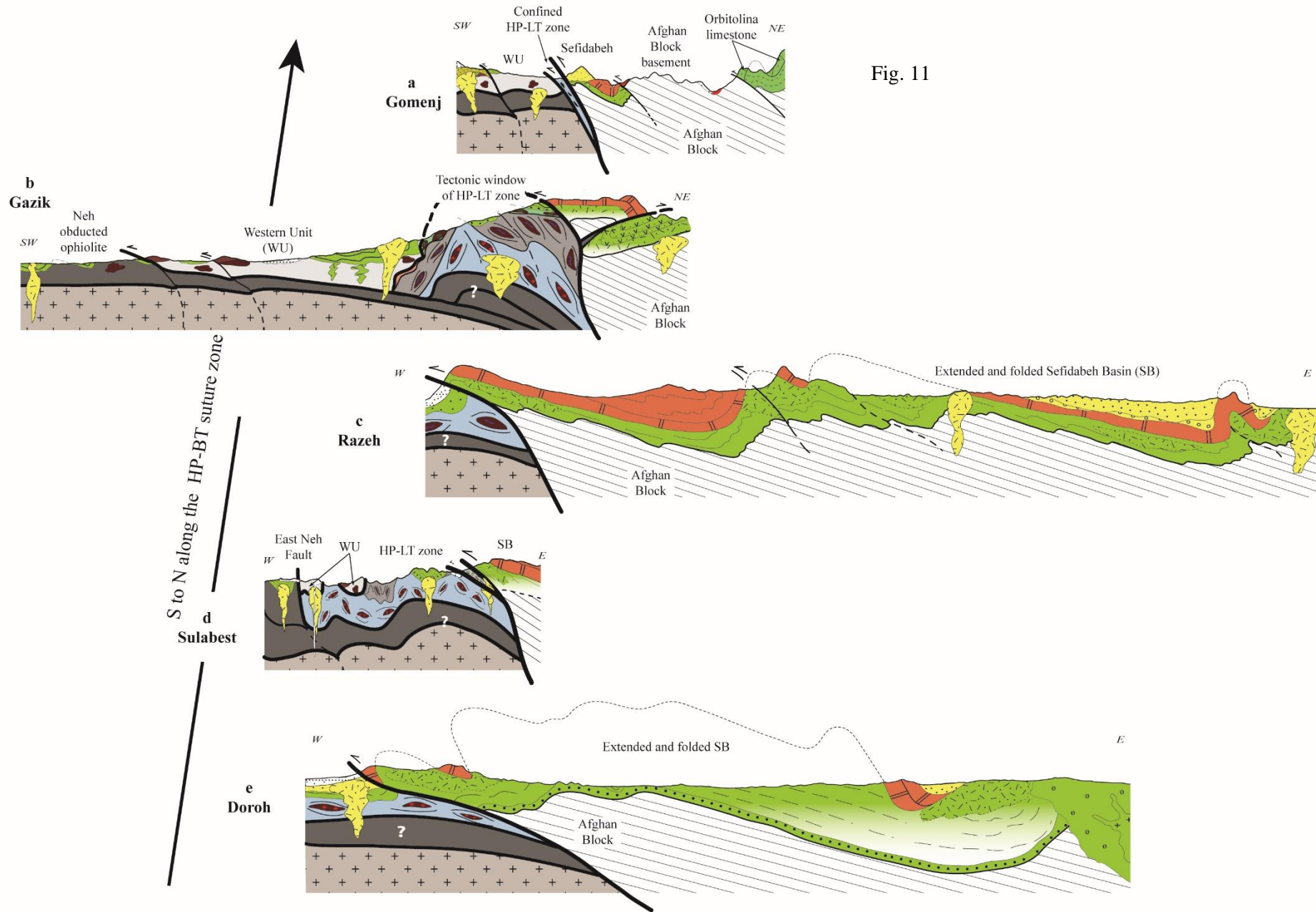


Fig. 11

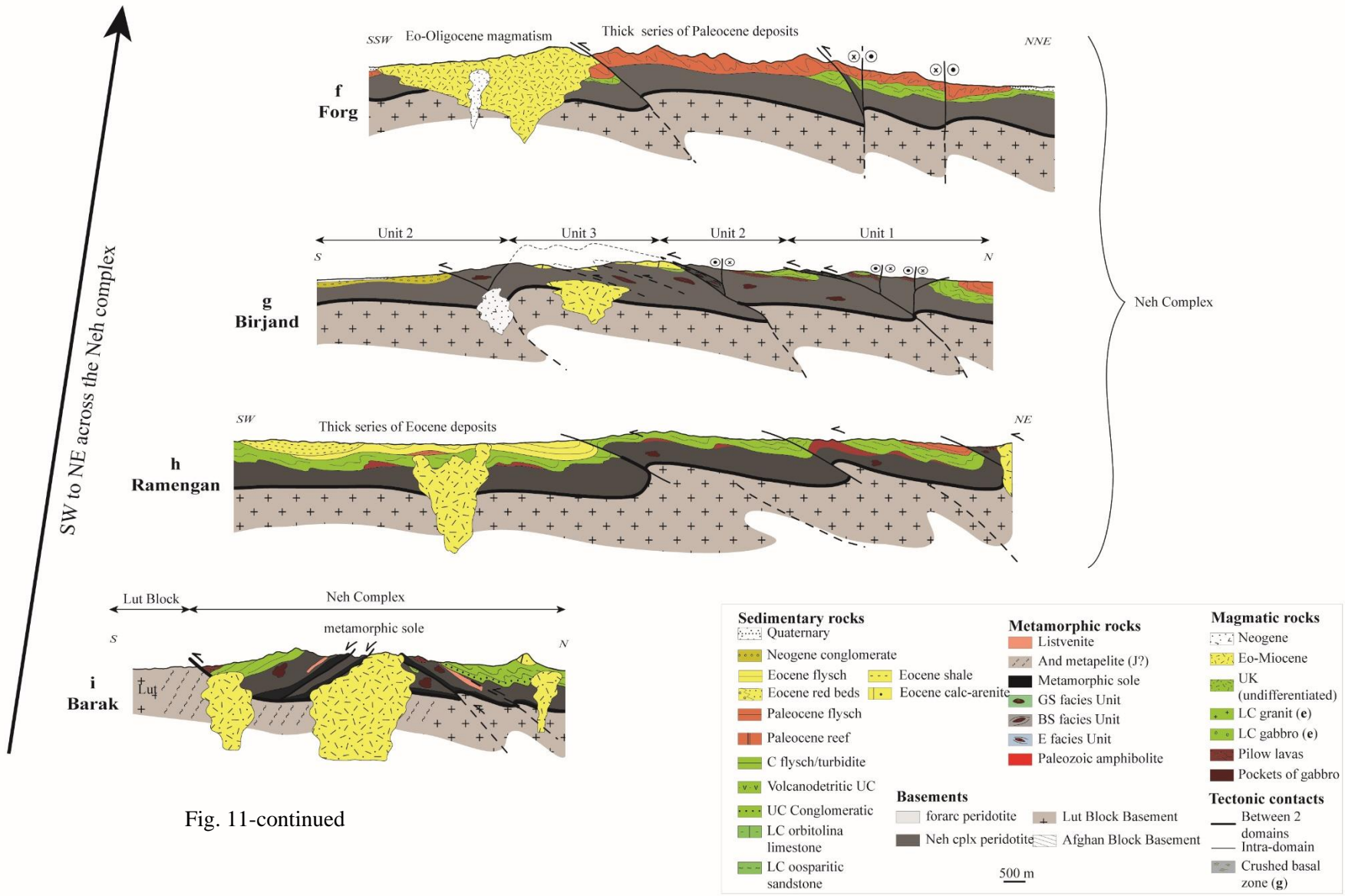
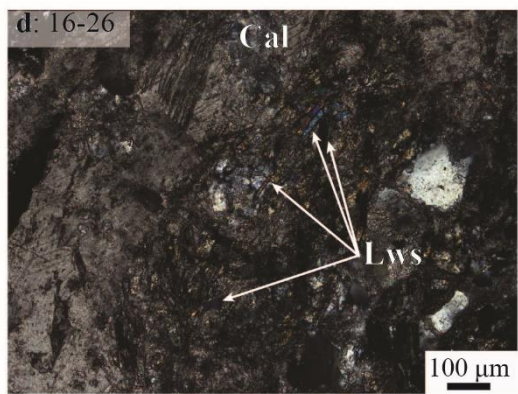
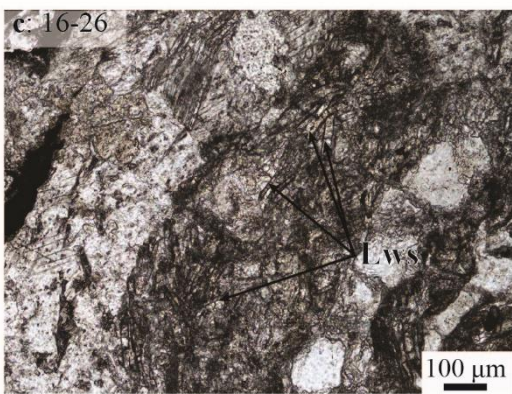
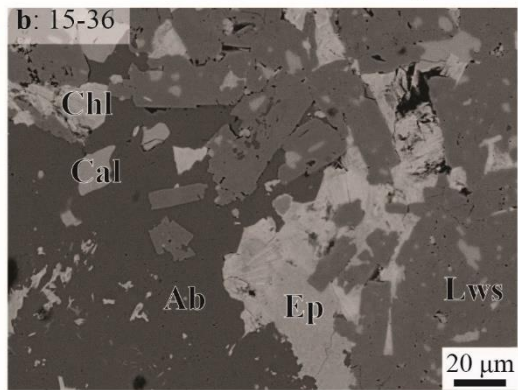
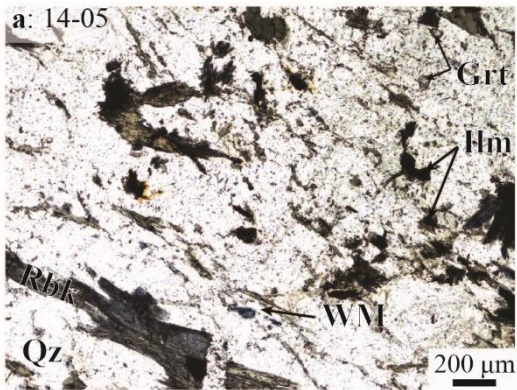


Fig. 11-continued

Fig 12

Birjand metasediments



Amphibolitic sole

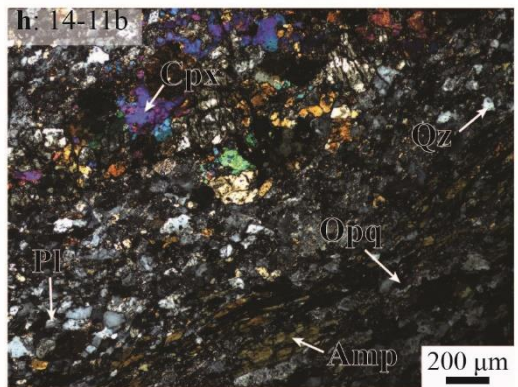
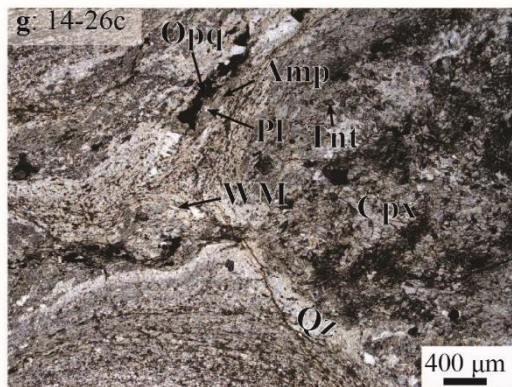
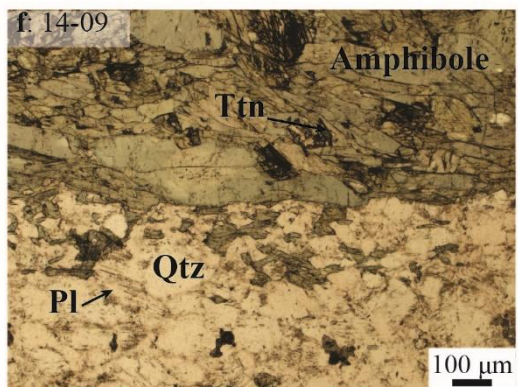
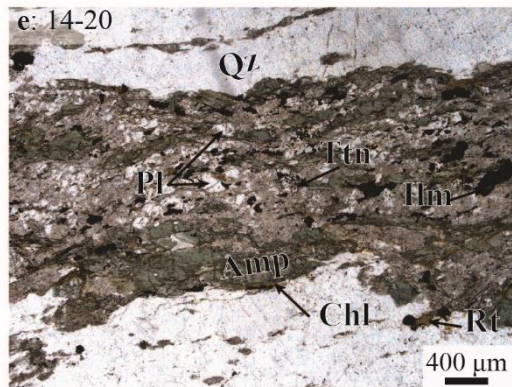


Fig 12-continued

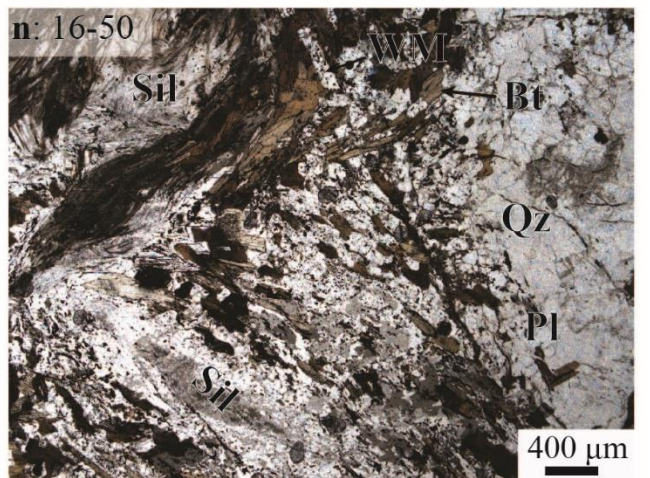
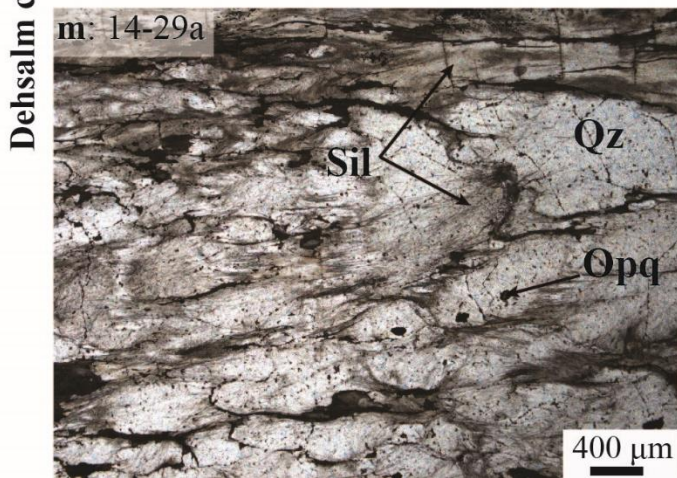
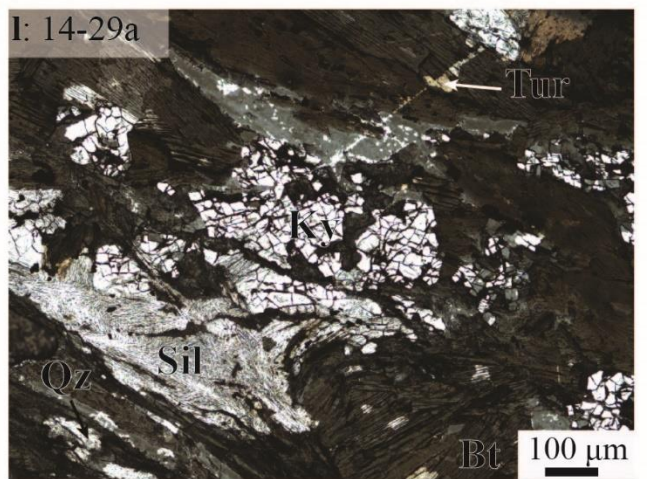
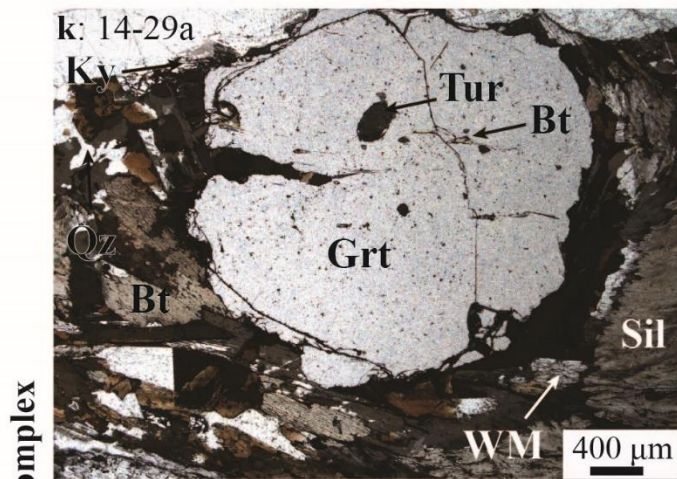
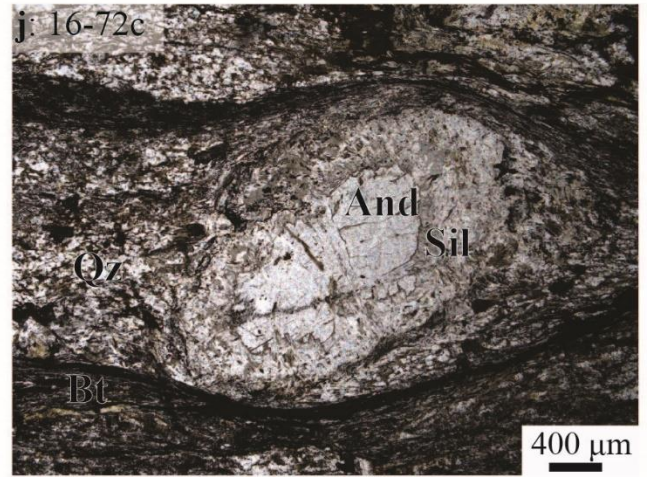
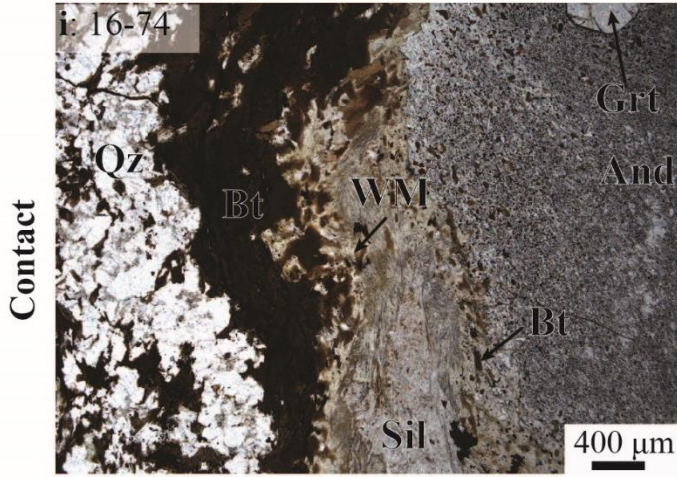
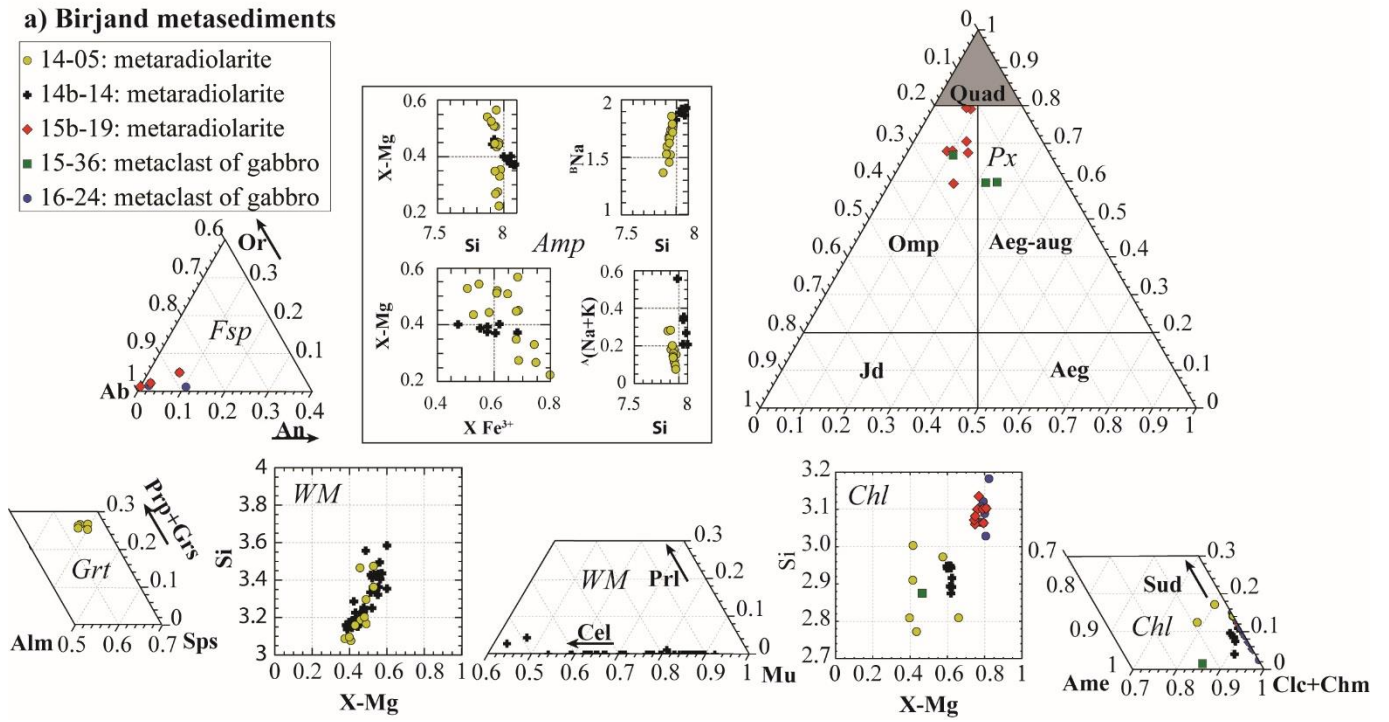


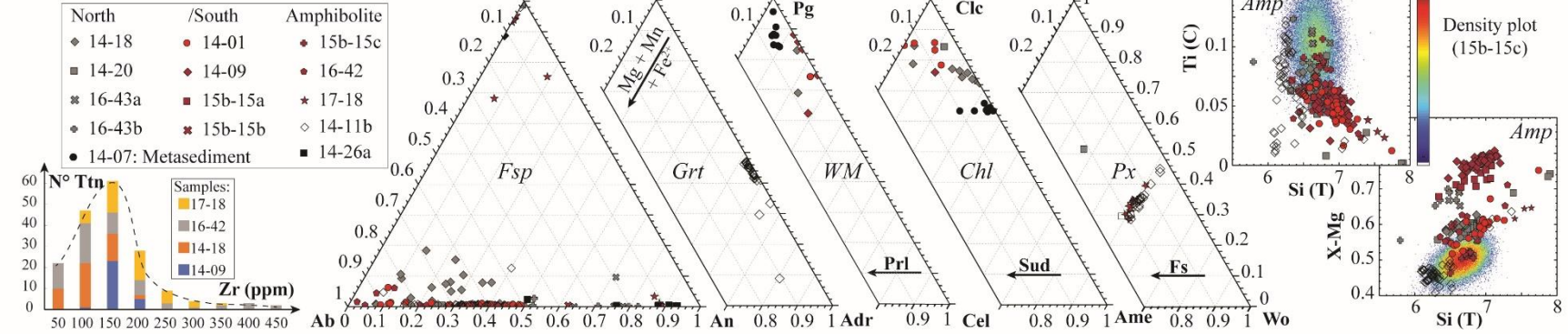
Fig 13

a) Birjand metasediments

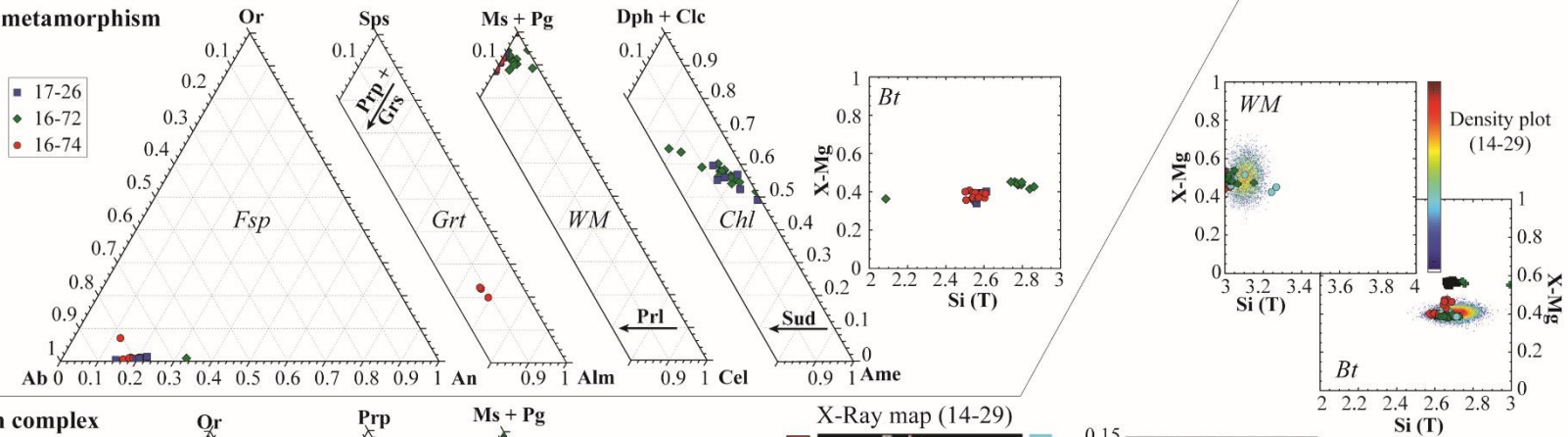
- 14-05: metaradiolarite
- ◆ 14b-14: metaradiolarite
- ◆ 15b-19: metaradiolarite
- 15-36: metaclast of gabbro
- 16-24: metaclast of gabbro



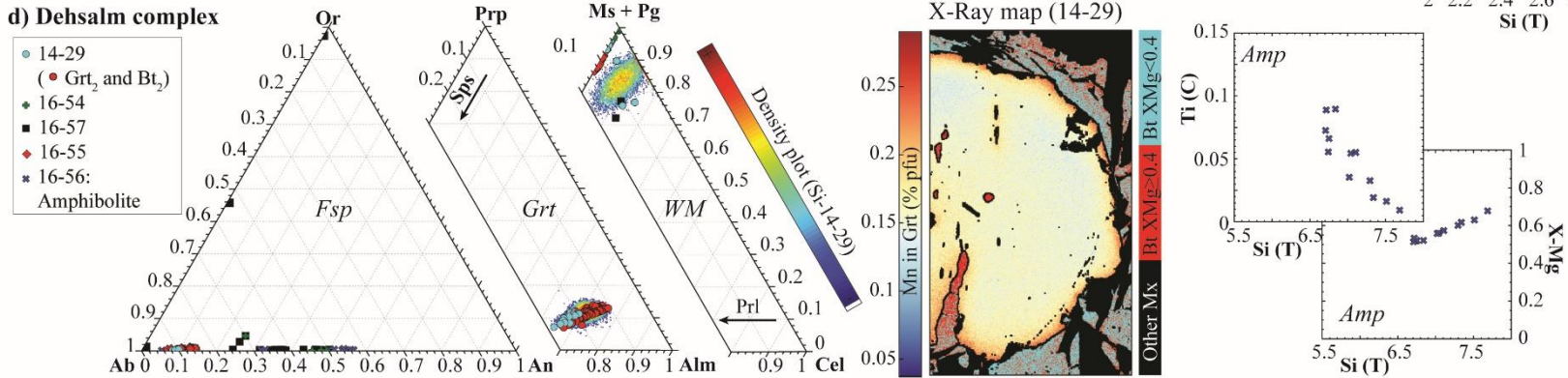
b) Amphibolitic sole



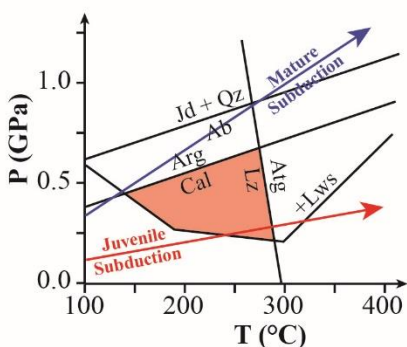
c) Contact metamorphism



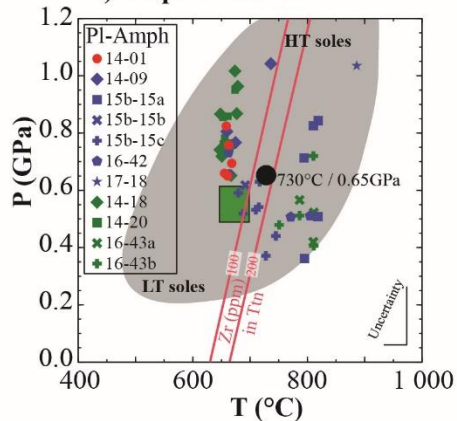
d) Dehsalm complex



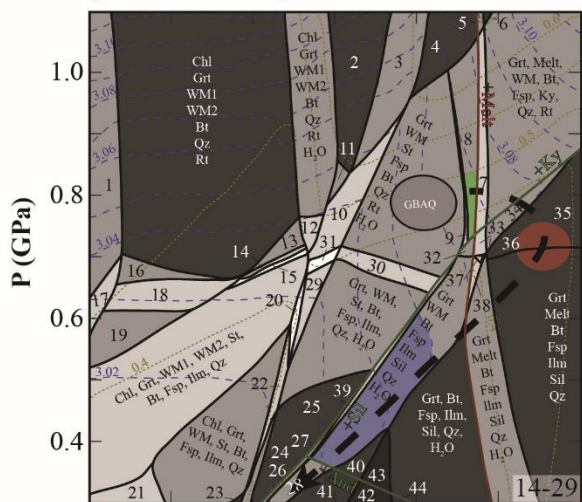
a) Birjand metasediments



b) Amphibolitic sole



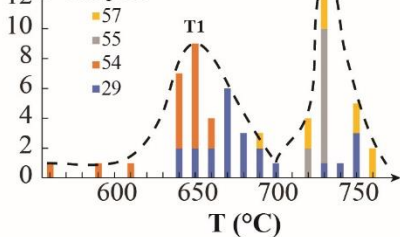
d) Deh-Salm complex



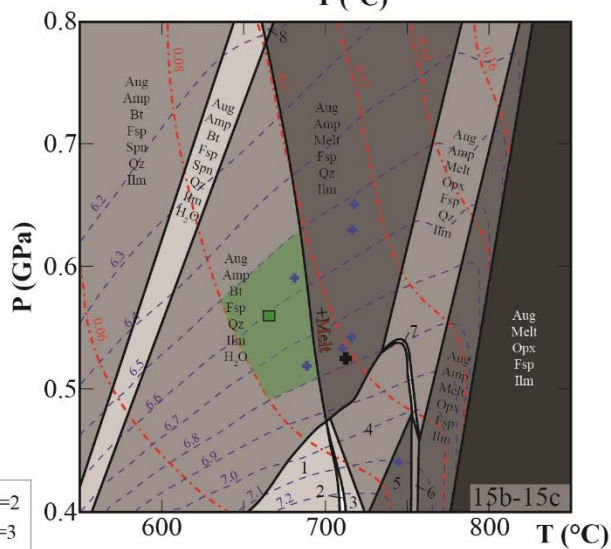
--- XMg Bt
 --- Si in Ph

N° Bt

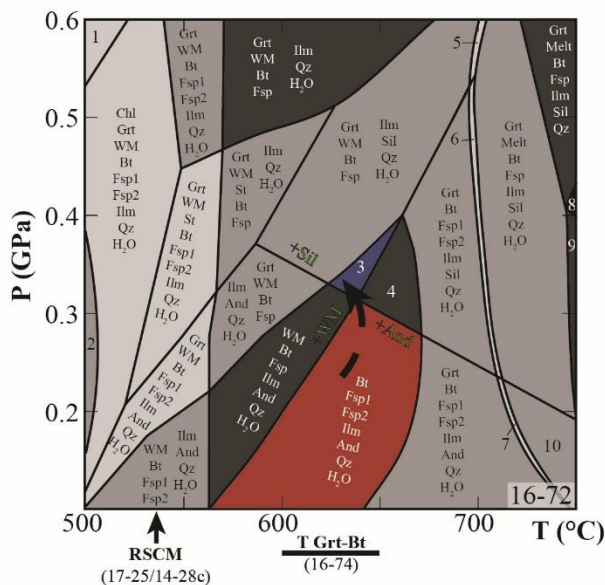
Samples:



V=2
 V=3
 V=4
 V=5
 V=6



c) Contact metamorphism



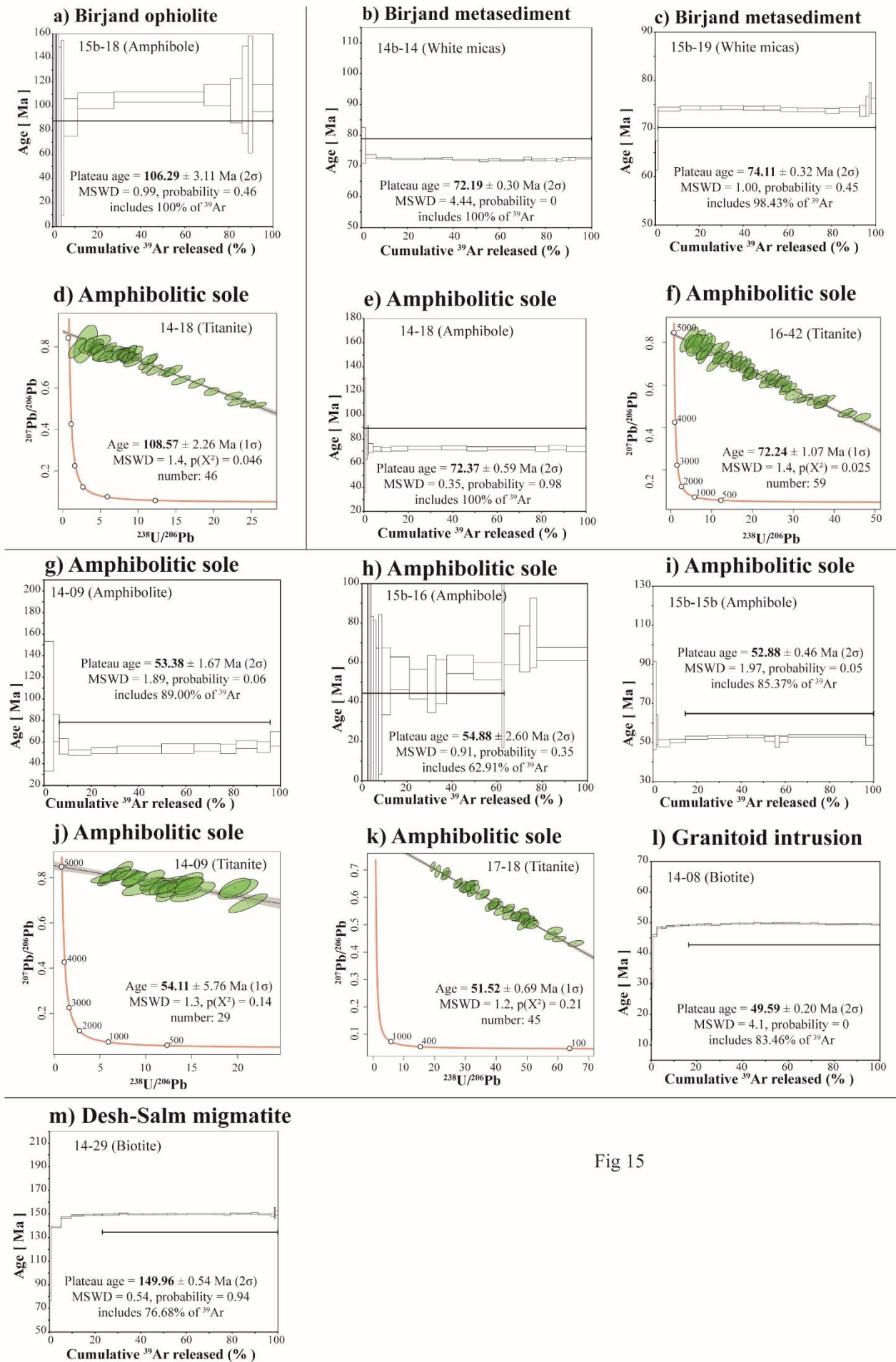


Fig 15

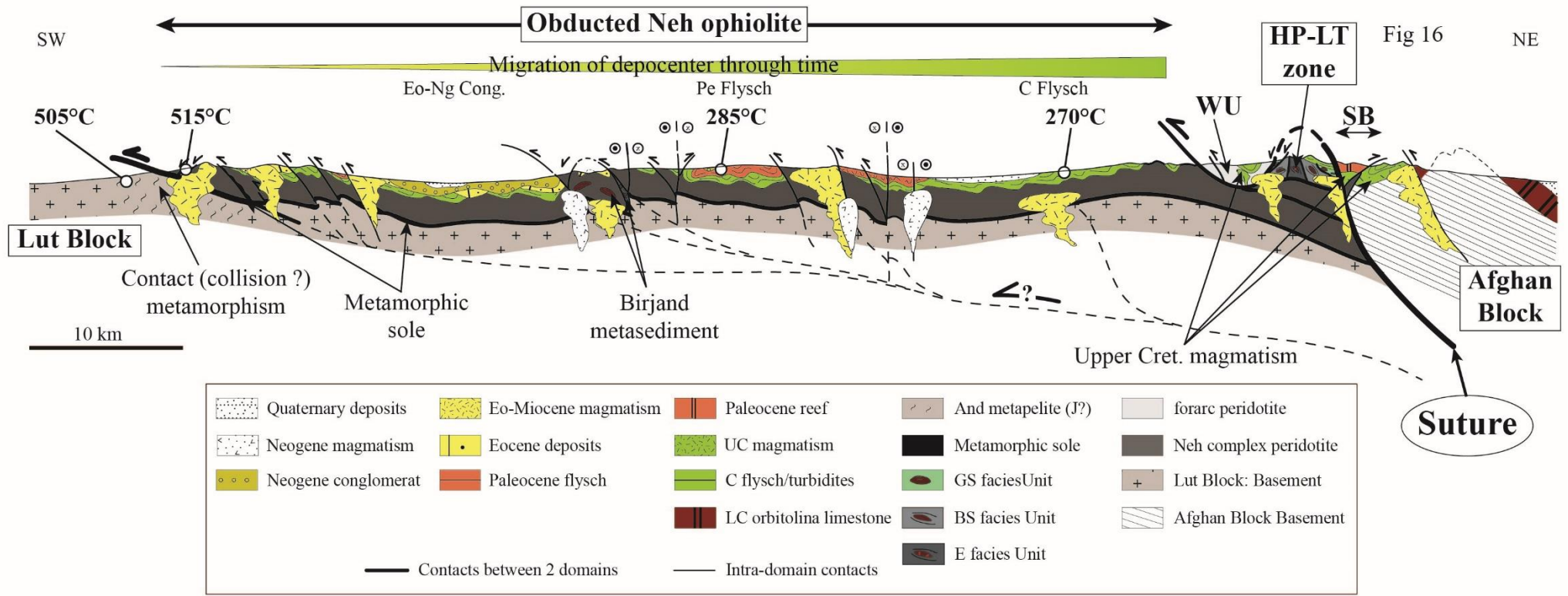


Fig 16

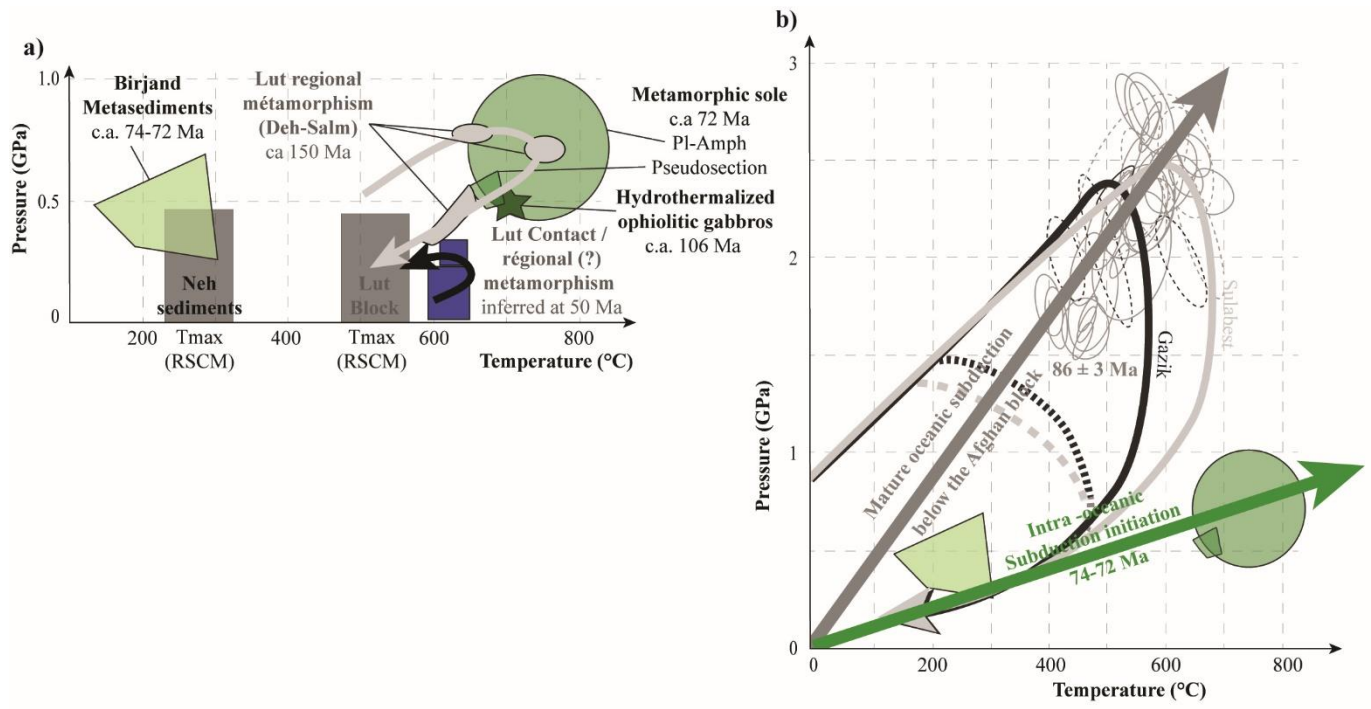
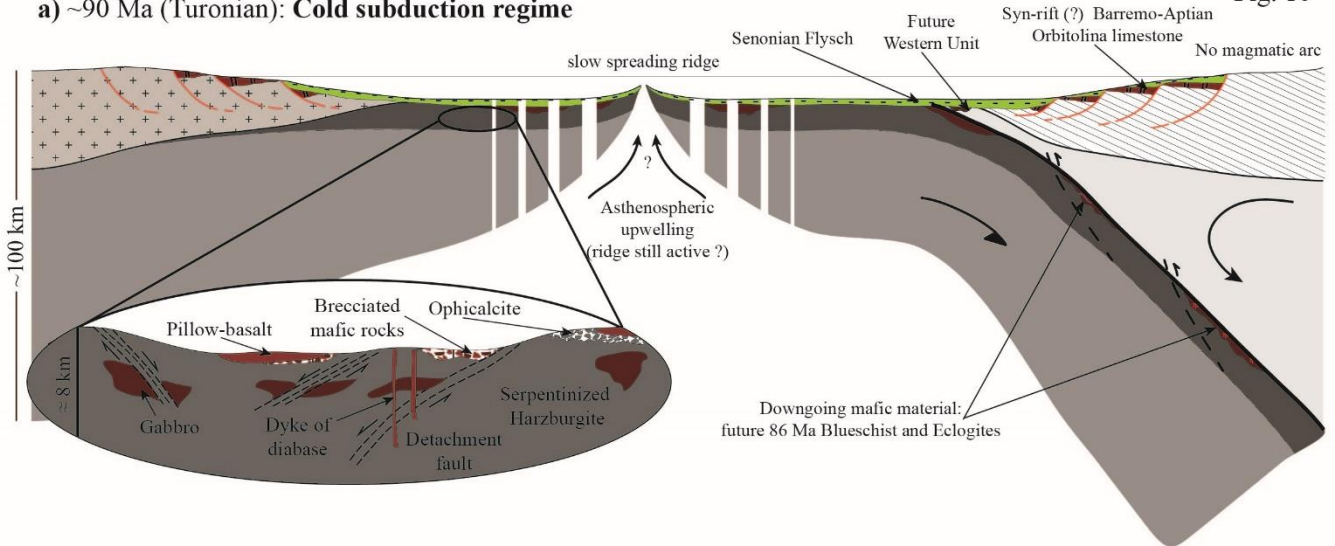


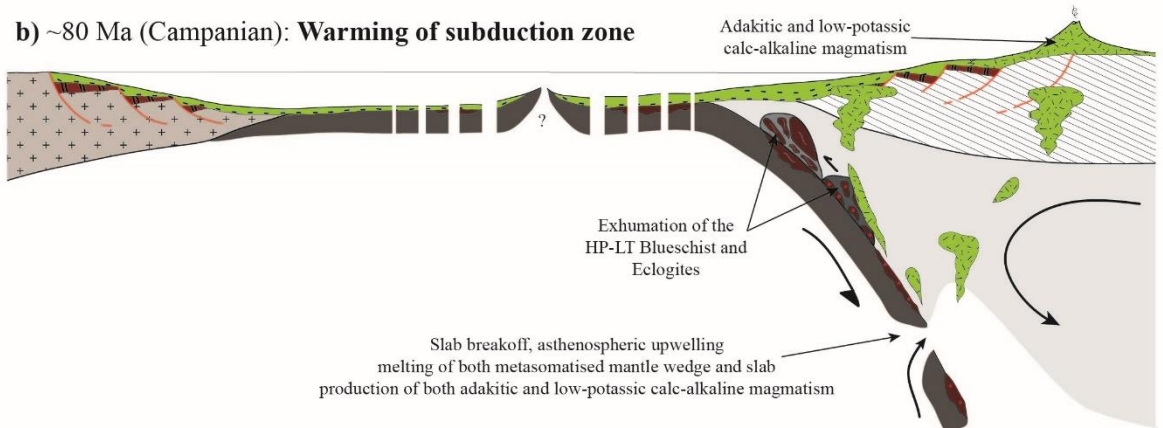
Fig. 17

Fig. 18

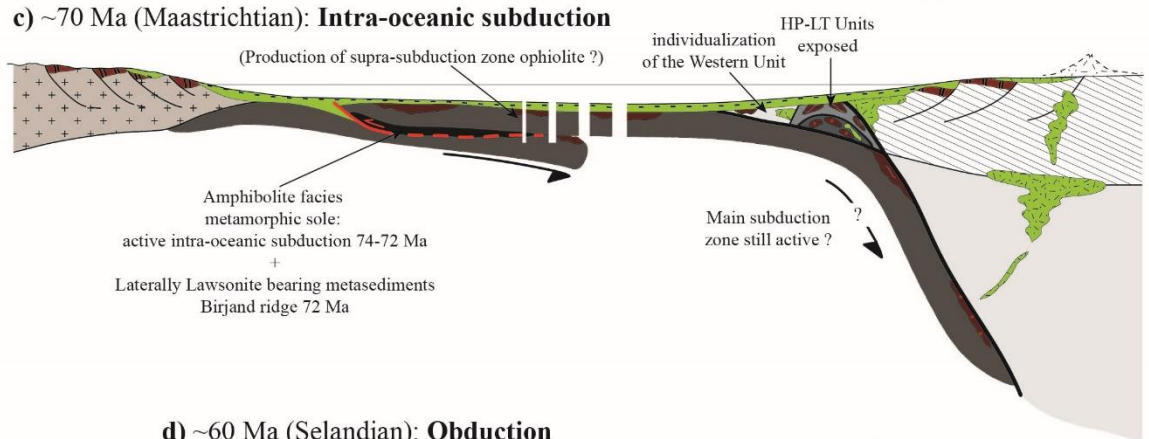
a) ~90 Ma (Turonian): Cold subduction regime



b) ~80 Ma (Campanian): Warming of subduction zone



c) ~70 Ma (Maastrichtian): Intra-oceanic subduction



d) ~60 Ma (Selandian): Obduction

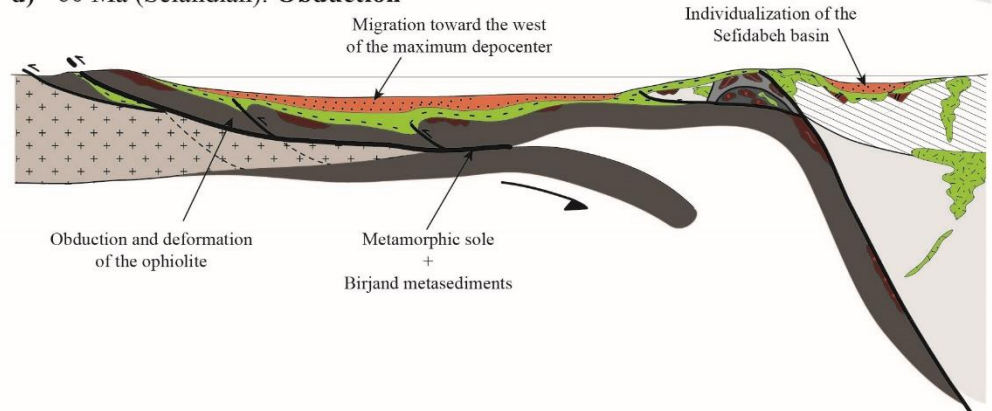
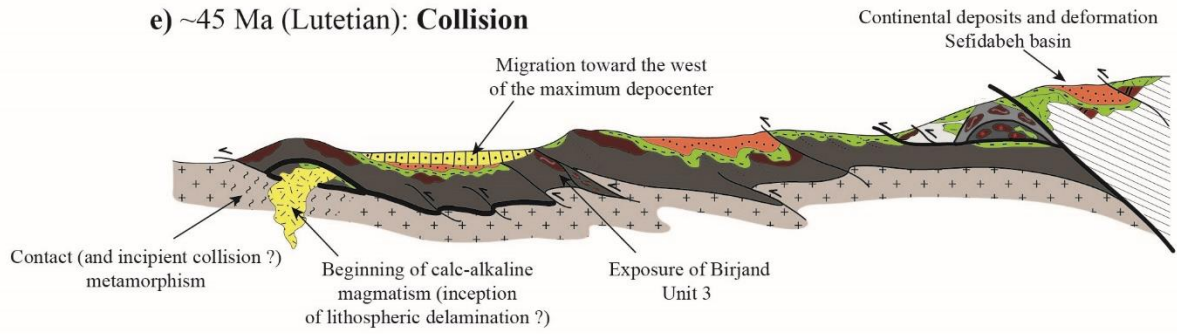
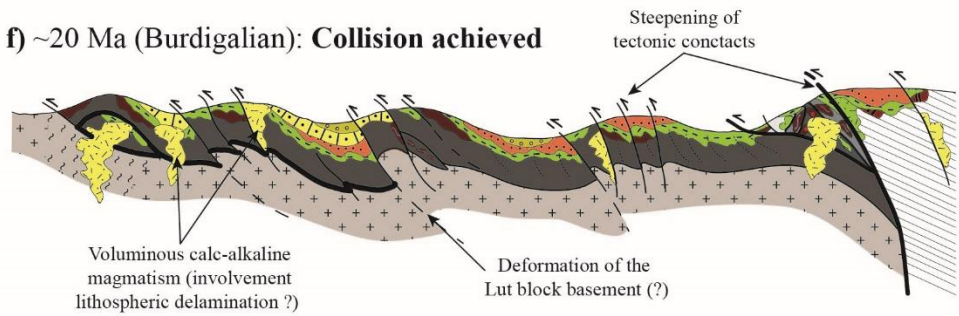


Fig. 18-continued

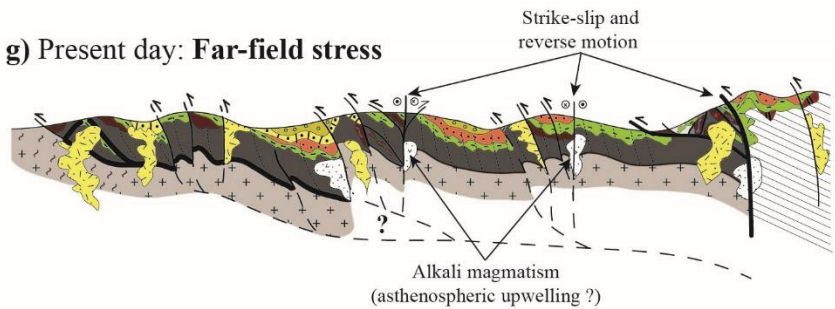
e) ~45 Ma (Lutetian): Collision



f) ~20 Ma (Burdigalian): Collision achieved



g) Present day: Far-field stress



	Neogene magmatism		Paleocene depositis		And metapelite (J?)		forarc peridotite
	Neogene conglomerat		UC magmatism		Metamorphic sole		Neh complex peridotite
	Eo-Miocene magmatism		C flysch/turbidites		BS facies Unit		Lut Block Basement
	Eocene depositis		LC orbitolina limestone		E facies Unit		Afghan Block Basement
— Contacts between 2 domains		— Intra-domain contacts					

74-72 Ma
(Campanian)

Fig. 19

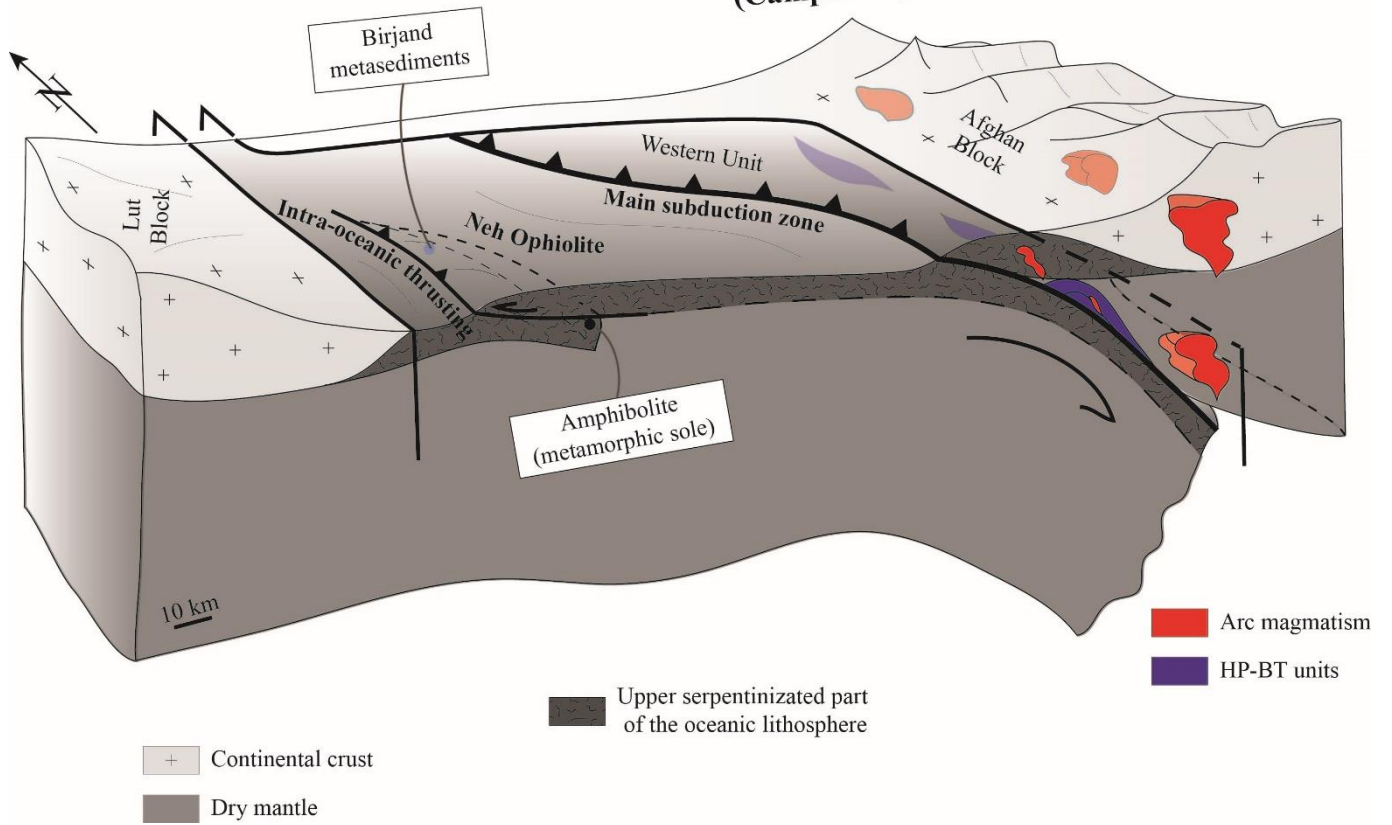


Fig. 20

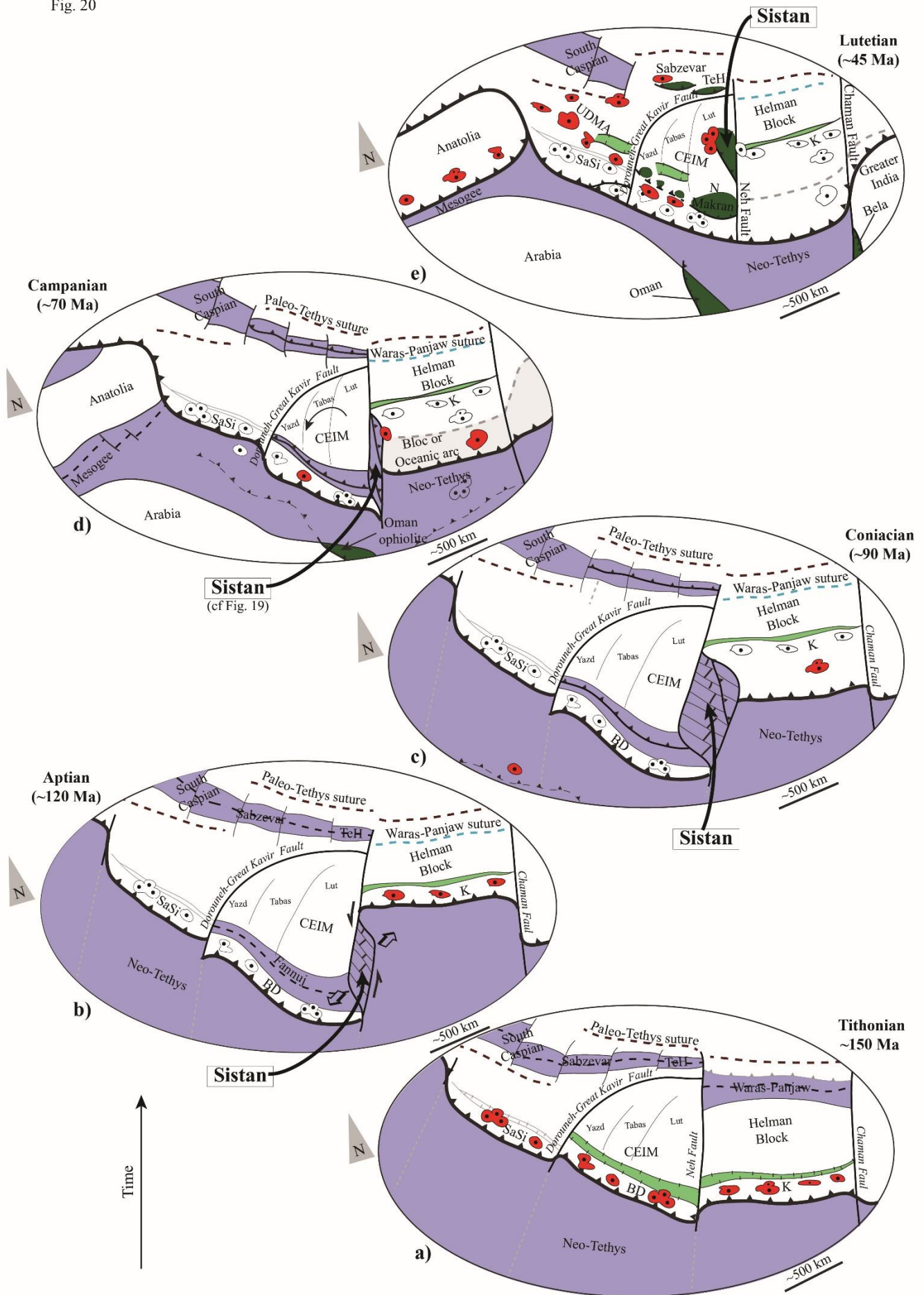


Table 1

N°	Name	Latitude	Longitude	Mineralogy													
				OI	Srp	Cpx	Opx	Pl	Amp	Ep	Ttn	Prh	Opq	Pmp	Cal		
Ophiolite																	
14-24	Serpentinite	32°03'13.6"	59°24'42.6"	+++	+	+	++		++++		+		+				
14-21	Serpentinite	32°17'31.4"	59°51'46.3"		++++								+				
15b-18	Gabbro Amph	32°40'43.7"	59°30'09.0"			++		(+)	++++				++		+		
16-01b	Gabbro Amph	32°40'43.7"	59°30'09.0"					+++	+++								
16-01c	Gabbro Amph	32°40'43.7"	59°30'09.0"			+		++	+++	+	+						
17-01	Gabbro Amph	32°30'4.8"	60°21'4.3"			++		+	+++	+		+					
14b-3	Basalt	32°47'27.0"	59°07'18.8"					++					+	+	+		
14b-4	Basalt	32°47'24.5"	59°07'43.4"					++		+			+	+	+		
15-39	Basalt	32°49'38.4"	59°08'8.5"			+++		+		+			+				

N°	Name	Latitude	Longitude	Mineralogy															
				Qz	Pl	Amp	Grt	Ph	Chl	Ep	Opq	Cal	Lws	Cpx	Ap	Srp	Ttn	Pmp	
Birjand metasediment																			
14-04a	Chert	32°43'42"	59°19'03.6"	++++	+++	Rbk ++			+	+	ilm +								
14-04b	Chert	32°43'42"	59°19'03.6"	++++	+++	Rbk ++		+	+	+	+								
14-05	Chert	32°43'07.8"	59°19'42.4"	++++	+++	Rbk ++	+	+	+	+	ilm +								
14b-14	Chert	32°43'08.2"	59°19'42.2"	++++	+++	Rbk ++	+	+	+		ilm +								
15b-19	Chert	32° 0'15.50"	59°34'41.40"	++++	+++	Rbk ++		+	++		ilm +			Omp ++					
15-36	Brecciated gabbro	32°41'39.8"	59°21'11.9"		+++	+++			+	+	+		++	Aeg ++	(+)		+	+	
16-24	Brecciated gabbro	32°41'08.5"	59°21'26.8"		+++								++	+++					
16-26	Spilitic-breccia	32°41'08.5"	59°21'26.8"			+						+++	++				+	+	
16-21b	Ophicalcite	32°41'08.3"	59°21'24.3"				+				Mag +	++	+			Liz ++			

N°	Name	Latitude	Longitude	Mineralogy																				
				Qz	Bt	Sil	Ky	Grt	Opq	Tur	Kln	Cal	Rt	Mnz	Pl	Chl	Amp	Ep	Ttn	Cpx	Or	Ph	OM	
Deshalm metamorphic complex																								
16-57	Micaschist	31°22'16.9"	59°32'18.9"	+++	+++	+++		+	+	+			+	+	+	+							+	
16-54	Micaschist	31°21'48.0"	59°32'06.5"	+++	+++	++			+	+	+				+								+	
16-55	Micaschist	31°21'48.0"	59°32'06.5"	+++	+++	++	(+)		+						+	+						+	+	
14-29a	Migmatite	31°21'13.1"	59°31'53.4"	+++	+++	++	+	+	+	+	(+)	(+)		(+)	+								+	
14-29b	Migmatite	31°21'13.1"	59°31'53.4"	+++	+++	++	+	+	+	+		(+)		+										
14-29c	Migmatite	31°21'13.1"	59°31'53.4"	+++	+++	++	+	+	+	+					+		+							
16-50	Migmatite	31°22'40.6"	59°32'37.3"	+++	+++	++		+	+						++								+	
16-56	Amphibolite	31°22'16.9"	59°32'18.9"										+		+++		+++	+	+	++				

N°	Name	Latitude	Longitude	Mineralogy																			
				Qz	Bt	And	Sil	Ph	Pl	Grt	Opq	Tur	Ap	Cal	Prh	Chl	Ttn	OM	Zrn				
Contact metamorphism																							
17-26	Micaschist	31°57'51.4"	59°30'42.1"	+++	+++	++	(+)	+	+			+			+								
16-72c	Micaschist	31°58'13.6"	59°29'08.0"	+++	+++	++	+	++	+		(+)		(+)	+		(+)		+++	+				
16-74	Micaschist	31°58'29.1"	59°29'06.0"	+++	+++	+	++	+	++	(+)					+	+							

Table 1-continued

N°	Name	Latitude	Longitude	Mineralogy																				
				Amp	Pl	Cpx	Ttn	Qz	Ep	Grt	Ph	Opq	Rt	Mag	Bt	Or	Chl	Cal	Pmp	Prh	Ap	Aln	Zrn	OM
Amphibolitic sole																								
14-01	Amphibolite	32°43'33.9"	59°01'59.8"	++++	+++		+	++	+		+	Ilm +					+				(+)	(+)		
14-09	Amphibolite	32°00'04.7"	59°31'01.8"	++++	+++		++	++	+		+	Ilm +	+					+						
14-18	Amphibolite	32°17'30.9"	59°51'44.2"	++++	++++		++	(+)	+			+					(+)							
15b-15a	Amphibolite	31°59'58.7"	59°30'59.7"	++++	++++																			
15b-15b	Amphibolite	31°59'58.7"	59°30'59.7"	++++	++++																			
15b-15c	Amphibolite	31°59'58.7"	59°30'59.7"	++++	++++		+	++				Ilm +		+				+		+	+	+		
16-42	Amphibolite	32°17'40.4"	59°51'16.4"	++++	+++		++	++				+								+				
16-43b	Amphibolite	32°17'33.0"	59°51'04.2"	++++	++++			++																
16-45a	Amphibolite	32°17'32.7"	59°51'03.4"	++++	+			++																
16-45b	Amphibolite	32°17'32.7"	59°51'03.4"	++++			+++																	
14-11b2	Amphibolite	32°00'04.7"	59°31'01.8"	+++	++	(+)		+			+	+												
14-20	Amphibolite	32°17'31.4"	59°51'46.3"	++++	+++	(+)		+++++				Ilm +	+			+	+	+				+	+	
16-43a	Amphibolite	32°17'33.0"	59°51'04.2"	++++	++	(+)	+	++	++													+		
16-86	Amphibolite	31°59'56.3"	59°22'34.7"	++++	+++	(+)	+		+									+	+			(+)		
14-11b	Amphibolite	32°00'04.7"	59°31'01.8"	++++	+++	++	++	+	++	+		+						+	+					
14-26a	Amphibolite	32°02'09.9"	59°24'00.1"	+++	++	++	+	++			+					+	+							
14-26c	Amphibolite	32°02'09.9"	59°24'00.1"	+++	+	++	+	++	+	+	+	+						+						
17-18	Amphibolite	32° 2'13.08"N	59°24'1.02"E	++++	+++	++																		
14-07	Sediment	32°00'56.2"	59°33'19.0"					++++			+++	+						+						
14-23a	Sediment	32°01'08.9"	59°26'12.1"					+++				+			+++		+	+						++
16-80	Sediment	31°59'24.9"	59°29' 58.4"		(+)			+++							++		+	+++						++

Table 2

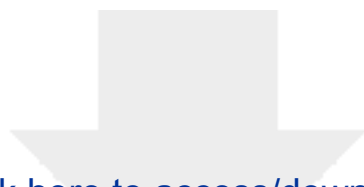
Location	Name	Size (km ²)	Protolith ages (biostrat./radiometric)	Structural organization	Mantle lithology	Crustal Lithology	Chemistry	Interpretation	Metamorphism	Interpretation	Post-ophiolite magmatism	Oldest unconformable sediments	References
E CEIM	Sistan	20 000	124-106 Ma	Kilometer scale slices	Harzburgite	Gabbroic intrusion Pillowed or massive basalt	N-MORB E-MORB OIB CA	Mid oceanic ridge activity Enriched mantle SSZ	1) Amphibolite: 700°C-0.65GPa 74-72 Ma; Lws bearing metasediments: 250°C-0.4GPa 72 Ma 2) HP-LT rocks at 86 Ma	1) Metamorphic sole or lateral equivalent 2) Subduction	1) CA and adakite Upper Cretaceous 2) CA Eo-Oligocene 3) Alkaline Miocene	Eocene conglomerate or sandy-limestone	Delaloye et Desmons, 1980 Saccani et al., 2010 Zarrinkoub et al., 2012a Pang et al., 2012 Pang et al., 2013 This study
NW CEIM	Sabzevar Torbat-e-Heydarieh	7 000	Upper Jurassic; 101-75 up to 52.4 (?) Ma	kilometer scale slices and colored mélange	Harzburgite Wherlrite	Gabbro Dikes of diabase Basaltic lavas	N-MORB E-MORB OIB IAT CA	SSZ	1) Blueschist: 420-500°C 1.3-1.55 GPa 54-51 Ma; 2) Granulite: 780°C-1.1-1.2 GPa 105 Ma	1) Blueschist subduction related (age?) 2) Granulite: metamorphic sole	CA and adakite at 45 Ma (flare up?) High Silica Adakite at 58 Ma (partial melting of slab, age?)	Eocene Nummulitic limestone	Lindenberg et Groler, 1984 Ghazi et al., 2004 Nasrabad et al., 2011 Khalatbari Jafari et al., 2013 Moghadam et al., 2014 Rossetti et al., 2014 Moghadam et Stern, 2015 Omrani, 2017 Kazemi et al 2019 Mazhari et al., 2019
SW CEIM	Nain Ashin	600	145-67 Ma or older up to 188 Ma (?)	Small tectonic slices and colored mélange	Harzburgite Lherzolite Dunite	Gabbro Dikes of diabase Massive and pillowed basalt	N-MORB IAT CA	SSZ	Amphibolite 113 Ma	Metamorphic sole	CA Cenozoic	Paleocene limestone	Sharkovski et al., 1984 Ghazi et al., 2004 Moghadam et al., 2009 Shirdashtzadeh et al., 2010, 2015, 2020 Moghadam and Stern, 2015 Pirnia et al., 2020
SW CEIM	Deshir Shahr-e-Babak	150	101-67	Small tectonic slices and colored mélange	Harzburgite Lherzolite Pyroxenite	Gabbro Dikes of diabase Massive and pillowed basalt	N-MORB IAT CA	SSZ			CA Cenozoic	Maastrichtian limestone	Ghazi et al., 2004 Moghadam et al., 2009, 2010 Moghadam et Stern, 2015
SW CEIM	Balvard Baft Esfandagheh	3 000	103-72	Small tectonic slices and colored mélange	Harzburgite	Gabbro Dikes of diabase Basaltic lavas	E-MORB CA IAT	SSZ			CA Cenozoic	Maastrichtian limestone	Moghadam et al., 2009, 2011, 2013 Moghadam et Stern, 2015
N Makran	Bad e Zeyarat Dar Anar	20 000	145-111	Kilometer scale slices	Harzburgite	Gabbro Dikes of diabase Pillowed basalt	N-MORB E-MORB	SSZ	Blueschist: 300-380°C 0.9-1.4 Gpa 100-95 Ma CCW PT path	Blueschist: cold subduction related regime after amphibolitic metamorphism		Maastrichtian limestone	Ghazi et al., 2004 McCall, 1997, 2002 Hunziker et al., 2015, 2017 Omrani et al., 2017 Burg, 2018 Sepidbar et al., 2020
N Makran	Fannuj Maskutan	2 800	<140	Kilometer scale slices	Lherzolite Harzburgite	Gabbro Dikes of diabase Basaltic lavas	IAT (S) E-MORB (N)	SSZ				Maastrichtian limestone	McCall, 1997, 2002 Hunziker et al., 2015 Burg, 2018 Sepidbar et al., 2020



[Click here to access/download](#)

Supplementary Interactive Plot Data (CSV)
SM1-GPS coordinates.xlsx





[Click here to access/download](#)

Supplementary Interactive Plot Data (CSV)
SM2-chemistry.xlsx





[Click here to access/download](#)

Supplementary Interactive Plot Data (CSV)
SM3-pseudosections.xlsx



Declaration of interests

The authors declare that they have no known competing financial interests or personal relationships that could have appeared to influence the work reported in this paper.

The authors declare the following financial interests/personal relationships which may be considered as potential competing interests:

This piece of the submission is being sent via mail.